POLITECNICO
MILANO 1863

Light-Driven Energy Conversion Processes in Natural and Bio-inspired Light Harvesting Systems probed by Two-Dimensional Electronic Spectroscopy

Doctoral Programme in Physics

Doctoral Dissertation of: **Mattia Russo**

Student ID: 913191

Supervisor: Prof. Giulio Cerullo

Tutor: Prof. Sandro de Silvestri

Year: 2022 Cycle 34

Contents

List of Figures

Abstract

In recent years the generation of renewable energy from bio-inspired systems came into the spotlight, with the goal to mimic the efficient energy conversion mechanism performed by natural organisms as higher plants, cyanobacteria and algae. Such systems exploit chromophores as chlorophylls (Chls) and carotenoids located in peripheral antenna complexes to capture the solar energy and transfer it to a pigment-protein complex, called reaction center (RC), in which charge separation and the subsequent photosynthesis chemical reaction take place. All these excitation energy transfer (EET) processes occur on an ultrafast timescale and their study is of crucial importance in order to, on the one hand, to understand natural photosynthesis and on the other hand derive design rules for artificial light-harvesting complexes. In order to temporally and spectrally characterize the EET processes, a combination of high temporal and spectral resolution is required. The two-dimensional electronic spectroscopy (2DES) technique is well suited for this aim since it generates time-resolved 2D correlation excitation/detection frequency maps typically with sub20-fs time resolution. In the first part of this work, we adopted 2DES to characterize the EET mechanism in natural photosystems in which Chls red forms (RF), absorbing at lower energy with respect the RC, are involved; specifically, we study photosystem I (PSI) in cyanobacteria and higher plants. In both systems, our results put in evidence an ultrafast energy equilibration between Chls bulk and red forms charcterized by two time constants; the first one $<$5ps describe EET from the bulk to Chls RF, typically refereed as downhill EET. The second one $<$1ps represents back transfer from the Chls RF to Chls bulk, typically defined as uphill EET. These results show the efficiency of the EET processes among Chls and demonstrate that Chls RF participate to the photosynthesis chemical reaction. In natural systems, there are some aspects as fast charge recombination and spatially limited EET that make the system unoptimized. The first aspect drastically reduces the effective fuel yield obtained from the photosynthesis chemical reaction. In this view, bio-inspired photosystems that mimic the structure of the natural one, are synthesized to increase the recombination time from hundred ps to the ns time scale. Here we report an ultrafast spectroscopy study of the so-called quantasome system, that uses Perylene Bisimide (PBI) as light harvesting antenna and a Ruthenium

Polyoxometalate (Ru_4POM) as a catalytic cofactor. Following photoexcitation of PBI, ultrafast charge separation leads to the generation of charges in the antenna (PBI^+ and PBI^-). The time-evolution of both species show a common dynamic till 800fs, in which the formation and consequent localization of the charges take place. Then, in 8ps, we observe an hole transfer from PBI^+ to Ru_4POM^+. The recombination time is estimated longer than 1.5ns that demonstrates a long-lived charge separation. The other aspect that can be improved for the production of innovative light harvesting devices is the distance at which EET between molecules can take place, beyond the typical limit set by the Förster radius (10nm). To this aim, we study possible EET between donor/acceptor molecules spatially separated by 2μm with spectrally separated excitonic states. This long range EET can be achieved when the two molecules are confined in an optical microcavity and both excitonic states are strongly coupled with the same cavity mode. This regime promotes the formation of three hybrid polaritons states, named upper polariton branch (UPB), middle polariton branch (MPB) and lower polariton branch (LPB). Following the excitation of the UPB state, 2DES enabled us to observe an ultrafast energy delocalization that promotes a direct connection between the molecules.

Introduction

0.1. From Natural to artificial light harvesting system

A light harvesting complex can be defined as any ensemble of molecules or materials that allows to capture and convert the light energy into another forms as chemical energy (photosynthesis in plants) and electrical energy (photovoltaic panels). This possibility opens up the investigation of different materials to yield renewable energy or optimize electrical processes. In this view, the high energy conversion efficiency performed by photosynthetic organisms providing a reference architecture for the design of specilized light harvesting systems[1, 2]. In particular, systems able to as higher plants, cyanobacteria and algae, are good examples of molecular absorb, drive and convert solar energy[3]. In general, they exploit a combination of two pigment-protein complexes called Photosystem II (PSII) and Photosystem I (PSI) in order to compute oxide-reduction chemical reaction of the water. Such systems are composed of two functional and structural moieties: an external part called light harvesting complex (LHC) antenna that surround the second part called Core where the Reaction Center (RC) is located. Such systems are harbored in the chloroplast membrane and the chromophores that mainly harvest the light are carotenoids and chlorophylls (Chls) [4]. Figure 1 shows a schematic representation of the PSII and the PSI complexes with a guideline of the photosynthesis process. Specifically, when the solar energy interacts with both systems, it is absorbed by the LHC antenna and transferred to the RC. Here, the primary chlorophylls of PSII and PSI called P680 and P700 respectively are excited by forming an electron-hole pair. The name of these molecules comes from to the optical wavelength at which they absorb; 680nm for P680 and 700nm for P700. The photogenerated electron in the P680 is then transferred to the PSI where it recombines with the hole of the P700 . In this way, the system creates a well separated hole-electron pair (hole in PSII and electron in PSI) that can induce chemical reactions[1]. In particular, the hole in the P680 works as a precursor for the water oxidation described by the chemical reaction: $2H_2O+4h^+ \rightarrow O_2+4H^+$. The hydrogen ions obtained from this mechanism are then reagents of the second chemical reactions with the photoesxited electrons

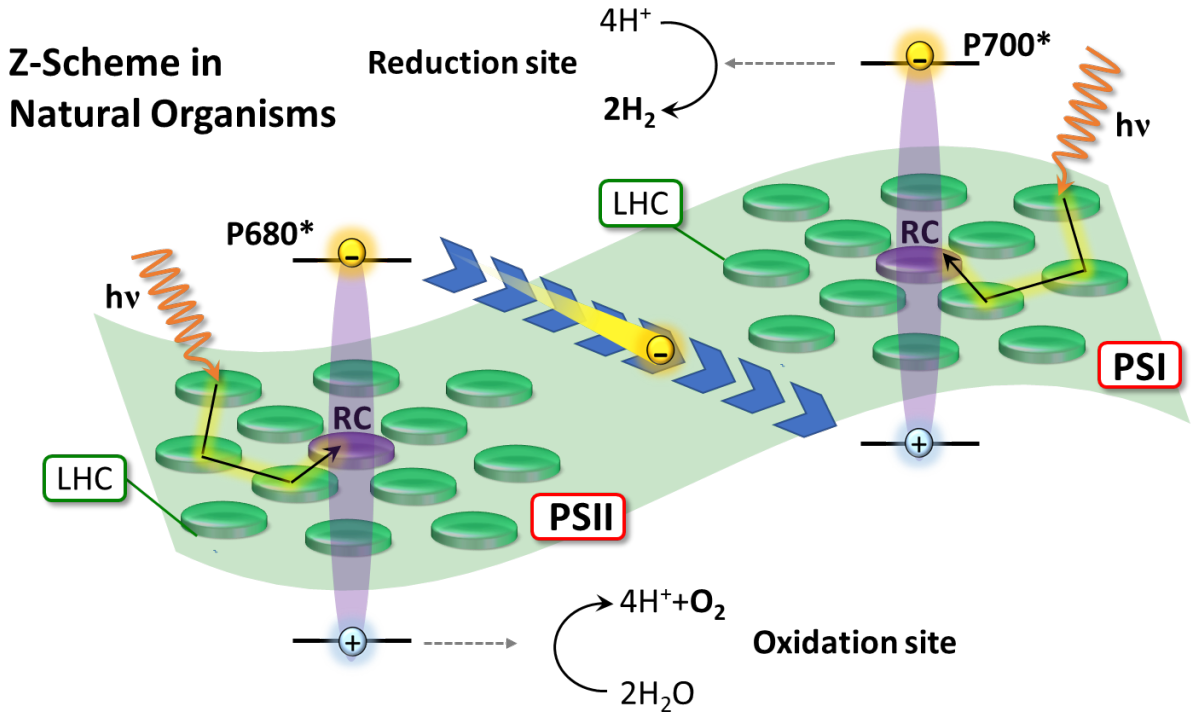

Figure 1: Z-Scheme in natural organisms with representation of the charge transport from PSII to PSI supercomplexes. When a photon is absorbed by the light harvesting complex (LHC) of both photosystems, it will be transferred through pigment-protein complexes (green buttons) through the reaction center by generating an electron/hole pair in the P680 (for PSII) and P700 (for PSI). The photexcited electron of the P680 travels trough the membrane in order to quenched the hole of the P700. The P680 remaining hole is used to performed water oxidation and the electron in the P700 is used for the reduction of the hydrogen

in the P700 by producing hydrogen: $2H^+ + 4e^- \rightarrow 2H_2$. Several studies are conducted on these light harvesting systems in order to spectrally and temporally characterize energy conversion processes and the role of each chromophore [5, 6]. Particular interest is dedicated to a group of low-energy Chls usually called red forms (RF) that absorb at lower energy with respect the RC [7]. Such Chls increase the light harvesting capacity of the system, but their role during the photosynthesis process still presents some uncertainty. In particular, their amount and location are different in various organisms and this aspect can impact the photosynthesis process [8]. It is already been observed that some aspects as fragility, favorable charge recombination and excessive intensity solar energy, negatively impact on the effective fuel obtained from the photosynthesis. For this reason, several studies are oriented to synthesize robust bio-inspired systems to mimic the energy conversion efficiency of the natural one and overcome the negative aspects. In this view, semiconductors materials represent the best choice to reproduce the PSI and PSII

photophysiscs[9]. In particular, the charge separation created in the P680 and P700 can be reproduced by irradiating a semiconductor where an electron/hole pair can be created in the lower energy state of the conduction band/higher energy state of the valance band respectively. At this point, the photoexcited charges can be transferred in order to perform oxidation and reduction chemical reactions. Such designed systems show a longer charge recombination time that consequently increase the effective fuel [10].
In this context, there are other characteristics that make the natural photosystems not optimized. One example is the excitation energy transfer (EET) process occurring within two chromophores. Specifically, the limitation of the EET distance between molecules set by Förster theory, shows that the distance between them can not be more then 10nm . Recent studies of donor/acceptor molecules confined in optical cavities, shows that long range EET processes is possible when both molecules are strongly coupled with the same cavity mode, by generating new hybrid states called polaritons [11]. Such new states can assist EET from the donor to the acceptor molecule. It is observed that this coupling take place also when the molecules are spatially separated by μm spacer by demonstrating the presence of a long range energy transfer[12].

0.2. Experimental Methods

In order to evaluate the energy conversion efficiency in different light harvesting systems (natural and artificial), it is necessary to have experimental methods that track their dynamical properties. In this field, time-resolved nonlinear spectroscopy techniques emerged as the powerful tool in order to reach this goal[13].High temporal resolution can be obtained by using broadband laser pulses that can be compressed up to $< 10fs$ (in the visible spectral range)[14]. Pump probe spectroscopy represents the more versatile technique adopted for catching dynamical properties in a generic system [15]. Specifically, in this method, the system interacts with two delayed laser pulses by providing an nonlinear emission from the sample. Figure 2a shows a simple scheme of the pulse sequence where the first pulse acts as a pump and it is delayed by τ with the respect the second one that acts as a probe. For a fixed delay between the pulses, the iterations provide an emitted signal $S(\tau, t)$ which is a function of a specific delay τ and the detection time t. Such a signal is then usually Fourier transformed with respect the variable t with a spectrometer by obtaining a so called Transient Absorption (TA) spectrum. Such spectra reproduce how the probe is absorbed from the sample when it is excited previously by the pump pulse. By scanning the delay τ we can measure a collection of TA spectra as a function of the delay between pump probe pulses, providing a temporal evolution of the system. An example of this dataset is reported in figure 2b where the entire collection of the spectra is

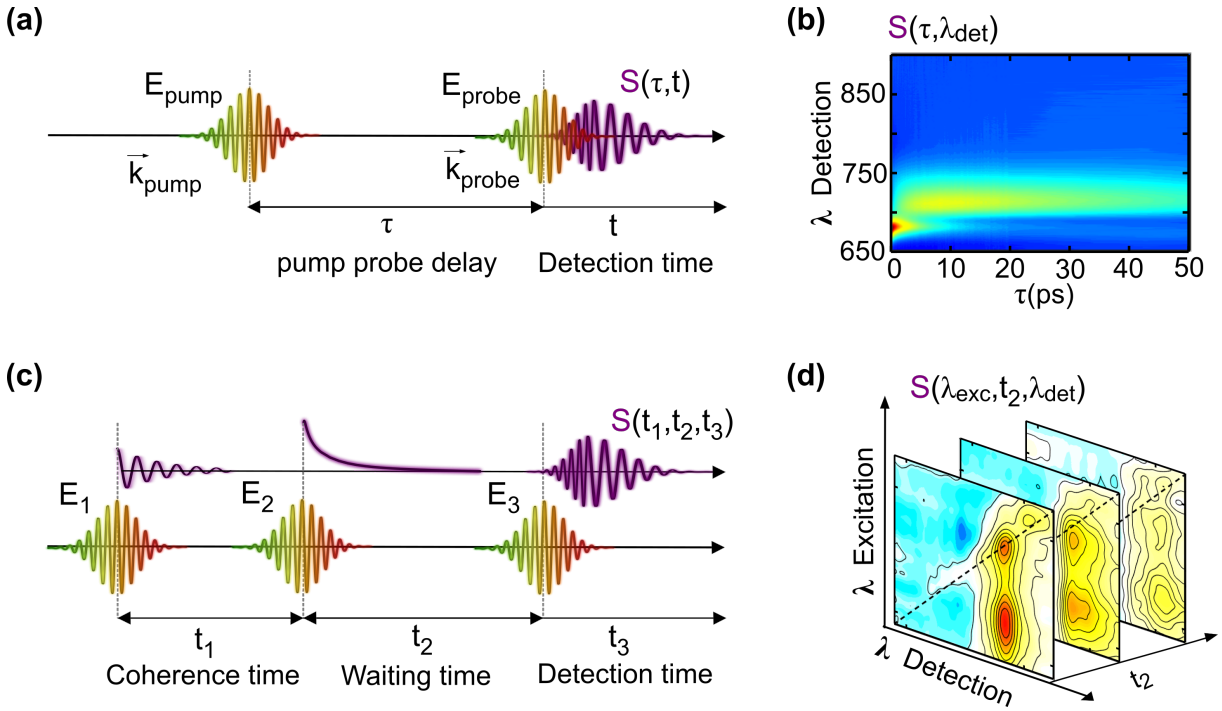

Figure 2: (a) Pulse sequence in a pump probe spectroscopy experiment where $\vec{k}_{pump}$ and $\vec{k}_{probe}$ are the wavevectors of the pump (E_{pump}) and probe (E_{probe}) laser pulses and τ is the delay between them. The signal $S(\tau, t)$ (violet) represents the emission from the sample after the two pulses interactions; (b) 2D map representation of the pump probe signal obtained by scanning the delay τ and where the detection axis t is Fourier transformed via spectrometer in order to get λ_{det} axis; (c) Pulse sequence (E_1, E_2 and E_3) in Two-Dimensional Electronic Spectroscopy (2DES) technique; in the bottom the delays between the pulses (t_1,t_2 and t_3) are specified; on the top is reported a possible third order non linear signal emitted from the sample after each delays. (d) Example of the 2DES spectra obtained after that the signal along t_1 and t_3 time axis are Fourier transformed to get the λ_{exc} and λ_{det} axis.

represented as a 2D map. The drawback here is that the signals related to different phenomena are overlapped to each other due to the simultaneous multifrequncies excitation induced by the pump pulse. It is possible also to use a narrowband pump pulse in order to study a specific phenomena resulting from a specific frequency excitation; however this approach represent a limitation in terms of temporal resolution (typically larger than 100fs). In this view, Two-Dimensional Electronic Spectroscopy (2DES) technique comes into the spotlight because it combines high excitation spectral and temporal resolution by generating time-resolved excitation/detection frequency 2D spectrum. The 2D signal provides an overview of the entire set of mechanisms that take place in femto-picoseconds time scale. Specifically, in this technique, a system interacts with three delayed laser pulses to produce a third order nonlinear signal as a function of the delays between the

them. The delay between the first and second pulse is called coherence time (labeled as t_1), the delay between the second and the third pulse is called population time or waiting time (labeled as t_2) and the time after the third pulse is called detection time (labeled as t_3)[16]. Figure 2a shows the pulse sequence accompanied with an example of the generated signal (violet) after each interaction. The first interaction generates a coherence state that manifests as an oscillatory signal that rapidly decay along delay t_1. The second interaction brings the system in a population state that relaxes during time t_2. The coherence state generated after the third interaction, provides the emission of the third order non linear signal mentioned before $S(t_1, t_2, t_3)$. The calculation of the 2D spectra is obtained by Fourier transforming the signal along t_1 and t_3 time delays to recover the excitation and detection frequency axis. The temporal evolution of the 2D map is detected by varying the population time t_2 [16]. The high temporal and spectral resolution mentioned before, is provided by using sub-20fs time compressed laser pulses and by recovering the excitation frequency axis.. Figure 2b shows an example of 2DES data measured at three different t_2 delays where each peak reflects a specific mechanism in the system. In particular, the position and the lineshape of the peaks can reveals different processes that are crucial in order to to characterized light harvesting systems.

Peaks in 2D spectra In 2D maps, the peaks can appear along the diagonal line where the excitation and detection frequencies are the same, or they can be located out of the diagonal line. In the first case, they reflect the steady state absorption spectrum. Completely different is the meaning of the peaks that stay out of the diagonal (cross peaks) where the excitation and detection frequency mismatch.Such peaks can represent energy/charge transfer mechanisms or coupling between different energy states. In order to distinguish these two effects, is necessary to study the temporal evolution of the cross peaks. Specifically if the decay of a diagonal peak associated with an excited state is followed by a rise time of a cross peak, it represents an EET process. This particular effect has been largerly observed in natural photosystems where the energy flows within different kind of Chls [5, 17, 18]. In the same way, we can observe charge transfer processes between two different materials as it is recently published for nanostructure systems [19] and transition metal dichalcogenide heterostructures [20]. When the cross peaks appear already at zero waiting time, we can observe a coupling between electronic states. This particular condition promotes a coherent superposition between the energy states by generating a signal along t_2 time which is modulated by this coherence. The presence and the study of this effects has been observed for molecular aggregates [21], semiconductors quantum wells [22] and polymers [23]. This evidence can be also exploit to define the structure of the system and assign the nature of the coupled states [24].

2D lineshape The possibility to measure the time-resolved transient absorption of the system as a function of excitation and detection frequencies, allows to represent each absorption peaks with a 2D lineshape. At waiting time closed to zero, such peaks show an elliptical shape elongated along the diagonal line where it is possible to assign two different spectral width. The one along the diagonal direction contains contribution from the inhomogeneous broadening generated by the interactions that each molecule experiences with the environment. This effect is reflected in the steady absorption spectrum where the linewidth is approximately reproduced as a convolution of sharper peaks modeled as Lorentzian functions [13]. The linewidth along the anti-diagonal direction shows a shorter width with respect to the diagonal one and it is associated with the homogeneous broadening [25, 26]. This particular spectral feature represents a local effect where each molecule interacts only with the neighborhood ones. The value of the this bandwidth is usually represented with 2γ where γ is defined as the dephasing rate [25]. This approach allows to direct estimate the dephasing time of the molecule calculated as the inverse of the parameter γ.
Another aspect that can be study by analyzing the linehape is the spectral diffusion effect. Such a phenomenon reflects how the system loose memory of the initial state due to both intermolecular and thermal-bath interactions. From the experimental point of view, this mechanism is reproduced in the 2D spectra as a variation of the lineshape during time t_2. Specifically, the shape changes from elliptical to circular where the diagonal and anti-diagonal linewidths are indistinguishable. The time in which this process take place gives a quantitative description of the spectral diffusion [27]. In order to implement both lineshape analysis (dephasing time and spectral diffusion), several methods are implemented and some of the will be explained later in this thesis.

0.3. Outlook of the thesis

In this thesis, I exploit 2DES technique to study natural and bio-inspired light harvesting systems in order to investigate their performances. For the natural part, I will focus the attention on the processes in which low-energy Chls are involved and their role during photosynthesis. For the bio-inspired part, I will show two different artificial light harvesting systems that are designed for two different goals. The first one is architecturally similar to a natural photosystem and it is designed to reproduce more efficiently the water oxidation reaction. The second one is designed to obtain energy transfer between two spatially separated molecules where the distance is in the order of μm. Following there is a summary of the entire thesis divided by each chapter.

- Chapter 1: This chapter is divided in two part: In the first part I will show the theoretical calculations to derive the response function of a system after multi-pulse interactions. Such expression is then characterized for the 2DES experiment by giving a graphical representation with the double sided Feynman diagrams. In the second part I will introduce the different experimental implementations adopted to perform 2DES measurements. In particular, I will focus on our experimental apparatus that is characterized by a partially collinear geometry for the laser pulses and a device based on birefringent wedges.
- Chapter 2: In this chapter I will explore several of these aspects by exploiting the 2DES experimental and theoretical results of three simple molecules. In particular I will study the origin of the signals for the Perylene Bisimide (PBI) dye, energy transfer and vibrational coherences in free base Porphyrin and lineshapes of Lumogen F-Orange (LFO) dye.
- Chapter 3: After showing the studies of simple molecules, in this part of the thesis we analyze more complicated systems. In particular I will study natural light harvesting systems isolated from higher plants and cyanobacteria in order to investigate the energy transfer pathways. The temporal characterization of the processes is obtained by using global analysis algorithm.
- Chapter 4: In this chapter I will investigate via 2DES and pump probe spectroscopy techniques two different bio-inspired light harvesting systems synthesized in the laboratory. The first one is designed based on the natural photosystems in order to perform the water splitting. In this case, the photophysics of the system is studied by tracking the charge dynamics. The second systems consist of two spatially separated organic semiconductors confined in a optical microcavity. The goal of this structure is to performed energy transfer between molecules when they are distanced by few μm.
- Chapter 5 In the last chapter we report the summary of the entire work by evidencing the main results obtained from each natural or artificial light harvesting systems and the future perspectives.
- Appendix A In this appendix we report a table with the characteristics of the samples discussed in this thesis and the experimental parameters adopted to perform the measurements.
- Appendix B Here we report the basic mathematical architecture in order to performed the global analysis on time-resolved ultrafast spectroscopy data

1 | Two-Dimensional Electronic Spectroscopy

1.1. Theoretical Framework

In this section we present a theoretical approach to derive an analytic expression of the response function of a system in a non linear experiment. In general, when an electromagnetic field interacts with a system, it excites the charges to get molecular vibrations. In this way, the field creates a non-equilibrium charge distribution that vibrate synchronously with the phase of the electromagnetic field. Such a distribution is usually refereed as a macroscopic polarization that temporally evolves according to the molecular response. When the system correspond to an isolated molecule, the macroscopic polarization can be easily derived from the wavefunction formalism [28], but when the system correspond to an ensemble of condensed molecules, that formalism is not sufficient. In this specific case each molecule of the system posses energetically different excited states and the macroscopic polarization is given by the interfere of the vibrational motion of each molecule. The formalism to describe this effect required statistical mechanism to take into account all possible effects. The suited formalism adopted to describe these system is the Density Matrix that visualize the state of the system with a statistical average within the wavefunctions. Following we introduce this formalism and we derive the expression of the response function by using the perturbation theory.

1.1.1. Density Matrix approach

Typically the system studied in a non linear optical experiments are ensemble of condensed molecules for which the wavefunction description result very complicated to evaluate the interaction with an electromagnetic field. In this view the density matrix operator allow a statistical description of the ensemble and it is commonly use to describe systems in non linear experiments. To motivate the introduction of the density operator, let us consider a pure state,which is, a quantum mechanical state of a single molecule that can be described

by a single wavefunction$|\psi>$, the temporal evolution of which is given by Schrödinger's equation.

$$i\hbar\frac{\partial|\psi(r,t)>}{\partial t} = H|\psi(r,t)> \tag{1.1}$$

Where $\hbar$ is the Planck's constant divided by 2π and H is the Hamiltonian of the system. We assume the existence a set of eigenstates $|\phi_k>$, such that:

$$<\phi_i|\phi_j>=\delta_{i,j} \tag{1.2}$$

which forms orthonormal basis; under this assumption, any wavefunction may be expanded according to:

$$|\psi>=\sum_{k=0}^{\infty} c_k|\phi_k(r)>\exp(-i\omega_k t) \tag{1.3}$$

where $|c_k|^2$ are the quantum probability to find the system in the eigenstate k. The density matrix of a system described by the wavefunction $\psi(t)$ is defined as [13]:

$$\rho(t) = |\psi(t)><\psi(t)| \tag{1.4}$$

Using equation 1.3, we can write it as:

$$\rho(t) = \sum_{mn} = c_n c_m(t)|\phi_n><\phi_m| \tag{1.5}$$

here it is possible recognize that the density operator can be expressed in the matrix form, where each element is:

$$\rho_{mn} = c_n(t)c_m^*(t) \tag{1.6}$$

The density operator can be used as an alternative description of the quantum system; indeed, the expectation value of any operator can be described only in terms of ρ, with no reference to the wavefunction:

$$<A>=<\psi(t)|A|\psi(t)>=\sum_m c_m^* \sum_n c_n <\phi_m|A|\phi_n>=\sum_{mn} c_m^* c_n A_{mn} \tag{1.7}$$

substituting with the formula 1.6 we get

$$<A>=\sum_{mn} = \rho_{mn}A_{mn} = Tr(\rho A) \tag{1.8}$$

This relation was derived for a pure state, but it is possible write it for a mixed state in

which the wavefunction $|\psi_i>$ can be found with a probability of p_i:

$$\rho = \sum_{i=1}^{n} p_i |\psi_i >< \psi_i| \tag{1.9}$$

where n is the number of the all possible states and p_i is the probability to have the system in the i-state. The definition of the expectation value of a generic operator A is the statistical average of the expectation values of this operator per each state of the system.

$$< A >= \sum_{i=1}^{n} p_i < \psi_i|A|\psi_i > \tag{1.10}$$

We can manipulate this expression , considering the following property of a complete set of eigenstates $|\phi_k>$.

$$I = \sum_{k} |\phi_k >< \phi_k| \tag{1.11}$$

Where I is the identity operator. Applying the identity operator from equation 1.11 in A from the right we obtain:

$$< A >= \sum_{i=1}^{n} p_i < \psi_i|AI|\psi_i >= \sum_{i=1}^{n} p_i < \psi_i|A \sum_{j} |\phi_j >< \phi_j||\psi_i >$$

$$= \sum_{j} < \phi_j| \sum_{i} p_i |\psi_i >< \psi_i|A|\phi_j >$$

$$= \sum_{j} < \phi_j|\rho A|\phi_j >= Tr(\rho A) \tag{1.12}$$

We can note that this formula has the same form of the formula for a pure state 1.8, so this is a general expression to calculate the expectation value for any operator.

Liouville Equation

Besides computing the expectation values of operators, we would like to describe the temporal evolution of a quantum mechanical system using the density operator only [28]. We start the calculation taking the time derivative of ρ

$$\frac{\partial \rho}{\partial t} = \sum_{i} p_i \left(\frac{\partial |\psi_i >}{\partial t} < \psi_i| + |\psi_i > \frac{\partial < \psi_i|}{\partial t} \right) \tag{1.13}$$

The time derivatives of the wavefunctions are given by Schroedinger's equation (1.1)

$$\frac{\partial \rho}{\partial t} = \sum_i p_i \left(\frac{1}{i\hbar} H|\psi_i >< \psi_i| - \frac{1}{i\hbar} |\psi_i >< \psi_i| H \right)$$

$$= \frac{1}{i\hbar} \left[H \sum_i p_i |\psi_i >< \psi_i| - \sum_i p_i |\psi_i >< \psi_i| H \right]$$

$$i\hbar \frac{\partial \rho}{\partial t} = [H, \rho] \tag{1.14}$$

The compact term $[H, \rho]$ is defined as commutator between H and ρ operators and the last expression is also called Liouville Equation which represent the equivalent of the Schrödinger's equation in case of wavefunction description[13].

Matrix Elements of ρ

Let us now consider each element of the density matrix and their meaning. By considering the definition of the density operator, the matrix elements are defined as:

$$\rho_{lm} =< \phi_l|\rho|\phi_m >= \sum_{i=1}^{n} p_i < \phi_l|\psi_i >< \psi_i|\psi_m > \tag{1.15}$$

Now we can manipulate this expression expanding the wavefunctions $|\psi_i >$ as we made in the formula 1.3

$$|\psi >= \sum_{j=0}^{\infty} c_j |\phi_j(r) > \exp(-i\omega_j t) \tag{1.16}$$

The orthonormal basis of the of the eigenstates imply that only the terms with index j=l and j=m survive in the sum with index j. The expression that we obtain is:

$$\rho_{lm} = \sum_{i=1}^{n} p_i c_{il} e^{-i\omega_l t} c_{im}^* e^{i\omega_m t}$$

$$= \sum_{i=1}^{n} p_i c_{il} c_{im}^* e^{-i(\omega_l - \omega_m)t} \tag{1.17}$$

We can now characterize this expression for a diagonal element of the matrix:

$$\rho_{jj} = \sum_{i=1}^{n} p_i c_{ij} c_{ij}^* = \sum_{i=1}^{n} p_i |c_{ij}|^2 \tag{1.18}$$

This expression is the statistical average of the quantum probability to find molecules in a certain eigenstate $|\phi_j>$. If the system has $\rho_{jj} = 1$ means that all the molecules of the ensemble stay in the $|\phi_j>$ eigenstate and it is usually refereed as population state. The representation of the density operator in this case is $|\phi_j><\phi_j|$. In case of off-diagonal elements, the expression becomes:

$$\rho_{lm} = \sum_i p_i c_{il} c_{im}^* e^{-i(\omega_l - \omega_m)t} \tag{1.19}$$

This expression represent the probability to find the ensemble in a coherent superposition between two eigenstate ($|\phi_l><\phi_m|$) and the temporal evolution shows an oscillation with frequency $\omega_l - \omega_m$ (energy difference between the two energy states). In this case the ensemble is in a coherent state.

1.1.2. Time evolution of an unperturbed system

Let us consider for simplicity a two level systems which energetic levels are identified with time independent eigenstate function $|0>$ the ground state and $|1>$ the excited state. Considering the unperturbed situation when the system is excited with impulsive electromagnetic field with a Delta Dirac temporal lineshape: $E(t) = E\delta(t)$, the Hamiltonian of the system can be represented with the following matrix:

$$H = \begin{pmatrix} \epsilon_0 & 0 \\ 0 & \epsilon_1 \end{pmatrix} \tag{1.20}$$

where ϵ_0 and ϵ_1 are the energies that correspond to the ground state and excited state. The time evolution of the density matrix can be obtained as solution of the Louville equation:

$$\begin{aligned} \frac{d}{dt}\begin{pmatrix} \rho_{00} & \rho_{01} \\ \rho_{10} & \rho_{11} \end{pmatrix} &= -\frac{i}{\hbar}\left[\begin{pmatrix} \epsilon_0 & 0 \\ 0 & \epsilon_1 \end{pmatrix}\begin{pmatrix} \rho_{00} & \rho_{01} \\ \rho_{10} & \rho_{11} \end{pmatrix} - \begin{pmatrix} \rho_{00} & \rho_{01} \\ \rho_{10} & \rho_{11} \end{pmatrix}\begin{pmatrix} \epsilon_0 & 0 \\ 0 & \epsilon_1 \end{pmatrix}\right] \\ &= -\frac{i}{\hbar}\begin{pmatrix} 0 & (\epsilon_0 - \epsilon_1)\rho_{01} \\ (\epsilon_1 - \epsilon_0)\rho_{10} & 0 \end{pmatrix} \end{aligned} \tag{1.21}$$

This matrix equation can be solved element by element obtaining:

$$\dot{\rho}_{00} = 0 \Rightarrow \rho_{00}(t) = \rho_{00}(0) \tag{1.22}$$

$$\dot{\rho}_{11} = 0 \Rightarrow \rho_{11}(t) = \rho_{11}(0) \tag{1.23}$$

$$\dot{\rho}_{01} = -\frac{i}{\hbar}(\epsilon_0 - \epsilon_1)\rho_{01} \Rightarrow \rho_{01}(t) = e^{-i\omega_{01}t}\rho_{01}(0) \tag{1.24}$$

$$\dot{\rho}_{10} = -\frac{i}{\hbar}(\epsilon_1 - \epsilon_0)\rho_{10} \Rightarrow \rho_{01}(t) = e^{i\omega_{01}t}\rho_{10}(0) \tag{1.25}$$

where $\omega_{01} = (\epsilon_0 - \epsilon_1)/\hbar$. The two diagonal elements are real number and they refer to population states; on contrary, the elements out of the diagonal oscillates with frequency obtained from the energy difference between the states. In order to get a correct description of the time-evolution of the system, it is necessary to include two decay steps. The first one is usually called population time T_1 and represents the time in which the system relax from state $|1>$ to ground state $|0>$ and it will affect only diagonal elements of the density matrix. The second time is correlated to the decay of the oscillations called dephasing time T_2 that will affect only the off-diagonal elements.

$$\rho_{11}(t) = \rho_{11}(0)e^{-t/T_1} \tag{1.26}$$

$$\rho_{00}(t) = 1 - \rho_{11}(t)$$

$$\rho_{01}(t) = e^{i\omega_{01}t}e^{-t/T_2}\rho_{01}(0)$$

$$\rho_{01}(t) = e^{-i\omega_{01}t}e^{-t/T_2}\rho_{10}(0)$$

The temporal evolution of ρ can be visualized by Bloch vector whose x, y and z components are defined in the following way:

$$B_z = \rho_{00} - \rho_{11} \tag{1.27}$$

$$B_x = -(\rho_{01} + \rho_{10}) \tag{1.28}$$

$$B_y = i(\rho_{01} - \rho_{10}) \tag{1.29}$$

The z component of the vector $\vec{B}$ depends only on the population states and the x and y components are only related to coherence states (elements out of the diagonal). Figure 1.1a shows the temporal evolution of the Bloch vector in case of one molecule. Before the interaction of the pulse, we can assume that all the molecules in the system are in the ground states and the value of the coefficients are $\rho_{00} = 1$ and $\rho_{11} = 0$. This brings the Bloch vector to have one component along z direction. Immediately after the pulse interaction ($t = 0$) the vector moves along the z-y plane and start to rotate with proceed motion around the z axis. This rotation is responsible of the emitted field from the sample which corresponding to the macroscopic polarization; specifically as will shown later, this

polarization is proportional to the x component of the Bloch vector ($P(t) \propto B_x$). By

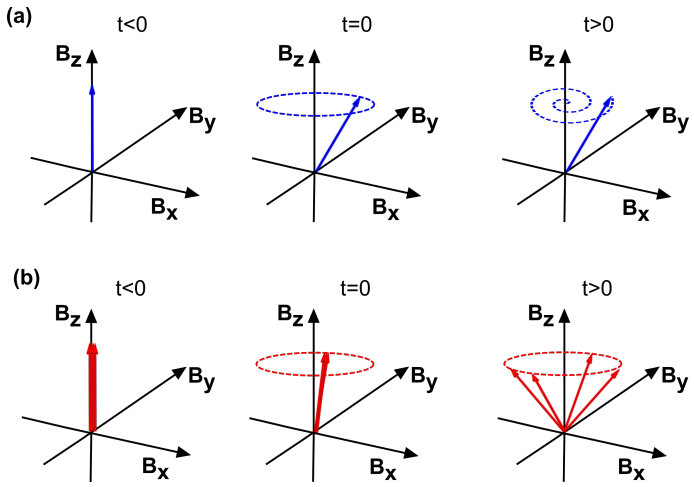

Figure 1.1: Temporal evolution of the Bloch vector in case of a single molecule (a) and in case of an ensamble of molecules (b)

adding the population and dephasing time in the description, Bloch vector performs a spiral around the z axis that at $t = \infty$ it will be align along the z direction, which means that the system is back to the ground state. This graphical method is particularly useful to visualize the macroscopic polarization that comes from an ensemble of molecules. In this case, the total polarization is given by the sum of each molecule contribution which can be represented each one as a Bloch vector. Figure 1.1b shows the temporal evolution of the Bloch vectors in the ensemble case in which the vector that describe the entire system is given by the sum of all the contributions. In yhis case, after the interaction, the signal emitted from each molecule constructively interfere and all the vectors are overlapped in the diagram. Following this, each vector start to rotate around z axis with different frequencies and the polarization of each molecule destructively interfere by producing a rapid decay of the macroscopic polarization

Macroscopic Polarization

As it was mentioned in the previous paragraph, the oscillation emitted from the ensemble correspond to the macroscopic polarization that evolves according to the response function of the system. In general, when an electric field interacts with a system, it generates delocalized charge distribution that oscillate in phase with the frequency of the field. This leads the system to emit an electromagnetic wave that correspond to the sum of the polarization contribution of each molecule. In general the polarization is correlated with

the external electric field E by the following relation:

$$\vec{P}(t) = \epsilon_0 \chi \vec{E} \tag{1.30}$$

where ϵ_0 is the dielectric constant in the vacuum, χ is the electric susceptibility tensor. When the electric field is enough intense, the susceptibility can not be approximate as a number, but nonlinear terms with higher order must be included in the expression 1.30 which can be rewritten as:

$$P(t) = \epsilon_0(\chi^{(1)}E + \chi^{(2)}E^2 + \chi^{(3)}E^3 + ...) \tag{1.31}$$

where the terms $\chi^{(n)}$ represent the n-order susceptibility. By applying the density matrix formalism, the polarization can be assumed proportional to the expectation value of the dipole moment μ:

$$P(t) \propto \langle \mu \rangle = Tr(\mu\rho(t)) \tag{1.32}$$

In the case of two level system, the matrix related to the dipole moment contains only off-diagonal elements that correspond to a linear combination between the ground the excited state.

$$\mu = \begin{pmatrix} 0 & \mu_{01} \\ \mu_{10} & 0 \end{pmatrix} \tag{1.33}$$

In this formula we can consider as first approximation that the two off-diagonal value are indistinguishable and the final expression of the macroscopic polarization is:

$$P(t) = Tr\left[\begin{pmatrix} 0 & \mu_{01} \\ \mu_{01} & 0 \end{pmatrix}\begin{pmatrix} \rho_{00} & \rho_{01} \\ \rho_{10} & \rho_{11} \end{pmatrix}\right] = \rho_{10}\mu_{01} + \rho_{01}\mu_{01} \tag{1.34}$$

As we already mentioned with the Bloch vector, the polarization depends only on the off-diagonal elements of the density matrix, providing an emission of an electromagnetic field typically called free induction decay.

1.1.3. Response function of a System (Interaction picture)

Let us now summarize the crucial points about the density matrix description: (i) the density matrix formalism is particularly suited to describe ensemble of condensed molecules because it includes a statistical description of the states; (ii) The response function of the system, followed by an interaction with an electric field, evolves according to the macroscopic polarization generated in the system; (iii) such a polarization is proportional to the expectation value of the dipole moment which expression can be written by the

formula 1.32. In order to retrieve a general expression of the of the macroscopic polarization in case of multi interactions, is necessary to solve the Louville equation in which the Hamiltonian of the system has the following expression:

$$H(t) = H_0 + H^{'}(t) = H_0 - \mu E(t) \tag{1.35}$$

where H_0 is the time independent Hamiltonian of the unperturbed system and $H^{'}$ is the time dependent operator that represent the interaction with an external field. In case of optical wavelength larger with respect the molecular size, the interaction operator can be written as the product of dipole moment μ and the external electric field. By considering this Hamiltonian of the system, the Louiville equation can be solved by applying the perturbation theory, which calculation and formalism are reported by Mukamel [28]. From this approach, the time-dependent expression of the density matrix can be written in the following way:

$$\rho(t) = \rho^{(0)}(-\infty) + \sum_{n=1}^{\infty} \rho^{(n)}(t) \tag{1.36}$$

where $\rho^{(n)}$ are the n-order density matrix generated from n interactions with the external field and it assumes the following expression:

$$\rho^{(n)}(t) = \left(\frac{-i}{\hbar}\right)^n \int_{t_0}^{t} d\tau_n \int_{t_0}^{\tau_n} d\tau_{n-1} ... \int_{t_0}^{\tau_2} d\tau_1 E(\tau_n)E(\tau_{n-1})...E(\tau_1)$$

$$U(t,t_0)[\mu(\tau_{n-1}), ...[\mu(\tau_1), \rho(-\infty)]..]]U^{\dagger}(t,t_0) \tag{1.37}$$

In this formula, t_0 represent the time before the interaction with the external field (the system is unperturbed) and the operator $U(t,t_0)$ ($U^{\dagger}(t,t_0)$ the Hermitian conjugate) is called time evolution operator defined as $U(t,t_0) = e^{-i\frac{H_0}{\hbar}t}$. The terms μ and $\rho(-\infty)$ within the squared parenthesis are the interaction dipole moment and the interaction density matrix defined as: $U^{\dagger}(t,t_0)\mu U(t,t_0)$ and $U^{\dagger}(t,t_0)\rho U(t,t_0)$. Figure 1.2 shows a simple way in which the expression 1.37 can be interpreted; specifically, the system interacts with n electromagnetic fields that arrive to the sample at time instants τ_1, τ_2,.....τ_n. In our context, these fields are sub 50 femtoseconds laser pulses that are delayed by time intervals ($\tau_1 = 0, t_1 = \tau_2 - \tau_1, ..., t_n = t - \tau_n$). The generic n-order non linear polarization can be expressed by exploiting the expression 1.32 [25]:

$$P^{(n)}(t) \propto Tr[\rho^{(n)}\mu] \tag{1.38}$$

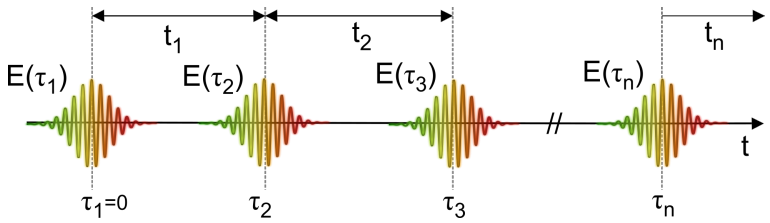

Figure 1.2: Temporal representation of n interactions with the systems in which τ_i correspond to the time instant in which the field $E(\tau_i)$ interacts with the system and t_i represent the time intervals between the interactions

which expression as a function of time intervals becomes:

$$P^{(n)}(t) \propto \int_0^\infty dt_n \int_0^\infty dt_{n-1}.. \int_0^\infty dt_1 E(t-t_n)..E(t-t_n-t_{n-1}..t_1)R^{(n)}(t_n...t_1) \quad (1.39)$$

where the $R^{(n)}$ is the n-order non linear response function defined as:

$$R^{(n)}(t_n...t_1) = \left(\frac{-i}{\hbar}\right) Tr\Big(\mu(t_n+t_{n-1}+...t_1)[\mu(t_{n-1}+..t_1),..[\mu(0),\rho(-\infty)]..]\Big) \quad (1.40)$$

This expression contains 2^n terms that correspond to the interactions with the fields $E(t-t_n)$, $E(t-t_n-t_{n-1})$, ..., $E(t-t_n-....-t_1)$. Here we can note that the last interaction described with the term $\mu(t_n+t_{n-1}+...t_1)$ is the out of the commutator because it describe the emitted field after the n interactions at time $t_n+t_{n-1}+...+t_1$. The first n inetractions contribute to generate the $\rho^{(n)}$ term that describe the system in a non equilibrium state.

Linear Response Function

We start the analysis of the response function with the simplest case: two level system that interacts with one laser pulse. This situation correspond to fix the non linear order n =1 and the non linear response function assumes the following form:

$$R^{(1)}(t_1) = iTr\big(\mu(t_1)\mu(0)\rho(-\infty)\big) - iTr\big(\rho(-\infty)\mu(0)\mu(t_1)\big) \quad (1.41)$$

This is called linear response function and it is composed of two terms that show the following differences: the position of the dipole moment operator with respect the density matrix and their sign. In order to understand the meaning of these terms, we now calculate step by step the temporal evolution of the density matrix in both situation, considering the following two assumptions:

(i) Before the interaction the system is in the ground state and the corresponding density matrix is:

$$\rho(-\infty) = \begin{pmatrix} 1 & 0 \\ 0 & 0 \end{pmatrix} \tag{1.42}$$

(ii) The dipole moment operator is off-diagonal and, for simplicity, we avoid units in the expression:

$$\mu = \begin{pmatrix} 0 & 1 \\ 1 & 0 \end{pmatrix} \tag{1.43}$$

Let us now calculate the first term of the response function; specifically after the first interaction with the dipole moment, we obtain:

$$i\mu(0)\rho(-\infty) = i \begin{pmatrix} 0 & 1 \\ 1 & 0 \end{pmatrix} \begin{pmatrix} 1 & 0 \\ 0 & 0 \end{pmatrix} = \begin{pmatrix} 0 & 0 \\ i & 0 \end{pmatrix} \tag{1.44}$$

This interaction bring the system in a coherence state (01) because only the term ρ_{10} is different from zero. From this point, the system propagate with the unperturbed Hamiltonian which effect consist of a oscillatory term $e^{-i\omega_{01}t_1}$ as we already seen in the previous paragraph (equation 1.25). In this case the density matrix becomes:

$$i\mu(0)\rho(-\infty) \xrightarrow{t_1} \begin{pmatrix} 0 & 0 \\ ie^{-i\omega_{01}t_1} & 0 \end{pmatrix} \tag{1.45}$$

This matrix represent a formation of a coherence state that oscillate in t_1 with a frequency ω_{01}. If we repeat the same calculation for the second term of the R^1 we get the following result:

$$-i\rho(-\infty)\mu(0) \xrightarrow{t_1} \begin{pmatrix} 0 & -ie^{i\omega_{01}t_1} \\ 0 & 0 \end{pmatrix} \tag{1.46}$$

We can notice that, by applying the dipole moment on the right side of the density matrix, it will generate a coherence state (01) which is the complex conjugated of the other. By combining both results we obtain the expression of $\rho^{(1)}$:

$$\rho^{(1)} = \begin{pmatrix} 0 & -ie^{i\omega_{01}t_1} \\ ie^{-i\omega_{01}t_1} & 0 \end{pmatrix} \tag{1.47}$$

Figure1.3 shows the expression and the graphical representation of the Bloch vector calculated for $\rho^{(1)}$ in which the z-component is equal to zero and the vector rotates in the x-y plane from which a signal will be emitted. In order to have a complete representation of the density matrix, also the 0-order term must be included. On the right side of the

figure, we show the Bloch vector for $\rho^{(0)} + \rho^{(1)}$ where the z-component is different from zero and it still rotate in the x-y plane. We can now proceed with the calculation of the

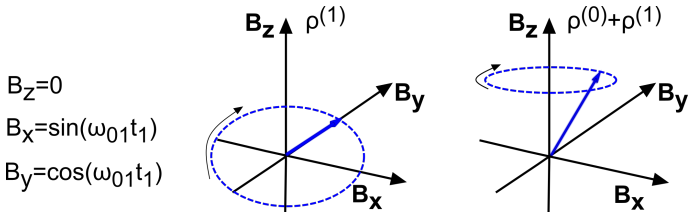

Figure 1.3: Bloch vector value and representation of the first order non linear density matrix $\rho^{(1)}$(on the left) and bloch vector of the density matrix including zero order (on the right)

linear response function by considering the last interaction with the dipole moment $\mu(t_1)$ which represent the emitted field. For the first term we get:

$$i\mu(t_1)e^{-i\omega_{010}t_1}\mu(0)\rho(-\infty) = \begin{pmatrix} ie^{-i\omega_{01}t_1} & 0 \\ 0 & 0 \end{pmatrix} \xrightarrow{Tr(.....)} = ie^{-i\omega_{01}t_1} \tag{1.48}$$

After the second interaction with the dipole moment, the system relaxes to the ground state with an emitted signal that oscillate with frequency ω_{01}. By repeating this procedure also for the complex conjugated part and combine both contribute we obtain the final expression of the linear response function:

$$R^{(1)}(t_1) \propto \sin(\omega_{01}t_1) \tag{1.49}$$

Double-sided Feynman diagrams

We now introduce the double-sided Feynman diagrams which is a graphical representation of the temporal evolution of the density matrix that is particularly useful in case of multi interaction picture. This method use two vertical lines to represent the temporal evolution of the $|ket>$ (left side) and the $<bra|$ (right side) of the density matrix. The interactions with the external fields are represented with tilted arrows and the population or the coherence states after each interaction must be indicated with the respective matrix element. By expressing the electric field in the form: $E(t) = E_0(t)(e^{-i\omega t+i\vec{k}\vec{r}} + e^{+i\omega t-i\vec{k}\vec{r}})$, the interaction arrows that point to the right represent an interaction with a field $E(t) \propto e^{-i\omega t+i\vec{k}\vec{r}}$ or its complex conjugated if it point to the left $E(t) \propto e^{+i\omega t-i\vec{k}\vec{r}}$. These arrows represent an excitation when they are point to the system; on contrary, they represent an emission from the system. The last interaction has a different meaning with respect to the others because it represents the emission (usually indicated with dashed line) and the system must relax in a population state. Figure1.4 shows the Feynman diagrams of both

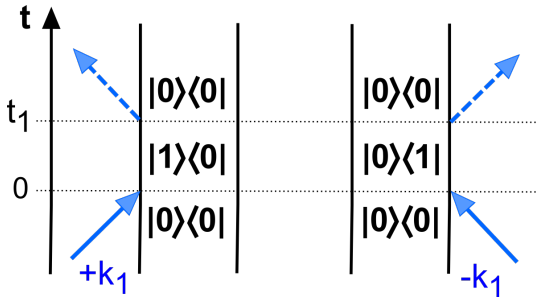

Figure 1.4: Feynman diagrams obtained from the two terms in the linear response function: on the left $Tr(\mu(t_1)\mu(0)\rho(-\infty))$ and on the right $-Tr(\rho(-\infty)\mu(0)\mu(t_1))$

terms in the linear response function. The first term is represented on the left side of the figure in which both dipole interactions are on the $|ket>$ (left side with respect to the density matrix). After the first interaction, the system is in a coherence state represented by the matrix element $|1><0|$. The second dipole interaction bring the system back to the ground state ($|0><0|$) by emitting a signal (blue dashed line). The second term of the linear response function is represented on the right side of the figure and it is mirror imaged with respect the other. For this reason, when there are two complex conjugated term, we can just evaluate one of them; typically the one that emits from the $|ket>$. In the following section we extend this analysis for the third order non linear response function which is the one that can be achieve with two-dimensional spectroscopy (2DES) experiment.

1.1.4. 2DES Response Function

Third order response function: Rephasing and non Rephasing

In this section we will try to derive the analytical expression of the system when two-dimensional electronic (2DES) experiment is performed. In 2DES technique, a system interacts with three delayed laser pulses and they allow to explore the third order non linear term of the response function. By using the same assumption adopted for the linear response function, the total electric field is given by the sum of three terms that identified the three pulses:

$$\begin{aligned} E(t) = E_1(t)(e^{-i\omega t+i\vec{k_1}\vec{r}} + e^{+i\omega t-i\vec{k_1}\vec{r}})+ \\ E_2(t)(e^{-i\omega t+i\vec{k_2}\vec{r}} + e^{+i\omega t-i\vec{k_2}\vec{r}})+ \\ E_3(t)(e^{-i\omega t+i\vec{k_3}\vec{r}} + e^{+i\omega t-i\vec{k_3}\vec{r}}) \end{aligned} \tag{1.50}$$

where k_1,k_2 and k_3 are the wave vector of each electric fields. The first pulse generates a coherence state that evolves during time interval t_1 usually called coherence time; specif-

ically this interaction produce a macroscopic polarization that decay with the dephasing time T_2. The second pulse generates a population state that evolving during time interval t_2 (called waiting time). This temporal evolution is characterized by a decay T_1 (population time). The third pulse generates another coherence state that produce an emission as a function of the delays between the pulses. The expression of the third order response function can be recover from the equation 1.49 by fixing n =3:

$$R^{(3)}(t_3,t_2,t_1) = \big(-\frac{i}{\hbar}\big)^3 Tr\big(\mu(t_3+t_2+t_1)[\mu(t_2+t_1),[\mu(t_1),[\mu(0),\rho(-\infty)]]]\big) \propto \quad (1.51)$$

$$+iTr\big(\mu(t_3+t_2+t_1)\mu(t_2+t_1)\mu(t_1)\mu(0)\rho(-\infty)\big) \Rightarrow R_5$$

$$-iTr\big(\mu(t_3+t_2+t_1)\mu(t_2+t_1)\mu(t_1)\rho(-\infty)\mu(0)\big) \Rightarrow R_4^*$$

$$-iTr\big(\mu(t_3+t_2+t_1)\mu(t_2+t_1)\mu(0)\rho(-\infty)\mu(t_1)\big) \Rightarrow R_1^*$$

$$+iTr\big(\mu(t_3+t_2+t_1)\mu(t_2+t_1)\rho(-\infty)\mu(0)\mu(t_1)\big) \Rightarrow R_2$$

$$-iTr\big(\mu(t_3+t_2+t_1)\mu(t_1)\mu(0)\rho(-\infty)\mu(t_2+t_1)\big) \Rightarrow R_2^*$$

$$+iTr\big(\mu(t_3+t_2+t_1)\mu(t_1)\rho(-\infty)\mu(0)\mu(t_2+t_1)\big) \Rightarrow R_1$$

$$+iTr\big(\mu(t_3+t_2+t_1)\mu(0)\rho(-\infty)\mu(t_1)\mu(t_2+t_1)\big) \Rightarrow R_4$$

$$-iTr\big(\mu(t_3+t_2+t_1)\rho(-\infty)\mu(0)\mu(t_1)\mu(t_2+t_1)\big) \Rightarrow R_5^*$$

The final expression is the sum of four pair of complex conjugated terms labeled as R_1, R_2, R_4 and R_5. There are also terms called R_3 and R_6 but their meaning will be mention later in the text. In order to understand the meaning of the four terms, let us consider the simplest case of a two level system characterized by the states $|0>$ and $|1>$. The terms R_1, R_2 are called Rephasing signal and the pair R_4, R_5 are refereed as non-rephasing signals which reason will be clarified in the next paragraph. For simplicity, we just focus on one of the rephasing and non rephasing term (R_4 and R_1) from which we will recover mathematically the temporal evolution of the density matrix. There are important aspects that must be assumed and point out to perform the calculation of the density matrix and the emitted signal:

(i) we use the same assumption adopted for study the linear response function (equation1.42 and 1.43)

(ii) After each interaction, the system evolves with the unperturbed Hamiltonian ($e^{\pm i\omega_{01}t}$).

(iii) For simplicity, in these calculations we are not consider the temporal evolution along t_2 time which implies that no effects due to the population time T_1 are considered.

Let us start the calculation of the response function for the term R_4:

$$\begin{pmatrix} 1 & 0 \\ 0 & 0 \end{pmatrix} \xrightarrow{i\mu_0\rho} \begin{pmatrix} 0 & 0 \\ i & 0 \end{pmatrix} \xrightarrow{t_1} \begin{pmatrix} 0 & 0 \\ ie^{-i\omega_{01}t_1} & 0 \end{pmatrix} \xrightarrow{i\mu_0\rho\mu_1}$$

$$\begin{pmatrix} 0 & 0 \\ 0 & ie^{-i\omega_{01}t_1} \end{pmatrix} \xrightarrow{i\mu_0\rho\mu_1\mu_2} \begin{pmatrix} 0 & 0 \\ ie^{-i\omega_{01}t_1} & 0 \end{pmatrix} \xrightarrow{t_3}$$

$$\begin{pmatrix} 0 & 0 \\ ie^{-i\omega_{01}(t_3+t_1)} & 0 \end{pmatrix} \xrightarrow{Tr(...)} ie^{-i\omega_{01}(t_3+t_1)} \tag{1.52}$$

in which we used a simplify notation for $\rho(-\infty) = \rho$ and $\mu(t_i + t_{i-1}) = \mu_i$. We can now compute the calculation for the sum $R_4 + R_4^*$ by proceeding as we have done for the linear response function:

$$\begin{pmatrix} 1 & 0 \\ 0 & 0 \end{pmatrix} \xrightarrow{E_1} \begin{pmatrix} 0 & -i \\ i & 0 \end{pmatrix} \xrightarrow{t_1} \begin{pmatrix} 0 & -ie^{+i\omega_{01}t_1} \\ ie^{-i\omega_{01}t_1} & 0 \end{pmatrix} \xrightarrow{E_2}$$

$$\begin{pmatrix} 0 & 0 \\ 0 & sin(\omega_{01}t_1) \end{pmatrix} \xrightarrow{E_3} \begin{pmatrix} 0 & -ie^{+i\omega_{01}t_1} \\ ie^{-i\omega_{01}t_1} & 0 \end{pmatrix} \xrightarrow{t_3}$$

$$\begin{pmatrix} 0 & -ie^{+i\omega_{01}(t_3+t_1)} \\ ie^{-i\omega_{01}(t_3+t_1)} & 0 \end{pmatrix} \xrightarrow{Tr(...)Emission} sin(\omega_{01}(t_3 + t_1)) \tag{1.53}$$

Figure 1.5a shows the associated Bloch vector representation of the density matrix for R_4+ R_4^* signal. The system starts in the population state $|0>$ in which the Bloch vector has only a unit component along z direction. After the first interaction with the pulse (E_1) the system goes in a coherence state. By considering an ensemble of condensed molecules, after E_1, the bloch vectors of each molecule are align along the y-axis (constructive interference). At this point, the system evolves during time t_1 by generating a macroscopic polarization due to the sum of the polarization signals created by each molecule. In terms of Bloch representation, each vector rotate with different frequencies (different values of ω_{01}) which are indicated in the figure with different colors (red slower and violet the faster). This create a destructive interference and the macroscopic polarization rapidly goes to zero. The interaction with the second pulse E_2 bring the sample back in the population state; specifically in the state $|1 > \rightarrow B_z = -1$. For simplicity we consider the time interval $t_2 = 0$, which means that the second and the third pulse interacts with the system simultaneously. The Third pulse creates the same coherence state generated by the first pulse which implies that the bloch vectors will rotate in the same direction during time t_3 and the polarization remain out of phase. We now repeat the same calculations for

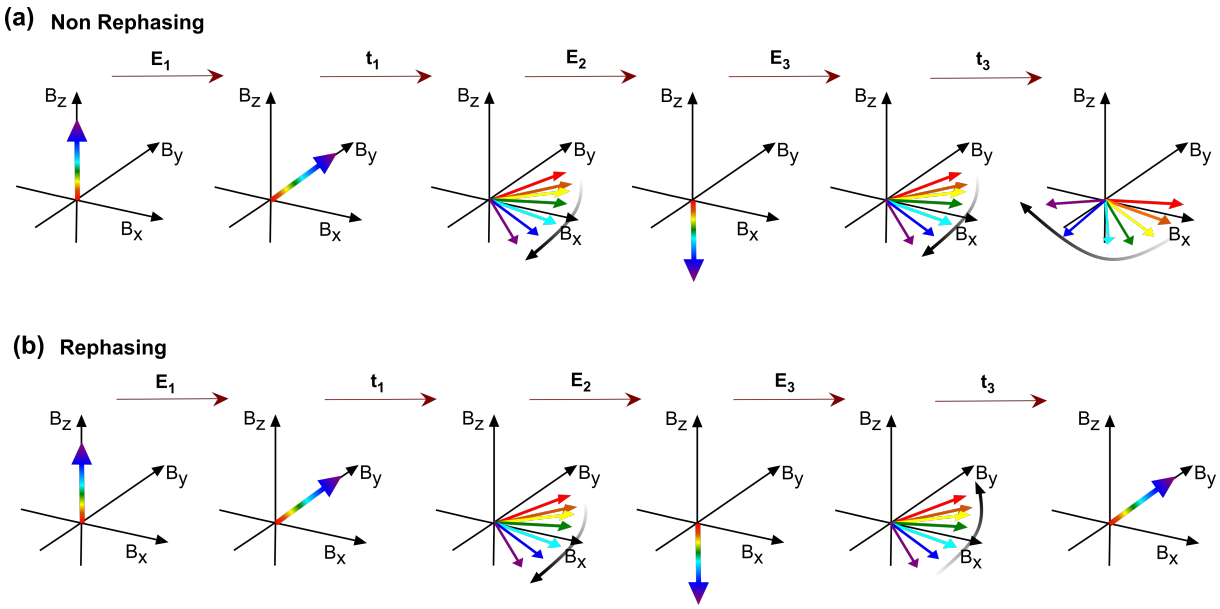

Figure 1.5: (a) Temporal evolution of the Bloch vector in case of non rephasing signal: after the interaction with the first electric field E_1 all the vectors are overlapped along the y-axis that during time t_1 dephase due to different velocities. The second field E_2 generates a population in state $|1>\rightarrow B_z = -1$ and the third field E_3 generates a coherence state in which the vectors are back rotating in the x-y plane in the same direction that they possesd during t_1. (b) Temporal evolution of the Bloch vectors in case of rephasing signal in which the only difference with respect (a) is that the third field E_3 induce a rotation in the opposite direction and at $t_3 = t_1$ the vectors are back in phase

$R_1 + R_1^*$:

$$\begin{pmatrix} 1 & 0 \\ 0 & 0 \end{pmatrix} \xrightarrow{E_1} \begin{pmatrix} 0 & +i \\ -i & 0 \end{pmatrix} \xrightarrow{t_1} \begin{pmatrix} 0 & +ie^{+i\omega_{01}t_1} \\ -ie^{-i\omega_{01}t_1} & 0 \end{pmatrix} \xrightarrow{E_2}$$

$$\begin{pmatrix} 0 & 0 \\ 0 & -sin(\omega_{01}t_1) \end{pmatrix} \xrightarrow{E_3} \begin{pmatrix} 0 & -ie^{-i\omega_{01}t_1} \\ +ie^{+i\omega_{01}t_1} & 0 \end{pmatrix} \xrightarrow{t_3}$$

$$\begin{pmatrix} 0 & -ie^{+i\omega_{01}(t_3-t_1)} \\ ie^{-i\omega_{01}(t_3-t_1)} & 0 \end{pmatrix} \xrightarrow{Tr(...)Emission} sin(\omega_{01}(t_3 - t_1)) \tag{1.54}$$

In this case, the third pulse create a coherence states which the complex conjugated with respect the one created by the first interaction. Figure 1.5b shows the bloch vectors related to the $R_1 + R_1^*$ and the last interactions induce the vectors to rotate (during time t_3) in the opposite direction with respect time t_1. When $t_3 = t_1$ the vectors come back in phase and it corresponds to have a delayed emission from the system usually called photon echo as is shown in figure1.6 For this reason the signal R_1 is called rephasing and

the R_4, where the polarizations remain out of phase during time t_3 is called non rephasing.

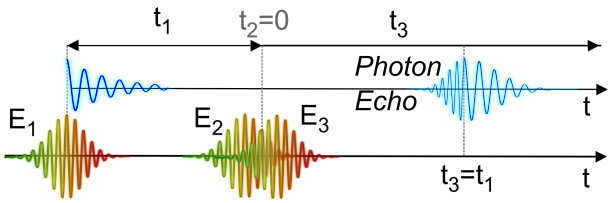

Figure 1.6: Laser pulse sequence in which time interval $t_2 = 0$ and above, the blue curve represent the signal emitted from the system in the rephasing case. At $t_3 = t_1$ the polarizarion of each molecule are back in phase, generating a signal called photon echo.

By following the same procedure performed for the linear response function, it is possible to build the double sided Feynman diagrams for every term in the equation 1.51. Figure1.7 shows the Feynman diagrams obtained for every terms (complex conjugated not included) and the terms R_3 and R_6 that comes out when a third energy level $|2>$ is added. On top of the figure there are the rephasing pathways (R_1, R_2 and R_3) in which the emission propagates along the same direction $k_R = -k_1 + k_2 + k_3$. The non rephasing pathways are shown in the bottom of the figure (R_4, R_5 and R_6) in which the emission propagates along the $k_{NR} = +k_1 - k_2 + k_3$ direction. We can now directly exploiting the diagrams to recover the expression of the response function, by including the dephasing and population decay. Here we report the derivation for R_4:
(i) $\boldsymbol{t < 0}$: The system starts from the ground state $\rho = |0><0|$
(ii) $\boldsymbol{t = 0}$: The system, after the first inetraction ($E(t) \propto e^{-i\omega t + i\vec{k}\vec{r}}$), goes in a coherence state and the off-diagonal element $\rho_{10} \propto i\mu_{01}$ is created. During the time interval t_1 the system evolving with the time-independent hamiltonian and the signal is damped with the dephasing time T_2:

$$\rho_{01} \propto i\mu_{01} e^{-i\omega_{01} t_1} e^{-t_1/T_2}$$

(iii) $\boldsymbol{t = t_1}$ The second interaction creates a population in the excited energy level$|1><1|$, by creating a diagonal element in the density matrix that decay with time T_1:

$$\rho_{11} \propto i\mu_{01}^2 e^{-i\omega_{01} t_1} e^{-t_1/T_2} e^{-t_2/T_1}$$

(iv) $\boldsymbol{t = t_1 + t_2}$ The third interaction generates another coherence state that dephase during time inetrval t_3:

$$\rho_{10} \propto i\mu_{01}^3 e^{-i\omega_{01} t_1} e^{-t_1/T_2} e^{-t_2/T_1} e^{-i\omega_{01} t_3} e^{-t_3/T_2}$$

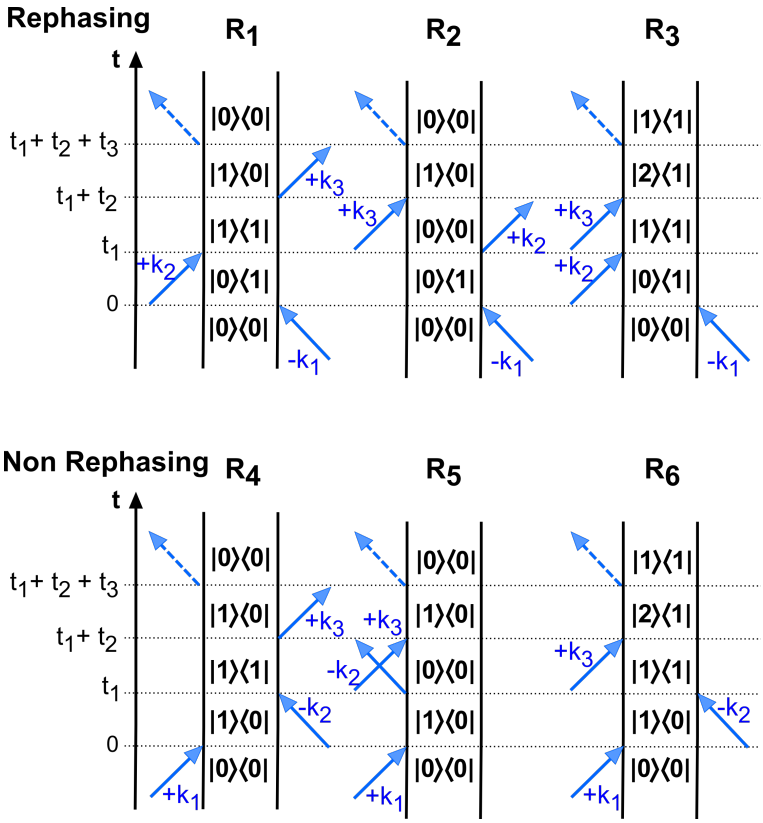

Figure 1.7: Feynman diagrams obtained from the third order response function: on top there are R_1, R_2 terms that corresponding to the rephasing signals. in the bottom there are R_4, R_5 terms that correspond to the non rephasing signals. The terms R_3 and R_6 are the rephasing and non rephasing terms that appear in the third order response function in case of three level system

(v) $\boldsymbol{t = t_1 + t_2 + t_3}$ There is the emission of the system and the response function is given by $Tr(\mu_{01}\rho)$:

$$R_4(t_3, t_2, t_1) \propto \rho_{10} i \mu_{01}^4 e^{-i\omega_{01}t_1} e^{-t_1/T_2} e^{-t_2/T_1} e^{-i\omega_{01}t_3} e^{-t_3/T_2}$$

From these diagrams, we are able to distinguish three different information which are useful in the next chapter for the interpretation of the 2DES data. The pathways R_1 and R_4, after the second interaction, show the system in the population state $|1><1|$ and the last interaction creates a coherence state between $|0>$ and $|1>$ that decay along time t_3 where the system relax back to the ground state. This kind of signal is called Stimulated Emission (SE). Pathways R_2 and R_5 are similar with respect the R_1 and R_4, the only difference is after the second interaction in which only the ground state $|0><0|$ is populated; in this case the siganl is called Ground State Bleaching (GSB). The pathways R_3 and R_6 appear when a three level system is considered; specifically the

second interaction creates a population state $|1><1|$ and the third interaction allow to access to the state $|2>$ from which we have the emission. In this specific case the signal is called Excited State Absorption (ESA).

From time to frequency domain

Let us now understand which signal is detecting when a 2DES experiment is performed and how can be interpreted. The detected signal after the interaction with the third pulse is proportional to the third order non linear polarization:

$$S^{(3)}(t_3,t_2,t_1) \propto iP^{(3)} \propto e^{i(\mp\vec{k_1}\pm\vec{k_2}+k_3)\vec{r}}e^{i(\mp\phi_1\pm\phi_2+\phi_3)}\sum_n iR_n(t_3,t_2,t_1) \tag{1.55}$$

where the electric field of the each pulse is expressed by using the semi-impulsive limit in which the envelope can be assumed as a $\delta(t)$ function and ϕ_i represent the phase term:

$$E(t) \propto \delta(t)(e^{-i\omega t+i\vec{k}\vec{r}+i\phi}+e^{+i\omega t-i\vec{k}\vec{r}-i\phi}) \tag{1.56}$$

The combination of the wavevectors indicate the phase matching condition for the rephasing and non rephasing signals that are associated with a specific n^{th} Feynamn diagrams.In order to fully characterized $S^{(3)}$ in amplitude and phase, this signal is typically interfered with a fourth pulse called Local Oscillator (E_{LO}) that is phase locked delayed with respect the third pulse over t_3 time axis. The intensity S acquired at the detector will be:

$$\begin{aligned} S(t_1,t_2,t_3) &\propto \int_0^\infty |E_{LO}(t_3-t_{LO})+S^{(3)}(t_3,t_2,t_1)|^2 dt_3 \\ &\propto E_{LO}S^{(3)} \propto e^{i(\mp\phi_1\pm\phi_2+\phi_3\phi_{LO})}i\sum_n R_n(t_1,t_2,t_3) \end{aligned} \tag{1.57}$$

The detected signal is proportional to the non linear response $R^{(3)}$ and it contains structural and dynamical information of the system. The interpretation of this signal becomes very difficult when it is analyzed in time domain; for this reason, a double Fourier transform is applied to the signal S with respect the time intervals t_1 and t_3 in which the system is in the coherence states:

$$S(\omega_1,t_2,\omega_3) = \int_0^\infty \int_0^\infty S(t_1,t_2,t_3)e^{i\omega_1 t_1}e^{i\omega_3 t_3}dt_1dt_3$$

where the new coordinates correspond to ω_1 (excitation frequency axis) and ω_3 (detection frequency axis).The coordinate t_2 remains unaltered and it allows to temporally charac-

terized the processes in the system. The final detected signal can be represented with time-resolved excitation/detection two-dimensional spectra that are proportional to the Fourier transform of the sum of the R_n terms. Let us now consider a two level system

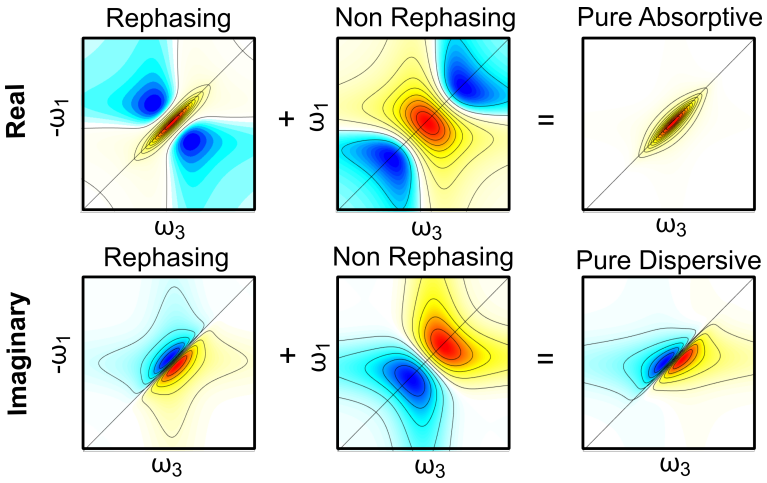

Figure 1.8: Simulated 2D spectra for a two level system at $t_2 = 0$: on the top there are the real part of the rephasing (left), non rephasing (center) and pure absorptive (right) 2D map. In the bottom there are the imaginary part of the rephasing (left), non rephasing (center) and the pure dispersive (right) 2D map

where the separation between the ground $|0>$ and excited $|1>$ states is ω_{01}. At $t_2 = 0$, the Fourier transform of the rephasing and non rephasing terms are:

$$R_1(\omega_1, \omega_3) \propto \frac{1}{i(\omega_1 + \omega_{01}) - 1/T_2} \frac{1}{i(\omega_3 - \omega_0 1) - 1/T_2} \tag{1.58}$$

$$R_4(\omega_1, \omega_3) \propto \frac{1}{i(\omega_1 - \omega_{01}) - 1/T_2} \frac{1}{i(\omega_3 - \omega_0 1) - 1/T_2}$$

The non rephasing 2D spectra (R_4) shows a peak in the position $\omega_1 = \omega_{01}$ and $\omega_3 = \omega_{01}$. In the rephasing signal, the peak appears in the position $\omega_1 = -\omega_{01}$ and $\omega_3 = \omega_{01}$. The different sign of the ω_1 for the position of the maximum point is due to the cohrence state during t_3 is the complex conjugated with respect the one created during t_1; this implies an opposite rotation direction of the Boloch vector during t_1 and t_3 time intervals. Both equations 1.58 are a product of two complex function that can be written as the sum of a real and imaginary part. The imaginary part correspond to the dispersion and the real part correspond to the absorption. Typically the pure absorption spectra are the one used for the data interpretation, but it is impossible to recover just taking the real part of the rephasing and non rephasing signal separately. Let us indicate with X the real part and

with Y the imaginary part, we will get:

$$Re\{[X(\omega_1) + iY(\omega_1)][X(\omega_3) + iY(\omega_3)]\} = X(\omega_1)X(\omega_3) - Y(\omega_1)Y(\omega_3) \tag{1.59}$$

The real part of the signal contains both absorption and dispersion contributions that creates phase twist in the 2D maps. Figure1.8 shows the real and imaginary part of the rephasing and non rephasing signal at t_2=0 in which the dispersion contribution generates the negative features in the 2D map. In order to measure the pure absorptive spectra, is necessary to calculate the real part of the sum of rephasing and non rephasing signals:

$$Re\{R_1(-\omega_1, \omega_3) + R_4(\omega_1, \omega_3)\} = 2X(\omega_1)X(\omega_3) \tag{1.60}$$

An example of this spectrum is reported in figure 1.8 where the phase twist disappear by preserving the sign of the response functions R_n.The same approach can be used to find the pure dispersion spectrum which is obtained by calculating the imaginary part of the rephasing and non rephasing sum. In the next section we show the experimental method to acquired this signal and how to obtained directly the pure absorptive 2D spectra.

1.2. 2DES Experimental Implementation

In the previous section we recover the third order nonlinear response function obtained after the interaction between a system and three electromagnetic fields (adapted for 2DES experiment). The amount of information inside this response allow to make a complete description of the system in terms of structure and mechanism within molecules. The implementation of the 2DES experiment result complicated due to the several constrains that must be satisfied in terms of laser pulses and mechanical stability [29]. In the last two decades different methods were explored to implement 2DES and in this section some of them are mentioned by showing positive and negative aspects and more details will be given for the experimental apparatus adopted in this thesis.

1.2.1. Pulse geometries

The experimental implementation of the 2DES technique is always considered as a challenge due to the several constraints that must be satisfied; specifically it requires an appropriate pulse geometry and a phase stability to perfectly defined the delay between them. In the last twenty-years several methods are used to perform 2DES experiment and typically the pulses configurations adopted are two: Boxcars geometry [30] and pump-probe geometry[31]. Figure 1.9a shows the boxcar geometry in which the three pulses E_1, E_2 and E_3 involved in the experiment propagate along different direction identified by the wavevectors k_1, k_2 and k_3. The non linear response signal emitted from the sample can propagate along different direction which are the linear combination of the wave vector k_i associated to each electromagnetic fields. Thanks to this wavevector mismatch, this geometry allow to separately detect the rephasing and non rephasing signals contributions that propagate along $k_R = k_2 - k_1 + k_3$ and $k_{NR} = k_1 - k_2 + k_3$ as was already mentioned in the previous section. In this scheme a fourth pulse, usually called Local Oscillator (E_{LO}) interferes with the response signal of the system and it allows to fully resolved such a signal in amplitude and phase. This implementation allows the detection of the signal in a background-free direction but at the same time the stabilization in terms of phase and delays between the pulses can be complicated. Figure 1.9b shows the second kind of configuration that is called partially collinear pump-probe geometry in which the first and the second pulse E_1 and E_2 (identified as pump pulses) propagate along the same direction and a third noncollinear pulse E_3 that acts as a probe ($k_1 = k_2 \neq k_3$). This particular condition of the wavevectors imply that the rephasing and non rephasing signals propagate along the same direction which is k_3 (probe wavevector). For this reason the probe pulse has a double nature; one to generate the third order non linear

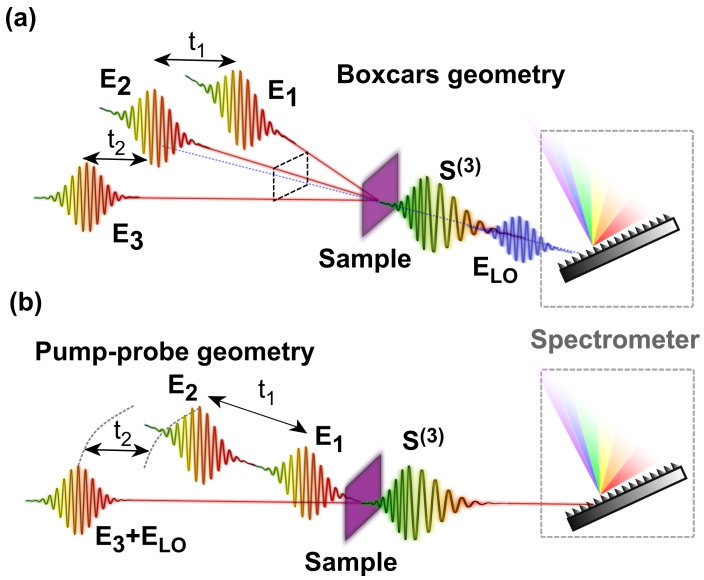

Figure 1.9: 2DES laser pulses configurations: (a)Fully non collinear geometry (Boxcars geometry) in which the pulses E_1, E_2 and E_3 propagate along different direction and the third oredr non linera signal emitted from the sample $S^{(3)}$ interfere with a local oscillator E_{LO}; (b) Partially collinear geometry or pump probe geometry in which the pulses E_1 and E_2 propagate along the same direction and the pulse E_3 behaves also as a local oscillator.

signal $S^{(3)}$ and the second one as local oscillator to heterodyne the signal (self-heterodying configuration). The detected signal contains directly the sum of the repahsing and non rephasing signals that correspond to the pure absorptive spectra [32]. As it was already mentioned at the beginning of this section, a crucial point to perform 2DES experiment is the phase stability between the pulses; in particular in the time intervals t_1 and t_3 where the Fourier transform is applied and the system is in a coherence between the ground the excited state.In time interval t_2 the system is in the population state and in some cases it can shows coherences of different nature as vibrational, vibronic or electronic. Such frequencies are typically much lower with respect the optical frequencies obtained in t_1 and t_3 time intervals and they not required an accurate phase stability as the others. The Fourier transform along the detection time interval t_3 is usually performed by a spectrometer and its phase stability is required between the third pulse and the local oscillator. This constrains is overcome in the partially collinear geometry where a fourth pulse in not required to fully detect the signal. In general, to convert accurately the coherence time delays into optical frequencies, a precision of $\lambda/100$ is required[33]. Following, different strategies are presented to overcome the 2DES experiment constraints and an entire section is dedicated to the method adopted for this thesis. In this work we use a setup in pump-probe geometry that exploits a device called Translating-Wedges-Based Identical

pulses encoding System (TWINS) to fixed the phase stability required between the first and the second pump pulses[34].

Standard Inteferometer: This is the first method adopted for multidimensional Fourier transform spectroscopy experiment to generate time delayed laser pulses[35, 36]. It is composed of a beam splitter to create two replicas of the beams and mirrors to guide the beams. One of the mirror is mounted on the translation stage to control the delay between the pulses. This device required an active stabilization to get high precision time delay measurements. Typically it is used for IR spectral region in which the phase stability is not demanding as for the visible spectral range. The bandwidth is only limited by the optical components of the device (beam splitters and mirrors).

Pulse shaper: A second method adopted to create two phase locked laser pulses is called pulse shaper. It is a device composed by a pair of gratings, a pair of cylindrical lens and an acusto-optics modulator[37]. Briefly, the first grating spatially separate the spectral components of the incoming beam that are then collimated with a cylindrical lens positioned at distance f from the grating. At distance $2f$ from the first lens, there is a second lens that focus all the spectral components to a second grating set at distance f with respect the second cylindrical lens. The acusto-optics modulator is setting in the middle of the two lenses (Fourier plane), in which each spectral component of the pulse is spatially separated (Spatial Fourier Transform). The acustic wave behaves as a grating that allows to modulate in amplitude and phase the pulse. Specifically the output of this device can be easily written in the Fourier domain in the following way:

$$E_{out}(\omega) = E_{in}(\omega)M(\omega) \tag{1.61}$$

where E_{in} and E_{out} are the Fourier transform of the input and output electric fields and $M(\omega)$ is the transfer function of the pulse shaper. Once the output is setting, it is possible to recover the corresponding transfer function. in order to obtain two delayed replicas of the same pulse, the transfer function assume the following expression:

$$M(\omega) = (1 + e^{i\omega t}) \tag{1.62}$$

The two pulses will be delayed by time t and are phase locked because their optical path is the same. In general, based on the choice of $M(\omega)$, it is possible to create an arbitrary electric field. The disadvantages are the high cost for the implementation and the spectral limitation based on spatial-light modulator shaper. In the next section we present the strategy adopted in this thesis in which a birefringent interferometer is exploited to create a phase locked pairs of the pump pulses .

1.2.2. TWINS

The partially collinear configuration adopted in this thesis exploit a device called Translating-Wedges-Based Identical pulses encoding System (TWINS) to generate phase locked pump pulses pair and allows a mechanical control the delay between them. This device exploits the birefingence property of some materials in which a light beam can experience different refractive index based on the wavelength of the beam and its polarization direction. In general, in a birefringent material, we can identify two different refractive index which are called ordinary ($n_0(\lambda)$) and extraordinary index ($n_e(\lambda, \theta)$) where θ represents the propagation direction of the electric field. Another important characteristic of this materials is the presence of a particular axis called optical axis in which the light beam can propagate experiencing an isotropic environment [13]. Figure 1.10 shows the scheme of the device that his based on three building blocks denoted with letters A, B and C composed by the same birefringent material and the gray arrows represent the optical axis direction. The scheme include an xyz reference frame in which the z axis correspond to the propagation direction of the pulse. Before and after the three blocks there is a polarizer which orientation is fixed at 45 degree with respect the x and y axis. The Block A is a birefringent plate with optical axis along the y direction and fixed thickness d_A, the block B is composed by a pair of birefringent wedges with optical axis along the x direction and absolute width d_B and block C is similar to block B but the optical axis is along the z direction. The polarizer P_1 set the orientation of the incoming beam at 45 degree with respect the

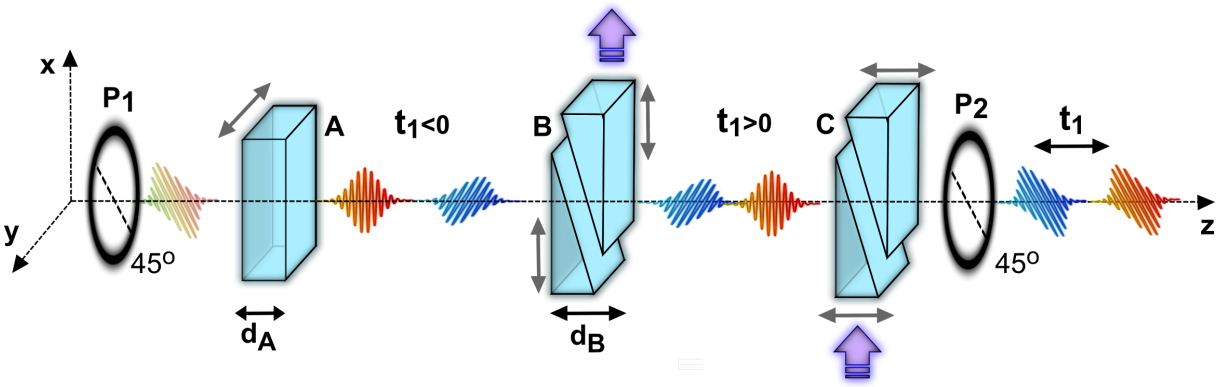

Figure 1.10: TWINS scheme: P_1 and P_2 polarizers at 45^o with respect x, y axis; A α barium borate (α-BBO) plate with optical axis (gray arrow) along y direction and thickness d_a; B (C)α-BBO wedges pair with absolute thickness d_B and optical axis along x (z) direction. Along the z axis there is the temporal evolution of the pulse replicas and violet arrows indicate the movement of the wedges

x and y axis. When the pulse propagate in block A, the ordinary (y-component) and

extraordinary (x-component) polarizations experienced different refractive index (n_o and n_e) and they cross the plate with different group velocities (v_{go} and v_{ge}). After Block A, the two components of the pulse accumulate a delay that is proportional to d_A. The different position of the optical axis in block B induces a relative delay with opposite sign with respect the Block A. The relative delay between the pulse replicas after block B is $t_1 = (d_A - d_B)(1/v_{ge} - 1/v_{go})$. The Block C does not introduce an extra delay between the replicas because they experience the same optical path (optical axis along the z direction). The polaraizer P_2 after Block C projects both replicas at 45 degree with respect the x and y axis. The variation of the delay t_1 is possible by varying the thickness of block B; Specifically one of the two wedges is mounted on a micrometer translation stage and when the thickness changes by Δd_B, it produces a time variation of $\Delta t_1 = \Delta d_B(1/v_{ge} - 1/v_{go})$ that allows to control delay t_1 with very high accuracy. We can estimate this precision by considering α-barium borate (α-BBO) as birefringent material (n_o=1.67 and n_e=1.53 at $\lambda = 600nm$), thickness of block A $d_A = 2mm$ and wedges angle of 7 degree mounted on a translation stage of $0.1\mu m$ precision. This allows to control t_1 down to ~ 5 as that correspond to an accuracy larger than $\lambda/300$ which is much larger with respect to the required one. Furthermore the two replicas are phase locked with very high stability and reproducible because they follows the same optical path. From the experimental point of view, the combination of block A and B is not sufficient to perform 2DES experiment because we are not able to control the delay t_2. This problem is overcome by inserting the block C in which one of the two wedge is mount on the same translation stage of the wedge in block B, in such a way, one of the two replicas experiences the same optical path when the relative delay t_1 changed. In particular, only the first pulse change the time position while the second pulse is fixed. The Block C allows also to compensate part of the group delay dispersion introduced by block B that make this device powerful also for broadband laser pulses. Important to note that the two pulse replicas, while they crossing the wedges, acquire a delay dependent phase difference given by:

$$\Delta\phi = \frac{\omega_0[(1/v_{g0} - 1/v_p) - (1/v_{ge} - 1/v_p)]\Delta t_1}{(1/v_{ge} - 1/v_{go})} \tag{1.63}$$

where ω_0 is the carrier frequency and v_p is the phase velocity. This phase difference affect the 2DES measurement and,for this reason, a pahsing compensation must be implemented.

1.2.3. 2DES apparatus

In this section we present the experimental setup adopted to perform 2DES experiment by explaining the role of the different devices. Figure1.11 shows a simplified scheme of

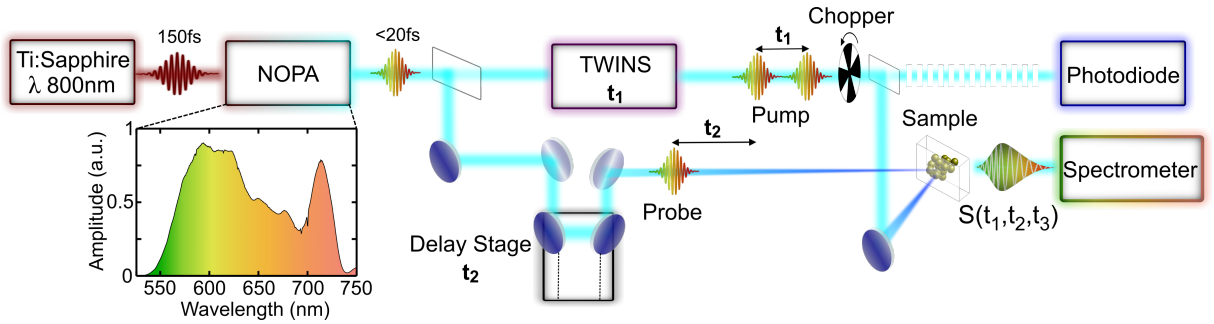

Figure 1.11: 2DES setup sketch: Ti:Sapphire laser pump a non collinear optical parametric amplifier (NOPA) to generate temporally compressed pump and probe pulses which spectra is showing in the bottom of the NOPA box. After the pulse compression, a beam splitter separate the pump and the probe optical paths. The reflected one is the probe beam that passing through a delay stage to control the delay between the second pump pulse. The transmitted one is the pump beam in which the TWINS is used to create a replica of the pump pulse and control delay between them. These pulse are modulated with a chopper and than part of the beam is focus to the sample and the other part id detected by a photodiode.

the apparatus in which the main building blocks are represented with colored squares. The setup uses a Ti:Sapphire laser in mode locking regime that emits 150 fs laser pulses centered at λ=800nm with 1kHz repetition rate. Such a pulse is used to pump a non collinear parametric amplifier (NOPA) to generate visible laser pulses with a spectrum spanning from 550nm to 750nm as is reported in the figure below the NOPA block [38]. This pulse are then temporally compressed with a pair of chirped mirrors in which the beam computes 7 bounces to reach a temporal resolution of <20 fs [14]. The pump and the probe laser pulses for the 2DES experiment are separated by a beam splitter setting after the NOPA. The reflected one correspond to the probe beam that goes into a motorized translation stage to control the delay t_2. The transmitted beam correspond to the pump and after crossing the TWINS, it will split in two replicas delayed by t_1. The temporal dispersion introduced by the birefringent materials is compensate by 9 bounces on a pair of chirped mirrors in order to obtain similar time duration as the probe. At this point, part of the pump beam is then send to the sample and the second part is detected by a photodiode. The non linear signal S emitted from the sample propagates along the probe direction and it is detected by a spectrometer that directly compute the Fourier transform along the detection time axis t_3 (detection frequency axis). The electrical devices in the setup are synchronize in order to measure the difference between the signals with an without the pre-excitation of the pump pulses. For this reason, along the pump optical path, there is an optical modulator (chopper) that which frequency is half of the repetition rate (500Hz) of the Ti: Sapphire laser. Before starting a measurement, two important steps

must be performed: the first one is the calibration of the TWINS in order to reconstruct the excitation frequency axis and the second one is the temporal characterization of the laser pulse.

1.2.4. Calibration and phase compensation

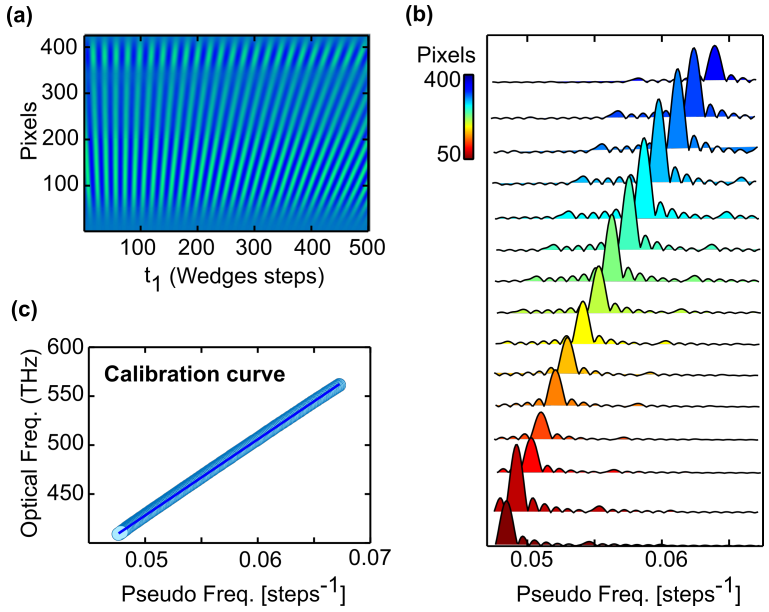

Figure 1.12: (a) pixels time resolved autocorrelation of the pump pulses detected at the spectrometer by scanning delay t_1; (b) Frequency traces obtained by Fourier transforming horizontal cuts of (a); (c) calibration curve in which each maximum point of the traces in (b) is associated with the related optical frequency. The blue line represent the linear function that best approximate the data

The calibration procedure involved only the pump beam; in particular one portion is send to the spectrometer and the other to the photodiode. Once the pump beam is setting, we mechanically scan the delay t_1 from -30fs to 250fs with 500 points usually labeled as motor steps. Figure1.12a shows the signal detected at the spectrometer which is a 2D map that represent the signal for different spectral components (pixels) as a function of t_1 motor steps. This map correspond to the linear autocorrelation of the two pump pulses. At this point, we apply the Fourier transform along every horizontal line of the 2D map (dynamics detected at each pixels) by calling the new axis of the Fourier domain Pseudo Frequency axis. Figure1.12b shows the pseudo frequencies traces of the pixels from 50 to 400 in which the maximum peak of each traces depends on the pixel position. Figure1.12c shows the association between the optical frequencies determined by the pixels and the pseudo frequency obtained at the maximum intensity of

the traces in figure 1.12b. The experimental point are then fit with a first order polynomial function in order to find an analytical relation between the two frequencies. Once the

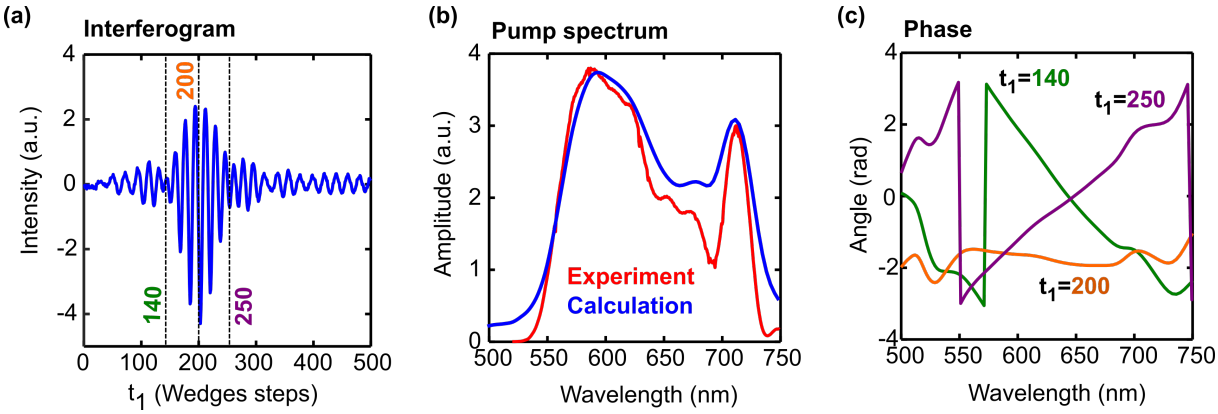

Figure 1.13: (a) interferogram of the pump pulses detected at the photodiode by scanning delay t_1; (b) Amplitude spectra of the inteferogram (blue curve) overlapped with the experimental spectra of the pump pulse (red curve); (c) phase spectrum obtained by cutting the interferogram in figure (a) at t_1 equal to 140 (green curve), 200 (orange curve) and 250 (violet curve)

calibration is completed, the second step consist of compensate the phase introduced by the TWINS; in particular we exploit the information of the autocorrelation detected by the photodiode [39]. Figure1.13a shows the interferogram of the pump pulses measured from the photodiode by scanning delay t_1. In order to find the value of the phase that compensate the 2DES spectra, it is necessary to identify the motor position in which the pump pulses temporally overlap (zero position) and cut the signal before that time to respect the causality principle. We now choose different t_1 motor step zero position and we compare how the Fourier transform of the interferogram change. The correct zero position is when the phase of the Fourier transform does not show a strong dependence with respect the optical frequencies, that in our case we usually express in terms of wavelength. The amplitude of the Fourier transform is not useful for this goal due to their independence with respect the choice of the zero position. Figure1.13b shows the amplitude spectra (Blue curve) that shows a good agreement with the experimental spectra of the pump pulse (red curve) as it was expected from Parseval theorem [13]. Figure1.13 shows the phase spectra by considering as zero motor steps position the points: 140 (green curve), 200 (orange curve) and 250 (violet curve).This analysis shows that if the zero motor step position is took close to the maximum intensity of the interferogram (t_1=200) the two pump pulses are almost temporally overlapped and the respective phase is more flat with respect the phase spectra obtained before (t_1=140 phase decrease with the wavelength) and after (t_1=250 phase increase with the wavelength) the maximum. The phase spectra calculating for zero position t_1=200 will be used to correct the 2DES spectra during the

experiment. However, this procedure perfectly compensate the phase if the pulses are considered as delta Dirac functions. In other cases,when the pulse have a fixed temporal width, the overlap between the pulses is extended for a larger time and taking the zero position at the maximum of the interferogram can produce a phase flip in the 2DES spectra. In the appendix A some simulation of this effect are reported and the best solution will be choose a point that is slightly before the maximum.

1.2.5. Temporal characterization of the pulses

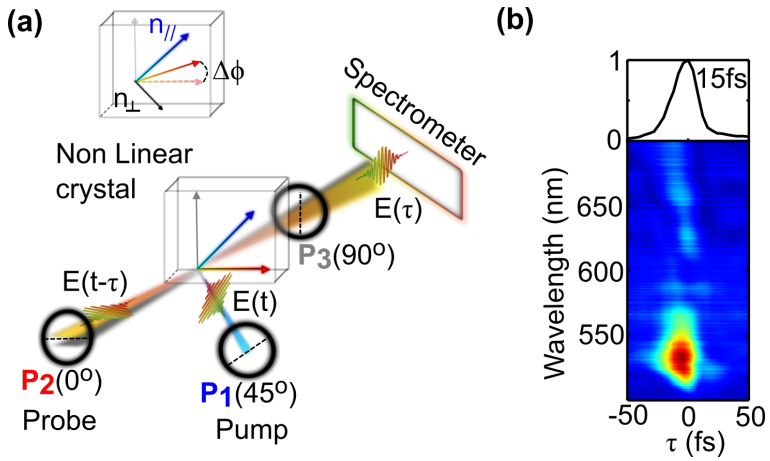

Figure 1.14: (a)PG-FROG scheme: P_1 and P_2 are the polarizer along the pump and probe pulse setting at 45^o and 0^o with respect the horizontal line, P_3 analyzer setting perpendicularly with repsct the orientation of the probe; on top left there is a reprsentation of the non linear crystals with the direction of the refractive index $n_{//}$ and $n_{\perp}$ indiced by the pump pulse and the rotation $\Delta\phi$ experienced by the probe pulse; (b) PG-FROG signal at different wavelength and on top there is the integrated map along the wavelength axis from which it is possible to estimate 15fs time duration from the full width at half maximum of the Gaussian lineshape

In order to characterize the pulse compression at the sample position, we implemented a Polarization Gating Frequency-Resolved Optical Gating (PG-FROG) measurement to obtain the correlation between pump and probe laser pulses. PG-FROG technique exploits third order non linear optical effects in a non linear crystals in which the refractive index of the material depends on the intensity of the beam [13]; in particular the expression of the modified refractive index is:

$$n = n_0 + n_2|E|^2 \tag{1.64}$$

where n_0 is the refractive index without interaction with the light, n_2 is a coefficient which is proportional to the third order non linear susceptibility (χ^3) and $|E|^2$ is the intensity of the field. This technique is based on the interaction of two delayed laser pulses with a

non linear crystal in order to exploit their polarization orientation to acquire information about their temporal width. In our case these two pulses are the pump and probe used for the 2DES experiment, and the material used to generate the third order non linear effect is a few silica plate with the same path length of the sample; this ensures that the pulses propagate in the same amount of material as in the experiment. Figure1.14a shows the scheme of the PG-FROG in which the polarization of the pump and probe pulses are setting with two polarizers labeled as P_1 and P_2. The orientation angle between them is setting at 45^o and a third polarizer (P_3), usually called analizer, is fixed between the crystal and the spectrometer with an orientation perpendicular with respect the probe pulse. The propagation of the intense pump beam through the material induces a transient refractive index change along the polarization direction of the pump. In particular, the crystal assumes different refractive index along the parallel ($n_{//}$) and perpendicular ($n_{\perp}$) direction of the pump orientation:

$$n_{//} = n_0 + n_{//}|E|^2 \tag{1.65}$$

$$n_{\perp} = n_0 + n_{\perp}|E|^2 \tag{1.66}$$

where, in our case, we consider $n_{2//} > n_{2\perp}$ The probe pulse, delayed by a time τ, will experience the variation of the refractive index only when it is temporally overlapped with the pump pulse on the crystal. In that specific case, the birefringence induced by the pump pulse, will rotate the polarization of the probe by an angle [13]:

$$\Delta\phi = \frac{2\pi}{\lambda} L(n_{2//} - n_{2\perp})|E|^2 \tag{1.67}$$

where λ is the carrier wavelength of the probe pulse and L is the width of the material. In order to measure this effect, the analyzer P_3 along the probe direction, allow the crossing of the probe only when its polarization is rotated. By collecting the signal at the spectrometer as a function of the delay τ, we can obtain 2D map as a function of wavelength and time τ. By integrating this 2D-map along the wavelength axis, we usually obtained a Gaussian profile from which it is possible to estimate the time duration of the probe pulse. Figure1.14b shows the 2D map obtained with $200\mu m$ few silica and on top there is the integrated spectra from which it is possible to estimate, by fitting with a Gaussian function, a Full width at half maximum of 15fs. In order to perform this measurement in the 2DES setup, is necessary to setting delay t_1=0 to have just one pump pulse; the delay τ corresponds to the waiting time t_2 and measuring the signals as a difference between the transmission with and without pre-excitation of the pump

pulse. Important to notice that the choice of the material used in the PG-FROG must be consistent with the sample that we are going to measure. The samples that are used in this thesis are both in solid states or in solution. In case of solid state, is useful to use the same material of the substrate with the same thickness. In case of solution, is useful to use the solvent inserted in the same cuvette to preserve path length.

1.2.6. 2DES data acquisition

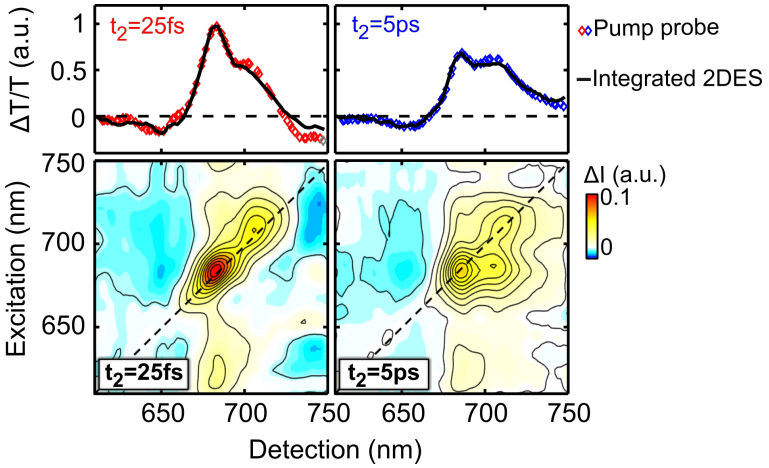

Figure 1.15: Pure absorptive spectra of Spirulina plantesis monomer at t_2=25fs and 5ps. On top there is the comparison between the spectra obtained by integrating 2D map along the excitation axis (black continuum lines) and the pump probe spectra (red and blue symbols) performed by fixing t_1=0

Once the calibration and phase correction parameters are setting, it is possible to start a pump probe measurement in which the delay t_1 is fixed to zero and only delay t_2 is scanned. In this case, instead to generate a 2D map for every delay, we measure 1D spectra which correspond to the 2D spectra when they are integrated along the excitation axis. This pump probe measurement is usually acquired for two reasons: (i) it represent a good method to check the validity of the 2DES experiment by comparing 1D spectra with the integrated 2D map; (ii) Performing pump probe measurement with high temporal resolution (<20fs). After the acquisition of the pump probe data, the 2D maps are obtained by fixing delay t_2 and by scanning delay t_1 from -30fs to 250fs. The detector spatially separate each spectral component of the signal by obtaining for every detection wavelength, a signal as a function of t_1. By applying the Fourier transform of the signals as a function of t_1, we generate a 2D spectrum at a fixed delay t_2. Figure 1.15 shows two 2D maps at t_2=25fs and 5ps obtained for Spirulina plantesis monomer and above there is a comparison between the pump probe spectra (symbols) and the integrated 2D

map (black line) at the same t_2 delays. The two spectra have a good agreement which demonstrate the validity of the 2D maps. Is important to notice that some peaks in the 2D map that stay out of the diagonal (cross peaks) are completely hide in the pump probe spectra and this confirm the ability of the technique to combine high spectral and temporal resolution. In the next chapter we explore the different information that are possible to retrieve from this experiment, by considering three single molecules as case of study.

2 | Information revealed by 2DES

In this chapter we investigate different kind of information that are possible to detect with 2DES technique; in particular, we will show different 2DES analysis approaches applied on three different simple molecules. The first one is the Perylene Bisimide (PBI), an organic dye which is used typically for synthesizing light harvesting systems[10]. The second one is the free base porphyrin which is usually adopted in order to mimic the role of chlorophylls in natural photosystems [40]. The last one is the Lumogen-F Orange (LFO), an organic dye with a strong oscillator strength suited for the study dephasing time and spectral diffusion. The details about the experiment and the sample are reported in the appendix A

2.1. 2DES Signals in Perylene Bisimide

In this section we explore the different kind of signals that can be measure with 2DES technique. As it was already mentioned in the previous chapter, the possibility to directly detect the pure absorptive 2D spectrum allows to capture the following signals: Ground State Bleaching (GSB) dynamics (transition from the ground to the excited state), Stimulated Emission (SE) which is the transition from the photoexcited state to the ground state and Excited State Absorption (ESA) that represent the absorption from the photoexcited state to higher energy levels. These signals are completely overlapped in a 2D spectrum and it results very complicated to discriminate the different processes that are taking place. In order to distinguish the different signals, it is possible to explore the theory explained in the previous chapter to reproduce 2D spectrum generated from each signals. If the calculations well reproduce the experimental data, we are able to give a direct interpretation of the mechanisms inside the system. Here, we consider as a case of study Perylene Bisimide (PBI) which is a simple dye molecule that shows a long-lived electronic bright state in the visible spectral range and a small amount of characteristics excite state absorption[41, 42]. These spectral features make this molecule a good candidate to compare simulation and experiment. Figure 2.1a shows the steady state absorption spectrum of the PBI monomer dissolved in the acetonitrile (Black line)

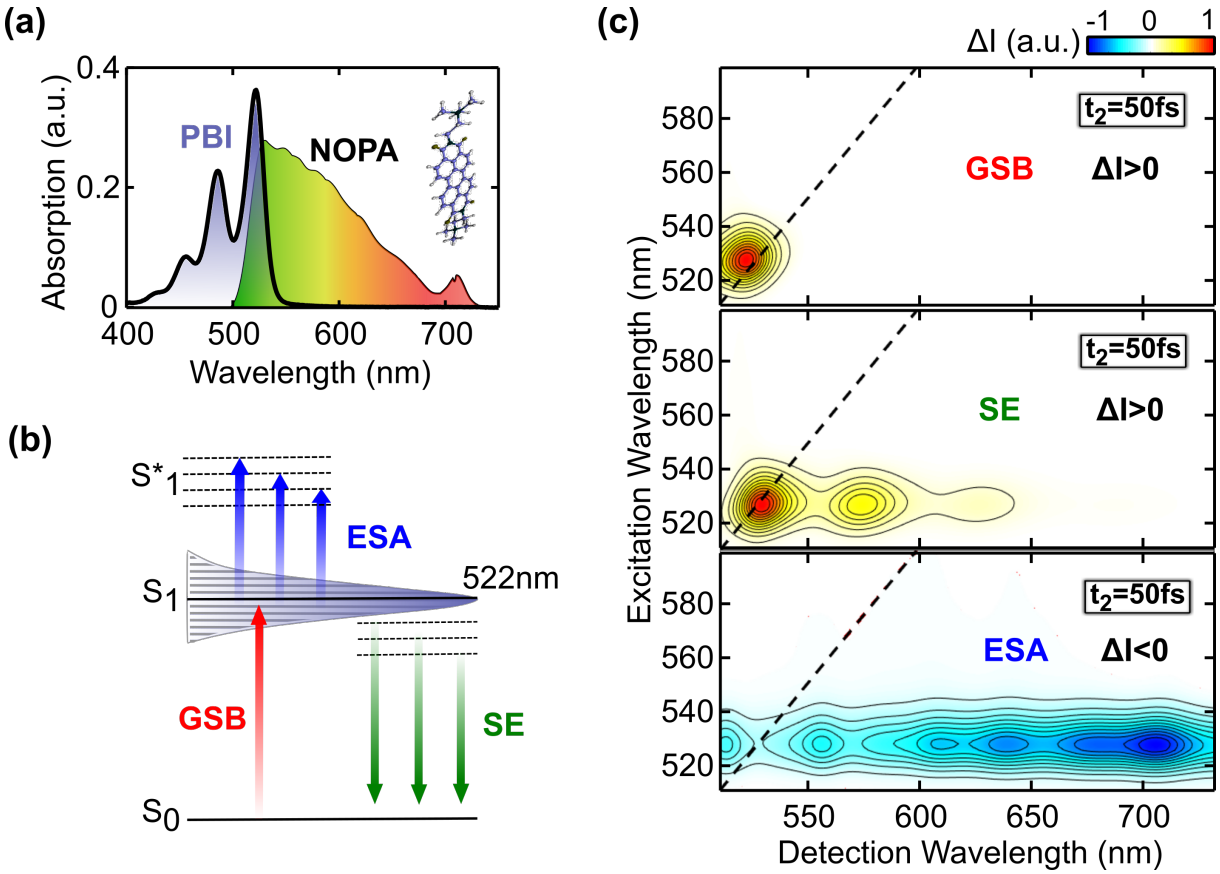

Figure 2.1: (a) steady state absorption spectrum of the Perylene Bisimide diluted in acetonitrile (black line) with the molecular structure (top right) and laser pulse spectrum (rainbow area); (b) Energy level scheme of the molecule in which GSB (red arrow), SE (green arrows) and ESA (blue arrows) signals transitions are emphasized; (c) Simulated 2D maps at t_2=50fs for the GSB (top), SE (middle) and ESA (bottom) signals.

overlapped with the pulse spectrum adopted for the experiment (rainbow area) with the PBI molecular structure. The static absorption clearly shows a main transition at 522nm (covered by the laser pulse) and vibration replicas at higher energies. The electronic structure was predicted with two different methods: the Restricted Active Self-Consistent Filed (RASSCF) [43] and the Time Dependent Density functional Theory (TDDFT)[44]. In this work we only report the results obtained with the more sophisticated method (RASSCF) that this typically adopted to simulate non linear spectroscopy experiments even if spectral features regarding this molecule are well predicted with both methods [45]. The calculations predict the excited state S_1 by considering the B_{3u} symmetry class and two bright transition from S_1 to higher states which generate ESA signals. Furthermore, a dark state was predicted in which the system can relax from the S_1 state by emitting an SE signal. Figure 2.1b shows the energy level scheme in which S_0 is the ground state, S_1

is the excited state and S_1^* represent the higher energy levels. By considering this model, it was possible to implement the theoretical description of the molecule under multi-pulse interaction. In particular, the theoretical framework that we used, explored perturbation theory combined with two more approximation: (i) The Condon approximation in which the dipole moment does not depend on the nuclear coordinate; (ii) The energy states are long-lived with respect the temporal resolution of the experiment [46, 47]. The long-lived signal for the S_1 excited state (complete decay in nanoseconds time scale) and the rigidity of the molecule, demonstrate the validity of these two approximation [45]. Figure 2.1 shows the calculated 2D spectra obtained for GSB (on top), SE (middle) and ESA (bottom) signals at t_2=50fs by using the RASSCF method. Such spectra show a signal only when the S_1 state is excited but the detected signal is spread along the entire spectral window. The GSB signal is mostly located along the diagonal line and it represent the transition $S_0 \rightarrow S_1$ in the double sided Feynman diagrams in the t_3 time interval. The SE signal appears as cross peaks detected at lower energy with respect the S_1 state and it is due to possible transitions from lower vibrational levels of the S_1 state to the ground state (S_0). The ESA signal has a negative amplitude and it represent the transitions $S_1 \rightarrow S_1^*$. The simulated pure absorptive 2D spectrum at t_2=50fs is obtained by summing these three contributions. Figure 2.2 shows a comparison between the experimental results and

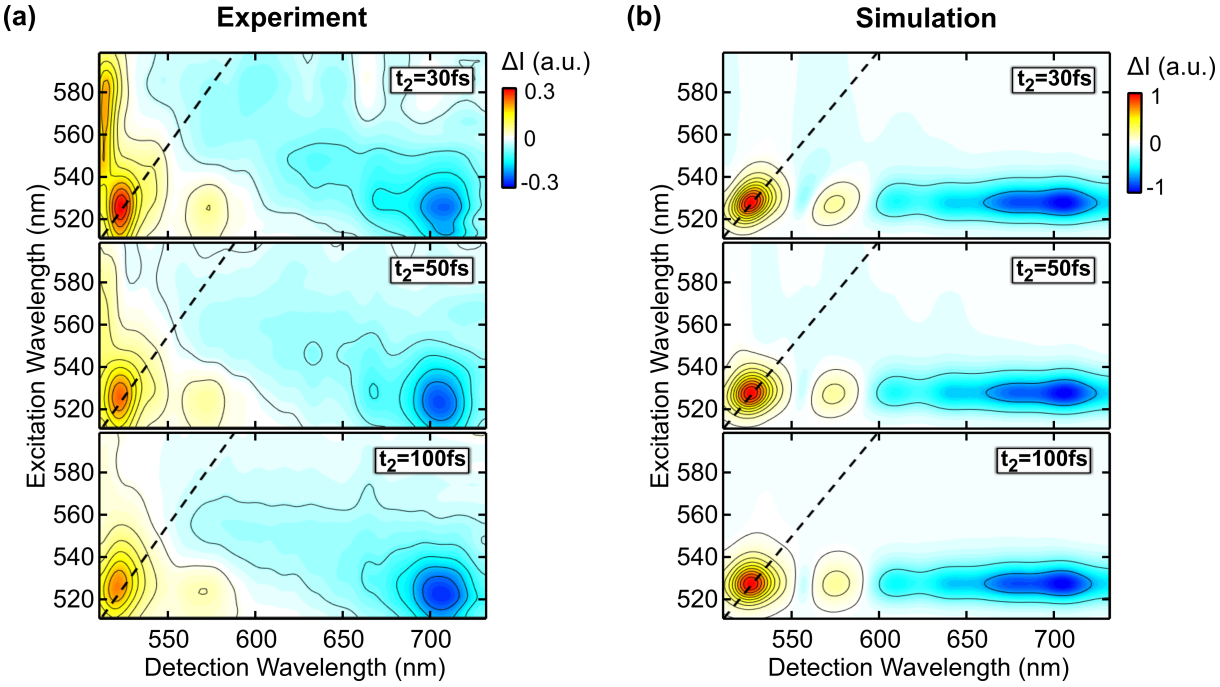

Figure 2.2: Comparison of experimental (a) and simulated (b) pure absorptive 2D spectra of PBI at t_2=30fs, 50fs and 100fs

the simulated 2D spectra at waiting times 30fs, 50fs and 100fs. The calculations are in a

good agreement with the experimental data; in particular, three peaks detected at 522nm, 575nm and 700nm are well reproduced. By combining the information acquired from the simulation of the single signals, we can attribute to the diagonal peak two different contribution: one is GSB signal and the other is the first vibronic SE signal. Such a peak shows also temporal variation of the lineshape (from elliptical at 30fs to circular at 100fs) that is also reproduced by the simulation. This lineshape temporal evolution is due to the spectral diffusion. The cross peak detected at 575nm is a combination of a strong SE Signal and a weak ESA signal. The strongest contribution of the ESA signal manifests around 700nm and it represents the transition $S_1 \rightarrow S_7$. Such a peak is well defined in the experimental data, but the entire ESA band seems not well reproducible from the theory. This discrepancy can be due to the wrong estimation of the equilibration energy found for the state S_7 that could be the responsible of a broad ESA band from 600nm to 750nm. In summary, the advanced theoretical model allows to interpret and, in some case, predict experimental data also for complicated ultrafast spectroscopy technique as 2DES.

2.2. Ultrafast processes in Free base Porphyrin

In the previous section we demonstrate the origin of the GSB, SE and ESA signals and how they are reported in the 2D spectra. In this section we show how excited state energy transfer (EET) and vibrational coherences can be reveal from 2DES technique; specifically we show the case of the free base porphyrin which posses a more complex energy structure with respect the PBI molecule. Figure 2.3a shows the steady state absorption of the molecule overlapped with the laser pulse spectrum that cover a spectral range from 500nm to 700nm and, on the top right, there is the molecular structure. In this case, we are excited simultaneously three absorption peaks labeled as Q_{y0} (peaked at 540nm), Q_{x1} (peaked at 580nm) and Q_{x0} (peaked at 640nm). By exploiting 2DES technique, it is possible to spectrally and temporally characterize internal conversion process from the Q_y band to the Q_x band by studying the temporal evolution of the cross peaks. Figure 2.3 shows 2D maps acquired at t_2=10fs and 500fs where the excitation and detection axis are grid based on the spectral position of the absorption peaks. At t_2=10fs, the 2D map shows three diagonal peaks that reflect the static absorption spectra of the molecule (GSB signals of Q_{y0},Q_{x1} and Q_{x0}). The presence of positive cross peaks below and above the diagonal line indicates possible couplings between the energy states. The ESA signal is spread along the entire 2D map by generating a negative signal that overlapped with the GSB and SE signals. At t_2=500fs, there is a clear formation of a cross peak by exciting at 540nm (Q_{y0}) and detecting at 640nm (Q_{x0}). Figure 2.3 shows

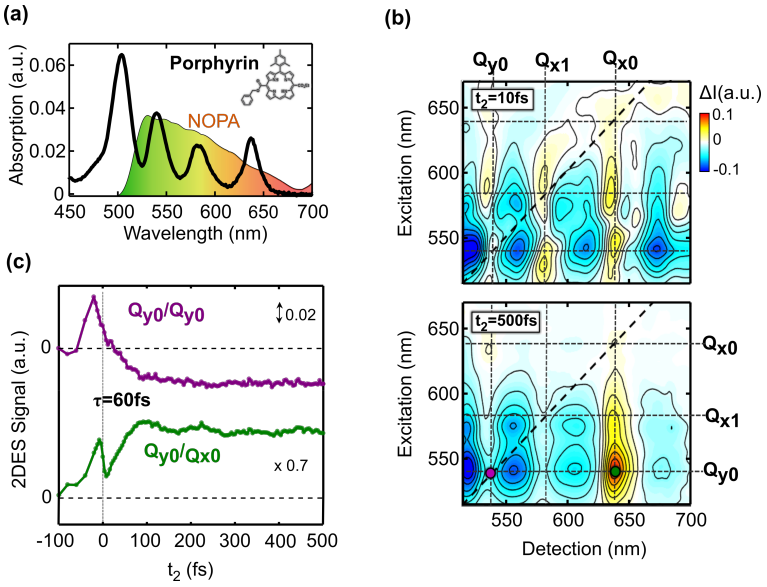

Figure 2.3: (a) Steady state absorption spectrum of free base Porphyrin (black line) with the molecular structure (top right) and laser pulse spectrum (rainbow area); (b) Experimental pure absorptive 2D spectra at t_2=10fs and 500fs, that are grid based on the spectral position of the Q_{y0}(540nm), Q_{x1} (580nm) and Q_{x0} (640nm) bands; (c) t_2 traces of the diagonal peak (violet line) at 540nm/540nm excitation/detection point and cross peak at 540nm/640nm point indicated in the 2D map in the panel (b). The time τ=60fs represent the first decay/formation of the diagonal/cross peak respectively.

the t_2 traces of the diagonal point peaked at 540nm (violet) and the cross peak detected at 640nm (green). The diagonal peak shows a decay that is followed by a formation of the cross peak in a time estimated around 60fs. These dynamics clearly identify an energy transfer from the Q_{y0} to the Q_{x0} that take place in a time scale that is impossible to acquired with a simple pump probe experiment where the typical temporal resolution is around 100fs. In order to obtain a model to explain the data, we performed a simulation by considering the energy level scheme reported in figure 2.4a. In this scheme, the Q_{x1} band is obtained by assuming a coupling between Q_{y0} and Q_{x0} states, and the ESA signal is obtained by adding higher energy levels that are reachable via photon-absorption from both bands. By fixing to 60fs the time in which the internal conversion take place, we are able to simulate 2D maps. Figure 2.4b shows the simulated 2D spectra at t_2=10fs and 500fs where the main spectral features are in good agreement with the experimental data. In particular, the EET process seems well reproduced by looking the formation of the cross peak and decay of the diagonal peak in the 2D map at 500fs. The main discrepancy between the experiment and the simulation comes from the ESA signal which is particularly strong in the simulation for the excitation of Q_{x0} band. This effect can be

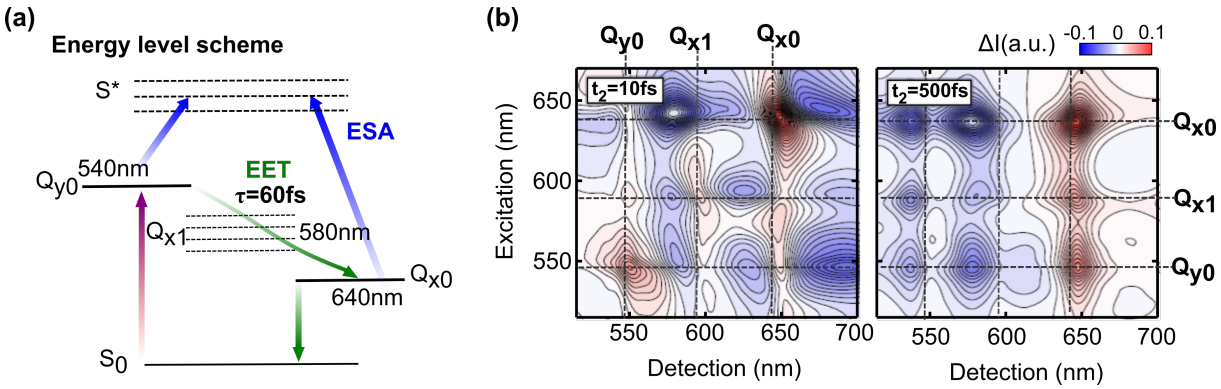

Figure 2.4: (a) Energy level scheme where the violet and the green arrows represent the EET process from Q_{y0} to Q_{x0} bands with the estimated time. (b) Simulated 2D pure absorptive spectra at t_2=10fs and 500fs that are grid based on the spectral position of the Q_{y0}(540nm), Q_{x1} (580nm) and Q_{x0} (640nm) bands.

due to an overestimation of the energy equlibration in the higher energy levels or of the dipole moment responsible of the transition from the Q_{x0} to higher energy levels. Another possible analysis that allows to give more information about the ultrafast processes in the molecule is the study of possible vibrational coherence that can drive internal conversion processes. In the following paragraph we will explain this analysis and we will apply such method to the porphyrin 2DES data.

2.2.1. 2DES Oscillatory map

In the previous chapter we point out that, in a 2DES experiment, the interaction with the second laser pulse generate a population state that evolves during time t_2. This is true for a simple system; however, when the system shows several energy levels that interact to each other, the second pulse can produce a coherence state that evolves in time as an oscillatory signal. Free base porphyrin represent one of these exception where, by constructing the Feynman diagrams, coherences between the different bands can be created during the waiting time interval. In this case we are interested on two high frequency modes at 1350cm^{-1} and 1510cm^{-1} that are created between the Q_{y0} and Q_{x0} bands. In order to study these modes, a method called oscillatory analysis can be implemented. This procedure consist of calculating the Fourier transform of the signal along the t_2 axis, generating a new frequency axis labeled as ν_2[48, 49]. In this way, we are able to create a series of 2D oscillatory maps as a function of the excitation and detection wavelength.In particular, by fixing a value of ν_2, the corresponding 2D spectrum will map out the couple of the excitation and detection frequencies in which the specific mode ν_2 appear. Figure 2.5a shows the 2D oscillatory map at ν_2=1350cm^{-1} and 1510cm^{-1}, calculated in the

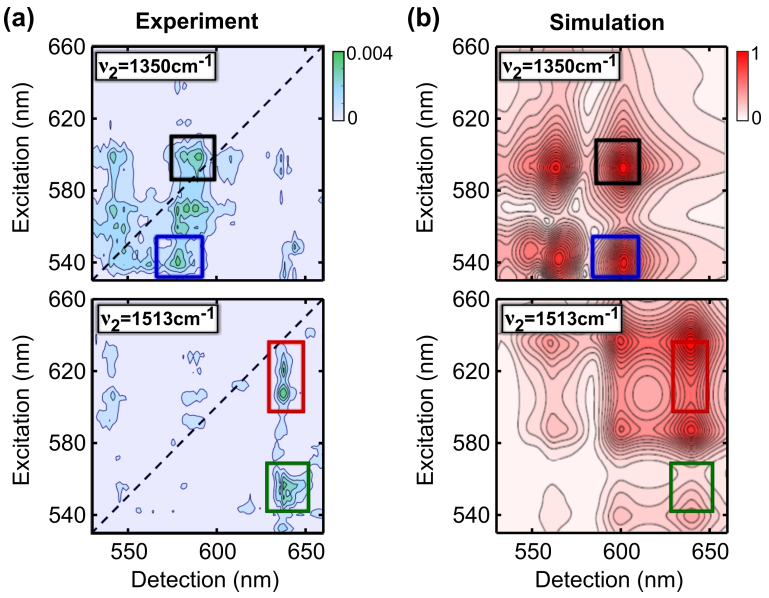

Figure 2.5: Comparison of the experimental (a) and simulated (b) 2D oscillatory maps at ν_2=1350cm^{-1} and 1513cm^{-1} where the main peaks in the experimental data are emphasized with colored square.

following way:

$$S(\lambda_{exc}, \nu_2, \lambda_{det}) = |FT(S(\lambda_{exc}, t_2, \lambda_{det}))|^2 \tag{2.1}$$

The 2D map at ν_2=1350cm^{-1} shows diagonal and cross peaks that corresponding to the position of the Q_{y0} and Q_{x1} bands that are also predicted by the simulation reported in figure 2.5b (on top). The diagonal and cross peak detected at the Q_{x1} band are emphasized with colored squared in both maps. The good agreement between the experimental data and the simulated one confirm the high quality of the calculation and allow to introduce more information in the model of the system. The 2D map at 1510cm^{-1}, even if the agreement with the simulation is lower with respect the other mode, reveals a dominant feature at Q_{x0} detection frequency. The red and the green square in the experimental map emphasized the two more intense peaks that appear in the simulation data as an average within adjacent peaks. This mode seems to couple all three peaks and could be the responsible of the internal conversion observed in the 2D data. The reason of this mismatch between the experimental and the simulated 2D map at ν_2=1510cm^{-1} could be due to the temporal resolution of the experiment (around 15fs) that makes this mode close to the edge of our frequency resolution.

2.3. Lineshape analysis in Lumogen F-Orange

Lineshape analysis is particularly useful in 2DES data because it allows to retrieve information regarding the dephasing time of the molecule, usually label as T_2, and the spectral diffusion effect. In this section we show both studies applied to the Lumogen F-Orange dye (LFO) that is typically used for designing innovative optoelectronic devices based on organic materials. Figure 2.6a shows the steady state absorption (black line) of the

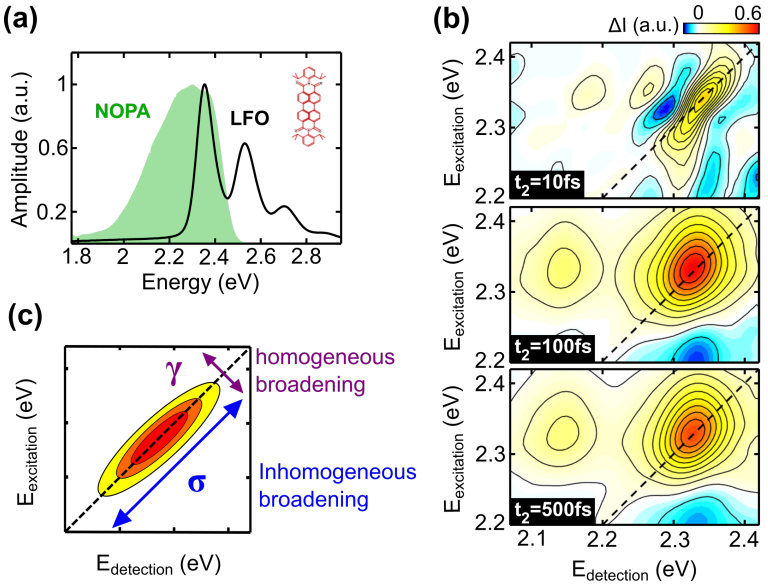

Figure 2.6: (a) steady state absorption of the Lumogen F-Orange (LFO) (black line) with molecular structure (top right) and laser pulse spectrum (green area); (b) Pure absorptive 2D spectra at t_2=10fs, 100fs and 500fs; (c) Representation of one diagonal peak in the 2D map at t_2 close to zero where the inhomogeneous linewidth (σ) and the homogeneous linewidth (γ) are indicated with blue and violet arrows respectively.

molecule accompanied with the molecular structure and the laser pulse spectra (green area). The absorption shows a main transition at 2.35eV and higher vibronic replicas (similar to the PBI absorption spectrum). The laser pulse adopted for the experiment well covers the main transition and it spans from 1.8eV to 2.5eV. Figure 2.6b shows the 2D maps obtained from the experiment at t_2 =10fs, 100fs and 500fs where it is possible to distinguish GSB signal located along the diagonal line and SE signal as a cross peak detected at 2.15eV. From the lineshape point of view, we can notice a variation of the diagonal peak; specifically, at t_2=10fs the it shows an elliptical lineshape elongated along the diagonal line and, for larger delays, it changes by assuming a circular shape. This effect is called spectral diffusion and it will be quantify later in this section. Let us now focus on the lineshape when the delay t_2 is closed to zero where the peak manifest an

elliptical lineshape. Figure 2.6c shows a simple cartoon of a 2D map in this situation where it is possible to identify two different spectral broadening. The one obtained by cutting the peak along the diagonal line (blue arrow) correspond to the inhomogeneous broadening and it reflects the static absorption spectrum where σ is the linewidth of the peak. The linewidth obtained by cutting the peak along the anti-diagonal line correspond to the homogeneous broadening (violet arrow) and it is labeled as 2γ[26]. Such a broadening is directly connected to the dephasing time, but its estimation present some difficulties [50]. In particular, the discrimination between the two different broadening is possible only when the 2D map at t_2=0 is well known. Usually this is not possible due to the finite temporal resolution of the experiment; for this reason, several sophisticated method are implemented in order to get the best estimation of the parameter γ. In the next paragraphs we show a new method in order to estimate homogeneous broadening and how to describe quantitatively the spectral diffusion by using central line slope (CLS) method.

2.3.1. Dephasing time

The time in which a system looses coherence and it relaxes to a population state, is called dephasing time. As it was already mentioned before, it is correlated to the parameter γ and the relation between them is $T_2 = 1/\gamma$ where γ is defined as dephasing rate. There are several method that allow a good estimation of the depahsing rate starting from the experimental data. The simplest one is called Homogeneous limit and it assumes that the elliptical lineshape well separate the homogeneous and inhomogeneous broadening contribution; one alone the anti-diagonal and the other along the diagonal line. In this case the anti-diagonal line can be reproduce with a Lorentzian curve and the diagonal with a Gaussian function[51]. The Full width at half maximum (FWHM) of the best fit will give directly the values of γ and σ respectively. Another method adopted by Siemens and coworkers considers that both homogeneous and inhomogeneous contribution are mixed along both direction and they found an expression of the lineshape that depends on both linewidth parameters [52, 53].This method was applied only for the rephasing 2D signal and it required a complicated theoretical background in order to find the best function that fit with the experimental lineshape. In this paragraph we present a new method in which theoretical framework of 2DES for a two level system is exploited in order to find a good lineshape function. We focus our attention only to the diagonal peak at 2.35 eV where the LFO can be assumed as a two-level system. By using the Bloch equation for a two-level system as reported by Mukamel[28], and applying the rotating wave approximation, it is possible to obtain a simple expression of the pure absorptive

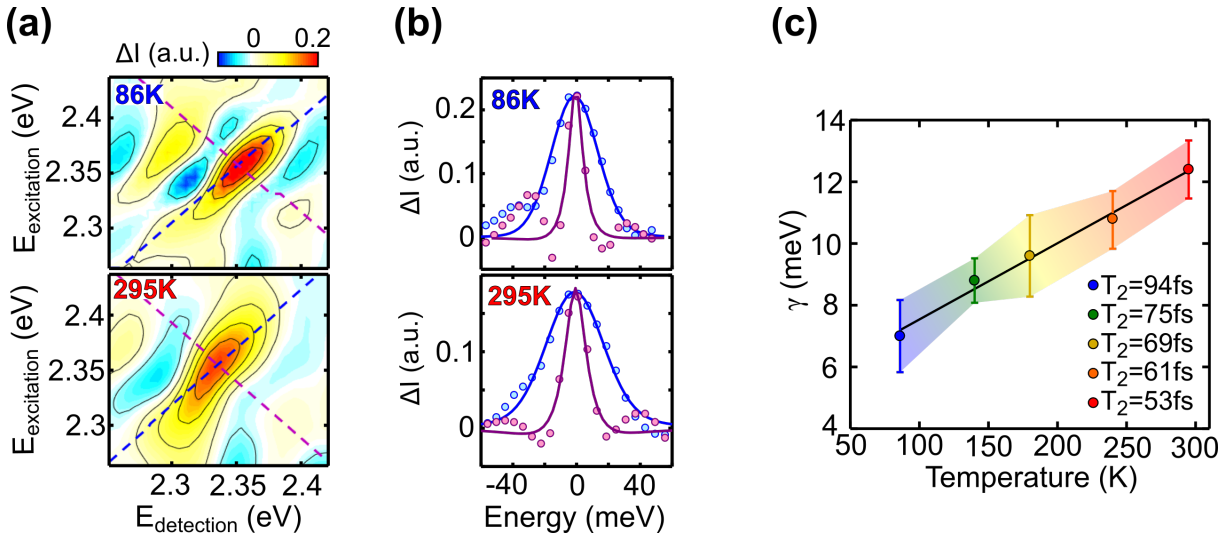

Figure 2.7: (a) Zoomed 2D maps around the diagonal peak and at t_2=10fs measured at 86K (on top) and 295K (bottom); (b) Best fit of the diagonal (blue line) and anti-diagonal (violet) cuts overlapped with the experimental data (symbols) obtained from the dashed lines in panel (a) at temperature 86K and 295K; (c) Temperature dependence of the parameter γ where each point is accompanied with error bars and the respective depahsing time T_2.

2D map for t_2=0:

$$S(t_1,t_3) = FT \begin{cases} S_R e^{-i\omega_0(t_3-t_1)} e^{-(t_3+t_1)\gamma} e^{-\sigma^2(t_1-t_3)^2/2} \\ + \\ S_{NR} e^{-i\omega_0(t_3+t_1)} e^{-(t_3+t_1)\gamma} e^{-\sigma^2(t_1+t_3)^2/2} \end{cases} \tag{2.2}$$

where S_R and S_{NR} are the amplitudes of the rephasing and non rephasing signals, γ is the dephasing rate, σ is the inhomogeneous linewidth and ω_0 is the transition frequency which is, in our specific case, fixed at ω_0=2.25eV. This function allows to simulate the entire 2D map and, by varying the amplitudes (S_R and R_{NR}) and the linewidth parameters (γ and σ), it is possible to find the best fit for the experimental data. The diagonal and anti-diagonal lines are extracted from the 2D map by introducing a pair of new axis that are rotate by 90 degree with respect to the excitation and detection axis and origin located in the center of the peak [26]. Figure 2.7a shows the zoomed 2D spectra at t_2=10fs acquired at temperatures 86K (on top) and 295K (bottom) where the pair of new axis are indicated as colored dashed lines. These two lines correspond to the diagonal and anti-diagonal directions. Figure 2.7b shows the diagonal and anti-diagonal lines at temperatures 86K (on top) and 295K (bottom) where the experimental data (symbols) are overlapped with the best fit (continuum lines) obtained from the Eq. 2.2. We can notice

that the linewidth along the anti-diagonal seems larger at 295K with respect to the one at lower temperature. For this reason, we have decided to perform a temperature dependence by repeating the same experiment at other temperatures: 140K, 180K and 240K. Table 1 contains the value of the parameters obtained from the best fit for every temperature. From this value, we can notice that the dephasing rate increases with the temperature, but the parameter σ does not shows a strong dependence with the temperature.

T (K)	**86K**	**140K**	**180K**	**240K**	**295K**
γ(meV)	7	8.8	9.6	10.8	12.4
σ(meV)	18.7	24	19.2	20.2	21.8
S_R (10^{-5})	1.8	2.46	1.87	2.39	2.92
S_{NR} (10^{-5})	1.4	1.53	1.14	0.7	1.43

Table 2.1: Values of the parameters γ, σ, S_R and S_{NR} obtained from the best fit at temperatures: 86K, 140K, 180K 240K and 295K

Figure 2.7c shows the estimated dephasing rate as a function of temperature, where each value is accompanied with the error bar of each best fit. In the same graph, we report the respective depahsing times for each value of γ and the best fit (black line) obtained with a linear function. Such result is also confirmed from previous studies where the temperature dependence of the dephasing rate was predicted with different methods. The increasing of the dephasing time by slowing down the temperature derives from the interactions between the molecule and the phonons. At lower temperature, such phonons are freezing and the coherence signal from the molecules takes more time to go out of phase [54].

2.3.2. Spectral Diffusion

In this paragraph we study the temporal evolution of the lineshape in order to quantify the spectral diffusion.This effect manifests when the system loses memory of the initial state due to the interaction with the environment. From the experimental point of view, the elliptical lineshape in the 2D map, starts to change till the linewidth of the diagonal and anti-diagonal line are indistinguishable and the homogenous broadening is completely lost (circular lineshape). Several methods were developed in order to study this mechanism but most of them required sophisticated model to extract the bandwidth of the diagonal and anti-diagonal line at different t_2 delays [27]. Here we use a method called Central Line Slope (CLS) in which the lineshape at different t_2 is characterized by an angular coefficient β [55]. Figure 2.8a shows a cartoon of the 2D map in order to understand how

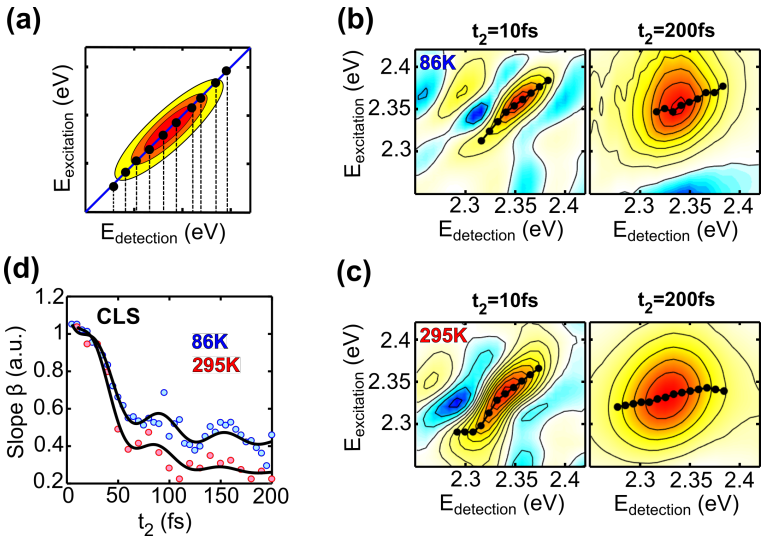

Figure 2.8: (a) Scheme of a single peak in the 2D map at t_2 closed to zero where the maximum amplitude for each detection energy are emphasized with black dots and the blue line represent the linear fit; (b)/(c) zoomed 2D spectra around the diagonal peak at t_2=10fs and 200fs measured at 86K/295K where the black dots indicate the maximum amplitude for each detection energy; (d) Temporal evolution of the slope β at 86K (blue dots) and 295K (red dots) overlapped with the best fit (continuum black lines).

the parameter β can be retrieved. The black dots represent the maximum amplitudes for each detection energies (vertical lines). Such points are then fit with a linear function (blue line) called CLS line where β represents its angular coefficient. Ideally, when t_2=0, β=1 (CLS line along the diagonal) and when the lineshape is circular, β=0 (horizontal CLS line). Figure2.8b and c shows 2D maps at early (10fs) and larger delays (200fs) measured at 86K and 295K where the black dots represent the CLS line. The 2D spectra acquired at early delays show a similar CLS line that follow the diagonal direction. At t_2=200fs, we can notice that at 86K the CLS line still tilted with a certain angle with respect to the detection axis, on the other hand, at 295K, the CLS line is almost flat. The expression of the β as a function of t_2 can assume different forms based of the kind of sample and substrate. Such value is proportional to the frequency fluctuation correlation function ($C(t_2)$) that contains information related to the spectral diffusion and energy fluctuation effects[27]. It is usually expressed with a series of exponential decays when the spectral diffusion is evaluate over a picosecond time scale. In our case, we want to evaluate over a much shorter time window (200fs) where other effects as laser pulse or vibration modes can affect the $C(t_2)$ function. For this purpose, we found a model that can include all of these effects that was inspired by the purposed made by Fecko et. al [56] where the possible vibration molecular modes are modeled as a linear combination

of underdamped and overdamped Brownian oscillators. The final expression adopted for the LFO is:

$$\beta(t_2) \propto C(t_2) = ae^{-t_2/\tau_p} + be^{-t_2/\tau}(cos(\omega_c t_2) + (1/\tau\omega_c)sin(\omega_c t_2)) + c \tag{2.3}$$

where the first exponential reflect the contribution of the laser pulse and τ_p approximate the temporal resolution of the experiment. The vibrational mode is ω_c that was fixed at 540 cm^{-1}, frequency extracted by performing the frequency analysis of the data and τ represents the life time of the mode that was impose similar to the dephasing time estimated in the previous paragraph. The amplitudes a, b and c are the only parameter of the fit. Figure 2.8d shows the best fit (black lines) overlapped with the experimental data (symbols) acquired at 86K (blue) and 295K (red). In conclusion, in this chapter we study three different molecules to show information are possible to extract 2DES experiments.

3 | Natural Light Harvesting Systems

In this chapter we exploit 2DES technique to study ultafast mechanisms in natural Light Harvesting Systems (LHC). Such photosystems can be found in different natural organisms that perform photosynthesis as higher plants, cyanobacteria and algae. In general they are composed of pigment-protein complexes organized in two parts: a peripheral part called light harvesting antenna and an internal part in which the Reaction Center (RC) is located [2]. Such complexes efficiently capture and transfer the solar energy through the RC where a molecule called P700 oxidized by generating the pair $P700^+$ and one electron. Such a charge separation is the starting point of the photosynthesis chemical reaction from which the plant can produce oxygen and glucose [57]. This process come into spot light due to the high energy conversion efficiency (ratio between the number of created charges and the absorbed photons) which is larger than 0.9 and the time scale in which excited state energy transfer (EET) processes are taken place (from femto to picoseconds time scale). For this reason, 2DES technique represents a perfect tool to study these mechanisms by giving a complete spectral and temporal characterization. In this work we study Photosystem I Light Harvesting Complex I (PSI-LHCI) isolated from spinach (higher plants) and the PSI-Core (without the antenna) isolated from Spirulina Platensis (Cyanobacteria). Figure 3.1a shows a simple cartoon of the structure of the two photosystems where the green buttons represent the pigments-protein complexes that are mainly comprised of carotenoids (Car), Chlorophyills (Chls) *a* and *b* usually identified as Bulk and a group of Chls that absorbed at lower energy with respect P700 (absorption peak at 700nm) called red forms (RF) [58]. Figure 3.1 shows the steady state absorption spectra of the PSI-LHCI of higher plants (black line) and PSI-Core of cyanobacteria (violet line) overlapped with the laser pulse spectrum (rainbow area). This graph is grid based of the absorption of Chls Bulk (from 550nm to 690nm), RC identified by the absorption of the P700 and Chls RF (from 700nm to 750nm). The carotenoids are omitted in this graph because their absorption (shorter wavelength with respect 550nm) is not cover from the laser pulse. Both spectra show clearly two peaks centered at 620nm and 680nm that

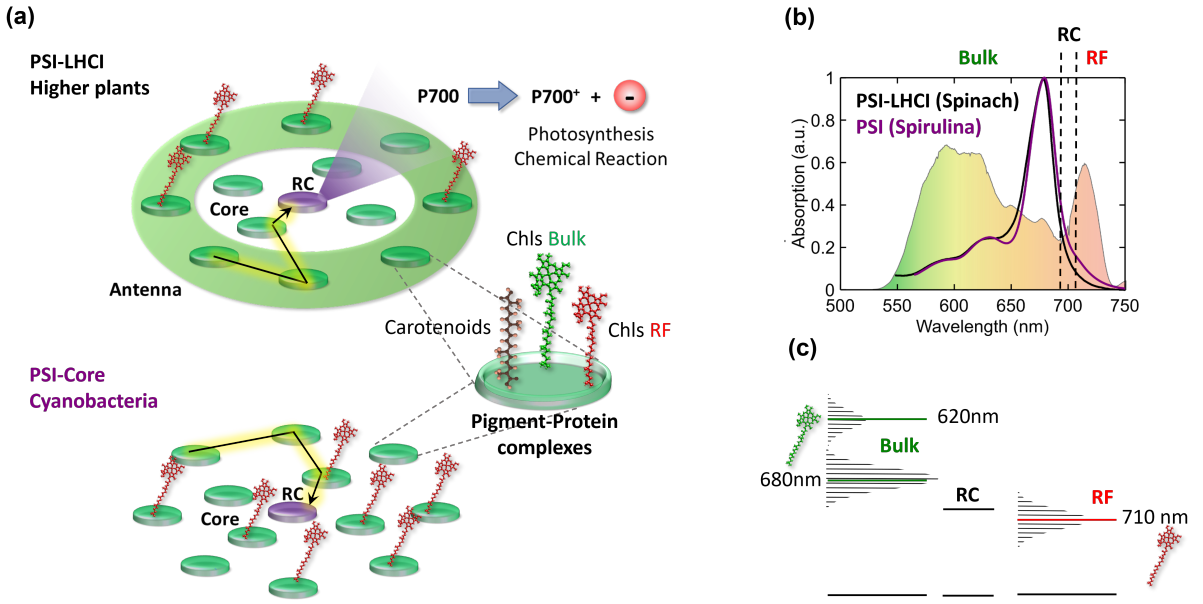

Figure 3.1: (a) Scheme of the PSI-LHCI of higher plant (on top) and PSI- Core of cyanobacteria (bottom) where the pigment-protein complexes are represented as green buttons that contain carotenoids, Chls bulk and Chls red forms; in the same panel are reported the molecular structure of the pigments and a cartoon that represent the EET processes within them (black arrows) and the charge separation process in the RC; (b) Static absorption spectra of the PSI-LHCI (black line) and PSI-Core (violet line) overlapped with the laser pulse spectrum (colored area); (c) Energy level scheme in which the energetic states of the Chls bulk (620nm and 680nm), RC (700nm) and Chls red forms (710nm) are included

correspond to the Q_x and Q_y bands of Chls a. At 650nm, the spectrum of the PSI-core shows a more marked hole with respect to the photosystem of higher plants. At this wavelength there is the peak of the Q_y band of Chls b that are located only in the antenna part and not in the core [7]. The main difference between the two spectra, appears at larger wavelength where the Chls RF absorbed. In particular, the PSI-core shows an higher intensity with respect the PSI-LHCI. The reason is related to the amount of Chls RF in both systems and their localization. In higher plants, such Chls harbor in the LHC antenna [8] and, in cyanobacteria, they are spread in all the core as it is illustrated in figure 3.1a [59]. Figure 3.1c shows the energy level scheme derived from the static absorption spectrum where the Chls Bulk are represented by the two bands of Chls a, the RC at 700nm and the Chls RF peaked at 710nm. The study of the Chls RF attracts several interest because, even if they absorbed at lower energy with respect the RC, their role in the photosynthesis process still not fully understood. In the next sections we exploit 2DES results and analysis of both photosystems in order to spectrally and temporally

characterize all the EET mechanisms within the two kind of Chls. In the last section we compare the results of the two systems by giving the predicted deactivation energy level scheme and relative interpretation.

3.1. PSI-LHCI (Core-Antenna) in Higher plants

Photosystem I Light Harvesting Complex I (PSI-LHCI) in higher plants shows the highest quantum conversion efficiency ($\simeq 0.98$)[2] with respect the other photosystems known in nature. This high efficiency persist even if there are Chls RF that could limit the EET process to the RC; in particular it was proposed a termodynamically unfavorable uphill EET from Chls RF to Chls Bulk that can slow down the charge separation/energy trapping mechanism[60]. The characterization of the EET processes in this photosystem could be complicated and the main reasons are: (i) the time scale of the different EET mechanisms are similar and they overlapped with the charge separation and stabilization steps; (ii) the large number of pigments in each units ($\simeq$ 150 Chls) implies a broadly spectral absorption of the photosystem where is difficult to distinguish contribution that coming from different species [5]. For this reason, in order to understand the effects on EET processes imposed by the low energy Chls, we need to perform experiments in which such Chls are directly excited. Here we use 2DES technique with a laser pulse spectrum spanning from 580nm to 725nm in order to well cover the absorption of Chls bulk and Chls RF. Furthermore, we study the PSI-LHCI in two conditions: open and closed RCs. The second condition was obtained by oxidizing the primary donor of the RC (P700) with Ferry cyanide in order to avoid energy trapping mechanism. The details of the sample and the experimental parameters are reported in appendix A.

3.1.1. 2DES Results

Figure 3.2a shows the pure absorptive 2D spectra of PSI-LHCI under open RCs condition at t_2=75fs, 1ps, 10ps and 50ps that are grid based on the absorption of Chls Bulk and Chls RF. At t_2=75 fs, the 2D map shows two diagonal peak at 680nm/680nm and 710nm/710nm excitation/detection wavelength. Such points corresponds to the GSB signal of the Q_y band of Chls *a* and Chls RF respectively. In this map is also present a strong cross peak by exciting at 620nm and detecting at 680nm which correspond to the EET process from the Q_x to Q_y band of Chls *a*. The absence of the diagonal peak associated with the Q_x band suggests that such a process take place in a time scale which is faster with respect the temporal resolution of the experiment. We can also notice that the lineshape of the diagonal peak st 680nm/680nm is mostly elliptical by covering also vi-

brational states of the Q_y band located around 670nm. The Coupling within these states mediate an ultrafast intramolecular EET process in which the energy will be localized in the dominant absorption peak centered at 680nm. This effect can be observe in the 2D map at t_2=1ps where the energy obtained by exciting around 670nm is completed transfer, by creating a cross peak at 680nm. The negative amplitude in this 2D map represents the ESA signal from Chls Bulk that could mask some vibrational coupling effect. At early waiting times, it is possible to observe a formation of a cross peak by exciting at 710nm and detecting at 680nm. Such a peak is correlated to the coupling between the Chls RF and Chls bulk which is usually refereed as uphill EET. 2D map at t_2=10ps shows cross

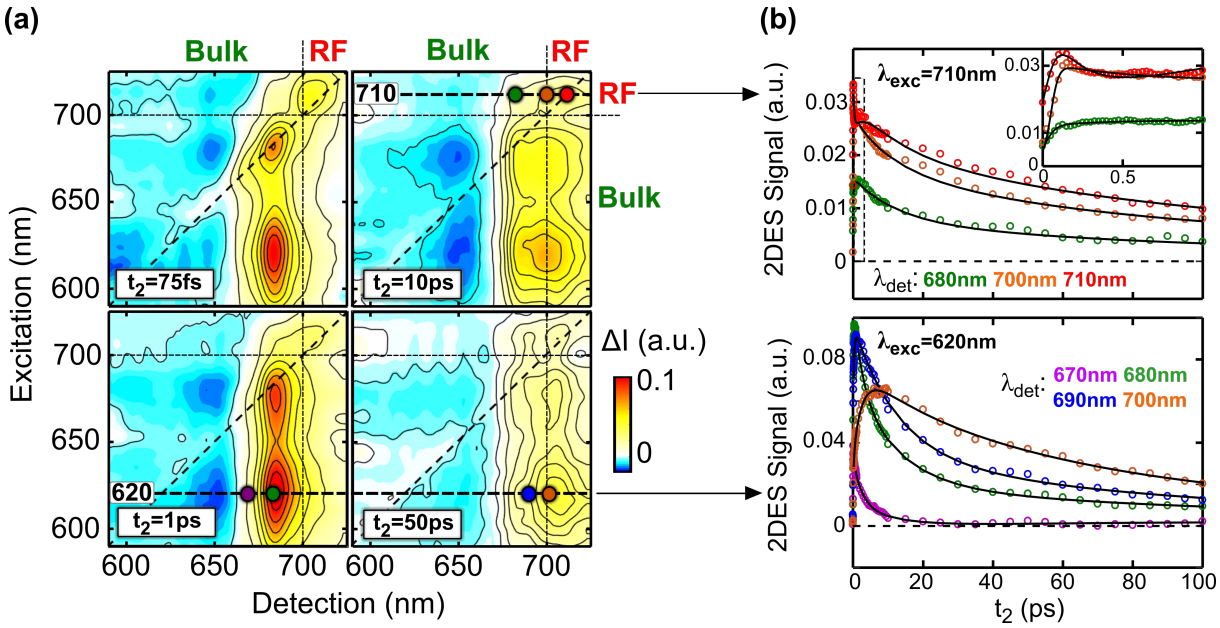

Figure 3.2: (a) 2D pure absorptive spectra of PSI-LHCI under open RCs at t_2=75fs, 1ps, 10ps and 50ps where each map is grid based of the absorption of the Chls bulk and Chls red forms; (b) on top: t_2 traces obtained by exciting at 710nm and detecting at 710nm (red), 700nm (orange) and 680nm (green) where a zoomed of the dynamics up to 1ps is reported in the same graph as a inset; bottom: t_2 traces obtained by exciting at 620nm and detecting at 670nm (violet), 680nm (green), 690nm (blue) and 700nm (orange). In both plots, the relative points are emphasized in the panel (a) with colored circles and the experimental points (symbols) are overlapped with the best fit (black continuum line) obtained from the global analysis

peak detected at 700nm and 710 nm when the system is excited at 680nm and 620nm (Chls bulk). Such peaks indicate an EET from the Chls Bulk to the RC and Chls RF and this mechanism is usually label as downhill EET. At t_2=50ps, the energy that was stored in the Q_y band of Chls *a* is completely disappear and the energy is mainly localized at detection wavelength larger than 700nm. In order to better visualize all of these processes

detected by 2DES experiment, we can observe the dynamics of the diagonal and cross peaks.. Figure 3.2b shows the dynamics of the colored points indicated in the 2D maps when the system is excited at 710nm (on top) and 620nm (bottom). The black continuum lines in the plots represent the best fit obtained with the global analysis algorithm that will be explained in the next section. By directly exciting Chls RF (710nm), the associated GSB signal (red point) shows two different decays. The first one is ultrafast and it match with the formation of the cross peak detected at 680nm (green point), by revealing the uphill EET mechanism. Such dynamics is more visible in the inset reported in the same graph where the dynamics are zoomed up to 1ps. The second decay is slower with respect the first one and it represents the relaxation to the ground state. Similar decay is also present in the cross peaks detected at 680nm and 700nm (orange point). The Downhill EET that was mentioned before, can be observed in the bottom panel of figure 3.2b where the system is excited at 620nm (Q_x band). The dynamics detected at 670nm (violet point) shows an ultrafast decay that is similar to the formation of the signal at cross peaks detected at 680nm (green point) and 690nm (blue point). This mechanism is related to the intramolecular relaxation of Chls bulk from the high vibrational energy levels to the lower one. The downhill EET process from the Chls bulk to the RC and Chls RF is identified by the decaying signal detected at 680nm that match with the rise time detected at 700nm (orange point). The data obtained at closed RCs condition show a similar behavior [5] and the main difference between the two conditions will appear when 2DES data are analyzed with global analysis algorithm which results are reported in the next section.

3.1.2. Data analysis

In order to temporally and spectrally characterized the EET and energy equlibration mechanisms in the PSI-LHCI, we performed the global analysis algorithm on the 2DES data. This procedure allows to model the entire 2DES dataset with a series of n exponential decays with the following expression:

$$S(\lambda_{exc}, t_2, \lambda_{det}) = \sum_{n}^{i=1} A_i(\lambda_{exc}, \lambda_{det}) e^{-t_2/\tau_i} \tag{3.1}$$

where the amplitudes A_i are 2D amplitude maps as a function of the excitation and detection wavelengths and are called Decay Associated Spectra (2D-DAS). Such maps are correlated to a specific time constant denoted with τ_i. The amplitude of the 2D-DAS reveals the decay or a formation of a specific species; in particular, a positive amplitude indicates a positive exponential decay which correspond to a decay of GSB signal; a

negative amplitude represents a negative exponential decay that correspond to a formation of a GSB signal or a decay of an ESA signal [61]. In this section we show the results of the global analysis for the PSI-LHCI system under open and closed RCs conditions. The

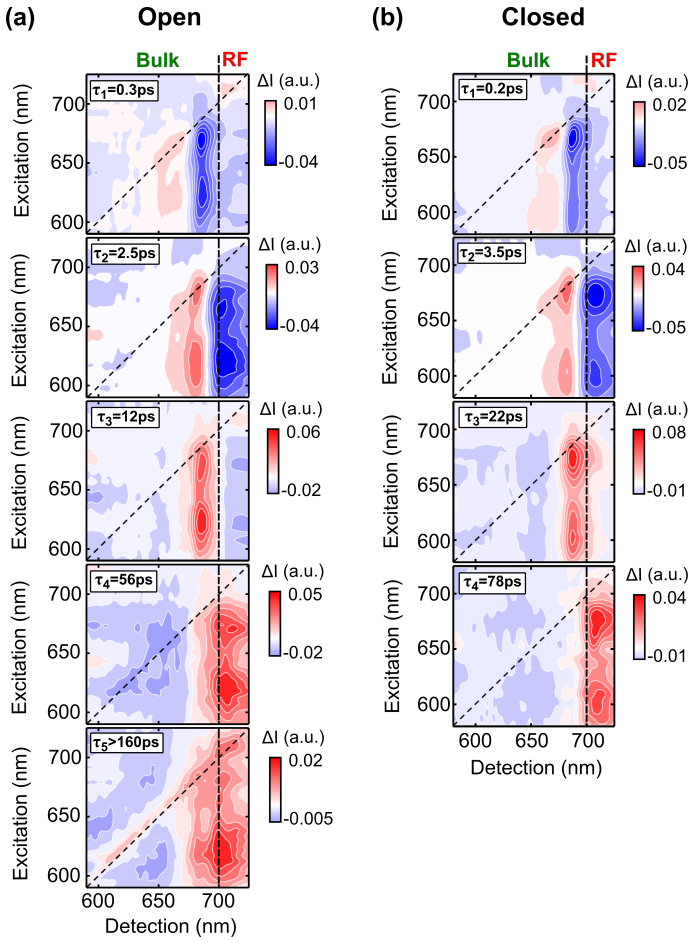

Figure 3.3: (a) 2D-DAS map obtained from the PSI-LHCI under open RCs condition where the temporal evolution can be described with time constants: τ_1=0.3ps, τ_2=2.5ps, τ_3=12ps, τ_4=56ps and a non-decaying component limited by the time window adopted to perform the experiment; (b) 2D-DAS map obtained from the PSI-LHCI under closed RCs condition where the temporal evolution can be described with time constants: τ_1=0.2ps, τ_2=3.5ps, τ_3=22ps, τ_4=78ps

best fit of the PSI-LHCI under open condition is obtained by imposing n=5 and the 2D-DAS and the related time constant are reported in figure 3.3a. Such lifetimes are: τ_1=0.3ps, τ_2=2.5ps, τ_3=12ps, τ_4=56ps and a non-decaying component which is larger with respect the time window adopted for the experiment (160ps). Such values are in a good agreement with those reported by performing a pump probe experiment on the same sample [62]. The 2D-DAS associated with the life time τ_1=0.3ps shows a signal decaying from 650nm to 675nm spectral region and a formation around 680nm. This corresponds to an intramolecular energy equilibration within the Q_y band of Chls bulk.

We can also notice that by exciting at larger wavelength with respect 700nm, the 2D-DAS shows a positive amplitude for the GSB signal of Chls RF and a negative amplitude of the cross peak detected at 680nm. This demonstrate the presence of an uphill EET from the Chls RF to the Chls bulk that take place in a time scale similar to the intraband EET process. The second 2D-DAS shows a decay in the Q_y band of the Chls bulk and a formation in the spectral region spanning from 700nm to 735nm. This means that, the time constant of τ_2=2.5ps temporally defined the downhill EET process from Chls bulk to the low energy Chls and RC. The life time of 12ps is dominated by the relaxation of the Chls bulk that overlap with the energy trapping time. In particular, once the P700 is completely oxidized, the energy from the Chls bulk will relaxed to the ground state instead to be transfer to the RCs. The 2D-DAS at τ_4=56ps shows a decay above 700nm spectral region which correspond to the relaxation of the Chls RF. The longest component should represent the long-lived signal associated with the $P700^+$ that has usually a lifetime of microseconds. Unfortunately, due to our limited time window, such time can not fully isolated and, for this reason, it is possible to observe in the 2D-DAS some decaying related to Chls RF. In general, with the global analysis, is difficult to distinguish processes that take place with similar time scales. From this view, we performed the same kind of analysis for the PS-LHCI under closed RCs where the best fit is obtained by imposing the number of components n=4. Figure 3.3b shows the 2D-DAS map obtained for closed RCs configuration which lifetimes are: τ_1=0.2ps, τ_2=3.5ps, τ_3=22ps and τ_4=78ps. The first 2D-DAS is similar to the first map in the open configuration and it describes the same intramolecular and uphill EET processes. The second lifetime describes the downhill EET process from Chls bulk to Chls RF which is slower with respect the lifetime found for the open configuration (2.5ps). Such a discrepancy derives from the EET from Chls bulk to RC which is only present in the open RCs sample; in particular the faster lifetime indicates a faster transfer from bulk to RC with respect the transfer from bulk to RF. The third 2D-DAS shows a lifetimes which is almost double with respect the open condition. In this case it represent only the relaxation of the Chls bulk that is note influenced by the energy trapping in the RC. The last 2D-DAS shows a decay of Chls RF which is larger with respect the 56ps found for the open case that was probably mediated with the relaxation time of the P700. In summary, by exploiting 2DES technique we have characterized the main EET processes in PSI-LHCI in higher plants; in particular, the ultrabroadband laser pulse adopted for the experiment allows to monitor the effects of the Chls RF in the EET/energy trapping mechanism in terms of lifetime. Even if Chls RF are situated in the antenna part, the uphill EET from Chls RF to Chls bulk observed in the 2DES data demonstrates that the overall energetic equibration depends only on the energy levels of the different chromophores rather than their specific location. In

particular, Chls RF participate to the photosynthesis process and their effect does not impact negatively to the efficiency of the entire photosystem. In the next section we repeat the same experiment and analysis for the PSI-core in cynaobacteria in which the Chls RF are distributed in the core complex part.

3.2. PSI (Core) in Cyanobacteria

In this section we report the results and the analysis of the 2DES data obtained from PSI-core isolated from Spirulina platensis (cyanobacteria class). Such organism shows the highest concentration of Chls RF in nature located in the core complex part. The dimension of the PSI-units counts almost 80 Chls which is almost the half amount with respect the PSI-LHCI studied in the previous section [59]. For this reason, it is particularly suited to study the effect of the Chls RF that usually have a lower intensity absorption with respect the Chls bulk.

3.2.1. 2DES Results

In this section we show the 2DES results obtained for PSI-core isolated from Spirulina platensis under closed RCs in order to avoid electron transfer process that can kinetically overlaps with the EET mechanisms. In literature, this sample is usually studied under trimeric and monomeric form where only fluorescence and transient absorption measurements were performed [59]. Here we explore for the first time 2DES experiment on the trimeric and monomeric form in order to spectrally and temporally characterized the low energy Chls role in terms of EET mechanisms. The details related to the samples and the parameters adopted in order to perform experiments are reported in appendix A. Figure 3.4a shows the pure absorptive 2D spectra of the trimeric form detected at t_2=25fs, 1ps, 5ps and 20ps that are grid based on the absorption bands of Chls bulk and Chls RF. 2D map at t_2=25fs shows two diagonal peak: the first one is peaked at 680nm/680nm excitation/detection wavelength by showing an elliptical lineshape elongated along the diagonal line; the second one is peaked at 710nm/710nm point and it corresponds to the GSB signal associated with the Chls RF. In this 2D map we can also observed a cross peak at the 620nm/680nm point that reflects the downhill EET from the Q_x band to the Q_y band of Chls bulk as it was observed for the PSI-LHCI complex. At t_2=1ps, the lineshape of the GSB signal associated with the Q_y band of Chls bulk changed, by showing a circular shape. This effect is probably due to the spectral diffusion effect that the system experienced with the environment (distilled water). In the same 2D spectrum, we can also observed a formation of a cross peak by exciting at 710nm and detecting at 680nm. Such a peak correspond to the uphill EET from the Chls RF to Chls bulk thanks to the coupling between them. The downhill EET from Chls bulk to Chls RF is represented by the cross peaks at t_2=5ps obtained by exciting at 680nm and detecting in the spectral region from 700nm to 750nm. In particular, such a broad peak seems composed by two peaks: one peaked at 710nm and the other at 730nm. From the 2D map at t_2=20ps we

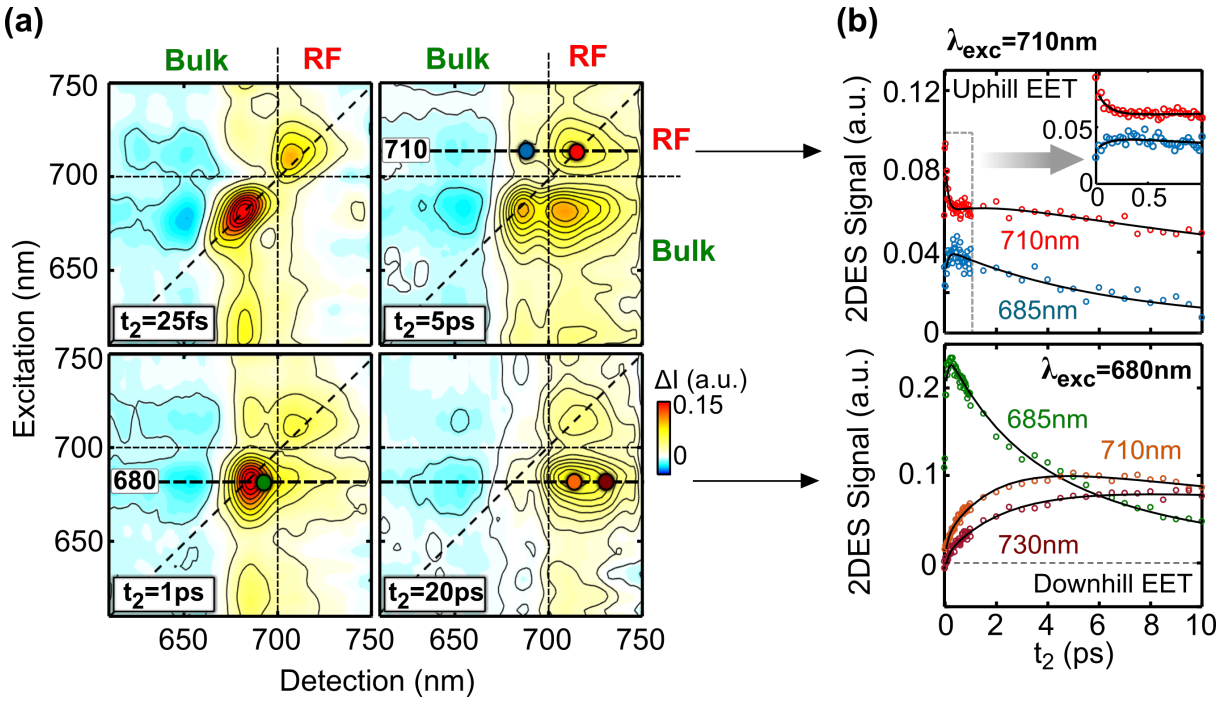

Figure 3.4: (a) 2D pure absorptive spectra of PSI-Core trimeric form under closed RCs at t_2=25fs, 1ps, 5ps and 20ps where each map is grid based of the absorption of the Chls bulk and Chls red forms; (b) on top: t_2 traces obtained by exciting at 710nm and detecting at 710nm (red) and 685nm (blue) where a zoomed of the dynamics up to 1ps is reported in the same graph as a inset; bottom: t_2 traces obtained by exciting at 680nm and detecting at 685nm (green), 710nm (orange) and 730nm (dark red). In both plots, the relative points are emphasized in the panel (a) with colored circles and the experimental points (symbols) are overlapped with the best fit (black continuum line) obtained from the global analysis

can observe the decay of the energy stored in the bulk and the presence of a long-lived signal associated with the low energy Chls. Both downhill and uphill EET mechanisms are clearly visible in the dynamics of the diagonal and off-diagonal peaks indicated in the 2D maps with colored circles. Figure 3.4b shows the t_2 traces of that points where the colored symbols represent the experimental data and the continuum black lines indicate the best fit obtained with global analysis. When the system is excited at 710nm, the dynamic of the GSB signal associated with Chls RF (red point) shows two different decays; one is ultrafast and it match with the rise of the cross peak detected at 680nm (uphill EET) and a slower second one that represent the relaxation to the ground state. The cross peak detected at 680nm, after the ultrafast rise, shows a decay that is faster with respect the diagonal peak at 710nm. The sub ps dynamics is emphasized in the inset where the same t_2 traces are reported in a time window up to 1ps. The dynamics trend completely change if the system is excited at 680nm (figure 3.4b bottom panel). In this

case, the dynamics detected at 685nm (green point) shows a sub-ps formation due to the intramolecular relaxation in the Chls bulk, followed by a sub-20ps decay. The dynamics of the cross peaks detected at 710nm (orange point) and 730nm (dark red point) show a rise time that almost match with the decay of the signal detected at 685nm, pointing out the downhill EET. We perform the same experiment also for PSI-Core of Spirulina platensis in the monomeric form where the trend of the 2D maps and the dynamics is similar. We can appreciate the differences between the two samples by looking the results obtained with the global analysis that will present in the next section.

3.2.2. Data analysis

In order to temporally and spectrally characterized the EET processes that are taking part in this complex, we performed global analysis of the 2DES data obtained from the PSI-core in the trimeric and monomeric form. Figure 3.5 shows the results of the global analysis in terms of 2D-DAS of both systems where the best fit was found by considering n=4 components. Figure 3.5a shows the 2D-DAS obtained from the trimer accompanied with the relative lifetimes: τ_1=100fs, τ_2=2ps, τ_3=6ps and τ_4=43ps. In the first 2D-DAS, by exciting at 680nm, we can observe a decay (positive amplitude) detected around 670nm and a formation (negative amplitude) detected at 680nm. This process correspond to an ultrafast energy equilibration within the Chls bulk.The same spectra can be observed also by exciting at shorter wavelength around 620nm. In the same time scale, by exciting at larger wavelength with respect 700nm, we can observe a decay of the GSB signal of the Chls RF and a formation detected at 680nm. This result unambiguously identifies the uphill EET that was also observed in the PSI-LHCI. In the 2D-DAS associated with τ_2=2ps, we can observe a decay of the Chls bulk and the formation in the Chls RF spectral region that represents the downhill EET process. The match between the modulus of the positive and the amplitudes suggests that no other processes are involved with that lifetime. The third 2D-DAS (τ_3=6ps) shows a positive amplitude detected at shorter wavelength with respect 700nm (Chls bulk) and a negative signal detected around 730nm. The stronger positive amplitude, suggests that the dominant process is the relaxation of the Chls bulk to the ground state. The presence of a weak negative amplitude at longer wavelength could represent an EET process from the Chls bulk to the more red shifted absorption peaks of Chls RF. The last 2D-DAS shows the decay of the Chls RF where it is possible to identify two peaks associated with the Chls RF; one at 710nm and the other at 730nm. Figure 3.5b shows the 2D-DAS obtained from the global analysis of the PSI-core monomeric form with the relative lifetimes: τ_1=520fs, τ_2=5.4ps, τ_3=30ps and a non-decaying component. The first 2D-DAS is similar to the one obtained from the

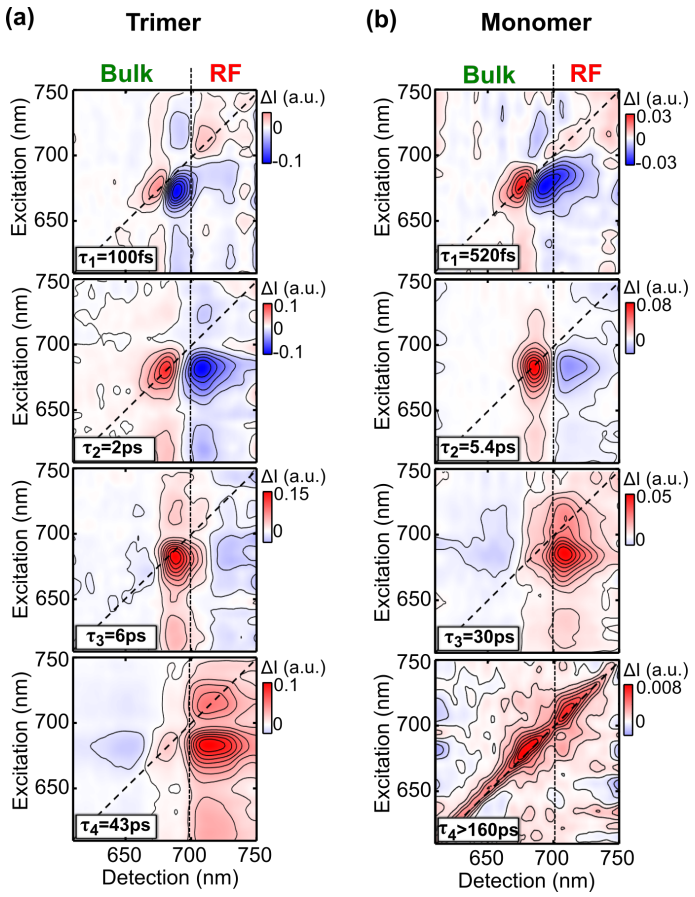

Figure 3.5: (a) 2D-DAS map obtained from the PSI-Core trimeric form under closed RCs condition where the temporal evolution can be described with time constants: τ_1=100fs, τ_2=2ps, τ_3=6ps and τ_4=43ps; (b) 2D-DAS map obtained from the PSI-Core monomeric form under closed RCs condition where the temporal evolution can be described with time constants: τ_1=520fs, τ_2=5.4ps, τ_3=30ps and a non-decaying component limited by the time window adopted fro the experiment

trimer, but the time constant in which the two processes (energy equilibration in the Chls bulk and the uphill EET) is five time slower with respect the trimeric form. The 2D-DAS characterized by a lifetime τ_2=5.4ps shows a decay at main absorption peak of Chls bulk and a formation in the Chls RF. The mismatch between the positive and the negative amplitudes suggest that more then one process are included in this 2D-DAS. In particular, the weak negative amplitude detected above 700nm indicates that only a small portion of energy is transferred from the Chls bulk to low energy Chls. The dominant effect is represented by the positive amplitude detected around 680nm, which correspond to the relaxation of Chls bulk to the ground state. For this reason, the time constant of 5.4ps is a balance between the two processes that are taken place with a similar time scale. The 2D-DAS associated with τ_3=30ps represents the relaxation of the Chls RF which show

a shorter absorption bandwidth with respect the trimeric form. This difference was also observed in a previous work by performing fluorescence experiment on the same samples [59]. The last 2D-DAS shows a very weak amplitude with respect the others and it mainly represent the residual pump pulse scattering of the experiment. By comparing the lifetimes τ_1 and τ_2 obtained for the trimer and monomer, we can notice that the uphill and downhill EET processes are faster in the trimer with respect the monomer. This means that in the trimer there are specific interactions that facilitate the energy diffusion in the entire photosystem. Furthermore, the time constant of 5.4ps found for the monomer contains contrbutions from two different steps (relaxation of Chls bulk and pure downhill EET from bulk to RF), but in the trimer, such processes are well distinguishable with time constant of 2ps and 6ps. On contrary the relaxation of the Chls RF seems slower in the trimer with respect the monomer. In the last section of this chapter we compare the results obtained for PSI isolated from the higher plants and cynaobacteria.

3.3. Higher plants vs Cyanobacteria

In this section we compare the results obtained from the PSI-LHCI isolated from spinach under closed RCs and the PSI-core trimeric form (closed RCs) isolated from the Spirulina platensis by proposing a deactivation energy level scheme. Figure 3.6a shows the predicted deactivation energy level scheme for the PSI-LHCI of higher plants under closed RCs where each processes are represented with colored arrows accompanied with their specific lifetimes. The downhill EET from high energy Chls to the main absorption of Chls bulk and the uphill EET from the Chls RF to Chls bulk are characterized by a time constant of 200fs. The pure downhill EET from bulk to low energy Chls take place in 3.5ps and the relaxation of Chls bulk and RF take place in 22ps and 80ps respectively. Figure 3.6 shows the predicted deactivation energy level scheme associated with the PSI-core trimeric form where the uphill and downhill mechanisms are characterized with similar time scales found for the higher plants complex (100fs and 2ps). The third lifetime (6ps) combine two different processes; the first one is the relaxation of the Chls bulk to the ground state and the second one is a downhill EET to the more red shifted Chls which absorption is peaked at 730nm. This result suggest that these two relaxation channels from the bulk take place with a similar time scale, by making this mechanism faster in the cyanobacteria with respect the higher plants. The last time constant of 43ps correspond to the relaxation of the Chls RF that is almost two times faster with respect the relaxation of the same Chls in the PSI-LHCI. This difference can be related to the amount and position of this Chls in both systems. In the higher plants supercomplex, these Chls are located only in the antenna (far from the RC) in which less interaction are present with respect

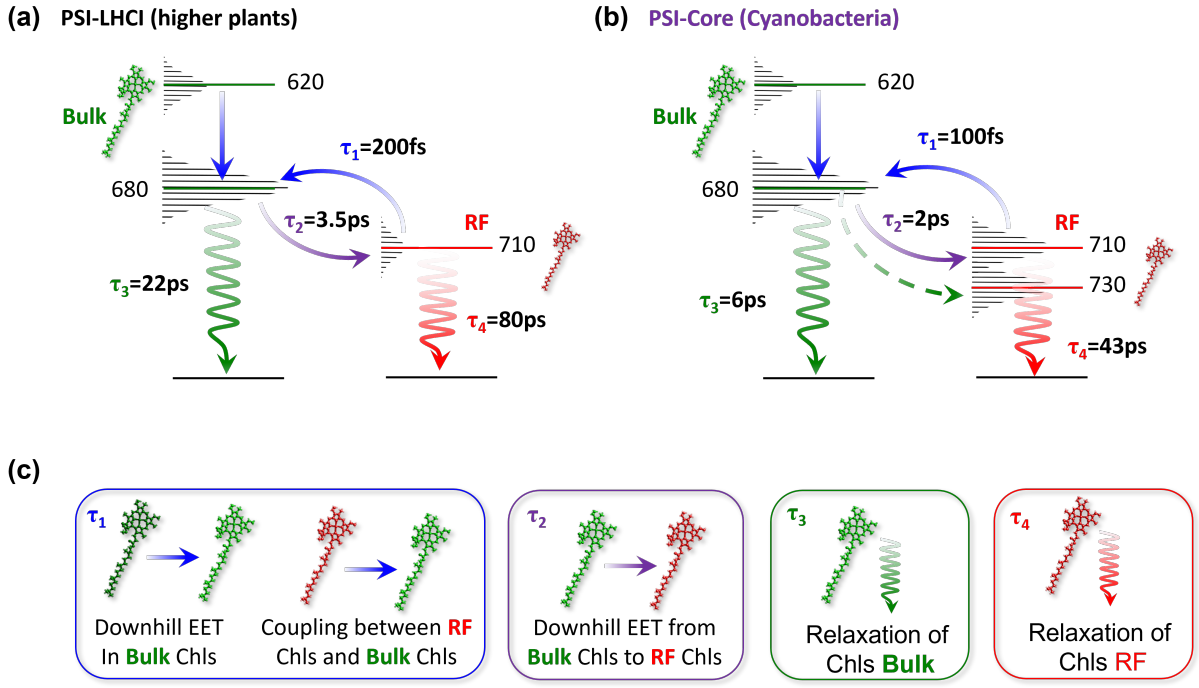

Figure 3.6: (a) Predicted deactivation energy level scheme for the PSI-LHCI isolated from spinach under closed RCs condition; (b) Predicted deactivation energy level scheme for the PSI-Core trimeric forms isolated from Spirulina plantensis under closed RCs. I both scheme, each processes indicated by a colored arrows are with the respective time constant; (c) Schematic representation of the different steps that are taking place in both systems with their specific time scales; τ_1(blue): energy equilibration in Chls bulk and uphill EET from Bulk to Chls RF, τ_2: downhill EET from Chls bulk to Chls RF, τ_3: relaxation of Chls bulk and τ_4: relaxation of Chls RF

the Chls situated in the core. Figure 3.6c summarizes the different processes that are involved in both systems where each interaction is labeled with its specific time constant. In conclusion, these results related to both natural light harvesting systems are relevant from the biology point of view for the comprehension of the photosynthesis process in different organisms and for the design of innovative artificial photosystems.

4 | Bio-inspired Light Harvesting Systems

In the previous chapter we have demonstrated the efficiency of the natural light harvesting systems to transfer and convert solar energy into chemical energy. Such processes take place in fs/ps time scale and the presence of low-energy Chls does not affect the production of free charges in the reaction center. However the ratio between the effective fuel and the photons absorbed is around 0.2 which means that the largest part of the charges created after the absorption of light is wasted due to a fast charge recombination process that usually take place in hundreds ps time scale. Another aspect that can be optimized in the natural photosystems is the distance in which the energy transfer within Chls take place. In particular, the EET mechanism is possible because the distances between the molecule is less than the typical Förster radius (10nm), but this phenomenon ruled out any possible EET for larger distances. In this chapter we study two different artificial bio-inspired light harvesting system that allow to overcome these negative aspects. The first one is inspired by the Quantasome concept and it allows to increase the charge recombination time from ps to ns time scale. The second structure is studied in order to have EET process between two spatially separated molecules which distance is in the order of micrometer.

4.1. Artificial PSII supercomplex

The possibility to generate renewable energy from artificial photosystems that bio-mimic the natural one still a big challenge. The main interest focus on the water oxidation and reduction processes that are performed in nature by photosysthems II and I (PSII and PSI) respectively. In this context, the minimal unit responsible for the energy conversion in both systems, called Quantasome, come into spot light as a reference in order to engineer robust architectures for artificial light harvesting. Figure 4.1a shows a schematic structure of the quantasome unit that is composed by a self-assembled light harvesting antenna and a catalytic cofactor located in the center. The antenna is comprised of pigment protein-complexes that capture and transfer the solar energy through the catalyst

in which charge separation and chemical reaction take place. In this figure we represent the case of the PSII that is responsible of the water oxidation mechanism in which the the oxygen is isolated from the water via four electron/four proton chemical reaction: $2H_2O \rightarrow O_2 + 4H^+ + 4e^-$. The main problems that reduce the efficiency of this mechanism are related to the favorable charge recombination in the water oxidation catalyst (WOC) and the photo-degradation induced by the excessive solar energy. Such aspects are also common in artificial photosystems that explore dyads arrangements [63]. In this

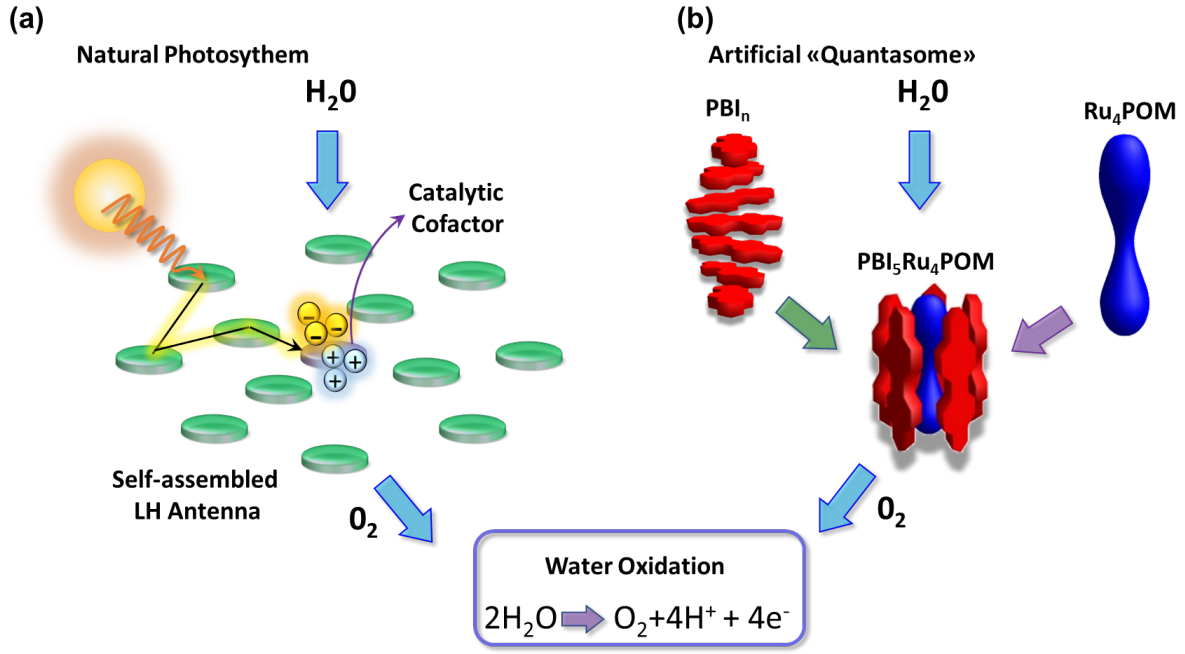

Figure 4.1: (a) scheme of a natural photosystem unit composed of self-assembeled antenna (green buttons) and a Catalytic cofactor located in the center where the charge separation take place after the absorption and transfer of the solar energy; (b) scheme of the artificial quantasome ($[PBI]_5Ru_4POM$) synthesized by mixing PBI_n h-aggregate and ruthenium based polyoxometalate (Ru_4POM). The light blue arrows indicate the reagents and products of the water oxidation chemical reaction

chapter we study an innovative artificial quantasome architecture that explores Perylene Bisimide (PBI) molecule as light harvesting antenna and ruthenium-polyoxometalate as a WOC [10]. By dissolving the PBIs molecules in distilled water, such molecules are piled up creating H-aggregate units as is shown on top of the figure 4.1b. When PBI_n aggregates are combined with the polyoxometale (Ru_4POM), they self-assemble around each photocatalyst, by generating units with the following stoichiometry formula: $[PBI]_5Ru_4POM$ as is shown in the figure 4.1b. In the previous work published by Bonchio and coworkers, they demonstrate that such units are self-assembled in 2D pattern that mimic the

chloroplast membrane that is presents in natural photosystems. In the following section we exploit 2DES and pump probe experiments in order to characterize the formation and the recombination of the charges in the $[PBI]_5Ru_4POM$ and PBI_n aggregate structures. The details related to the samples characteristics and the experimental parameters are reported in appendix A.

4.1.1. Tracking Charge Dynamics

In this section we explore ultrafast spectroscopy techniques in order to evaluate the artificial quantasome performances with respect the structure composed by PBIs H-aggregate. Figure 4.2a shows the steady absorption of the PBI_n aggregate (red) and the artificial quantasome (green). In both structures there are two main absorption peaks located in the visible spectral region; specifically at 500nm and 540nm for the PBI_n and red-shifted peaks at 510nm and 560nm for the $[PBI]_5Ru_4POM$ unit. We can immediately notice that the combination with the Ru_4POM increase the light harvesting capacity of the system due to a broader absorption spectrum. We start the analysis of the two structure by performing 2DES experiment in order to evaluate any possible differences that take place on ultrafast time scale. Figure 4.2b shows the pure absorptive 2D spectra of the PBI_n at t_2=0.1ps and 1ps. At t_2=0.1ps we can distinguish between GSB signal (positive amplitude) along the diagonal line that reflects the absorption of the molecules and the relative cross peaks due to the coupling between the two electronic states. At t_2=1ps, the positive signal does not change their amplitude, but there is a significant formation of the ESA signal detected around 600nm. Figure 4.2c shows the pure absorptive 2D spectra of the artificial quantasome structure measured at the same t_2 delays reported for the PBI_n. In this case, the GSB signal of both absorption peaks and the relative cross peaks are more marked with respect the PBIs structure and the ESA signal does not show a strong variation passing from 0.1 ps to 1ps delays. In general, in both systems, the GSB signal are instantaneous and do not present any ultrafast processes. On contrary, the ESA signal detected around 600nm, shows a variation within 1ps time window. Figure 4.2d shows the dynamics of the ESA signal for the quantasome structure and the PBI_n at the excitation/detection wavelength point marked with with green circle and red square respectively in the 2D maps reported in the panels b and c . In particular, such points are obtained by exciting at the lower-energy absorption peaks that are 560nm for quanatsome and 540nm for PBI_n and detected at 620nm. The dynamics show a different rise time that was estimated around 140fs for the quantasome and 800fs for the PBI_n aggregate. These values are obtained by performing a single dynamics fit which results are reported in the same plots as continuum colored line. The meaning of the ESA signal can be deduced

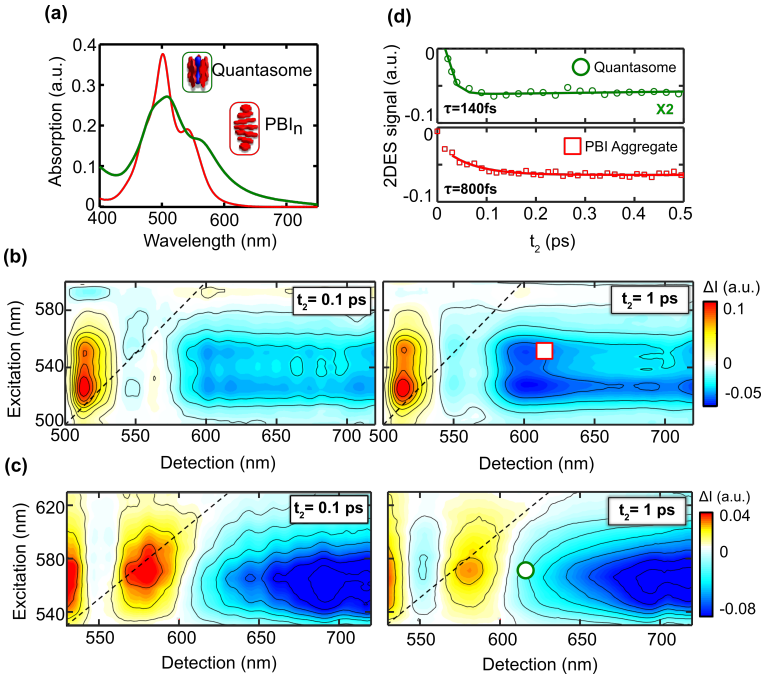

Figure 4.2: (a) steady state absorption spectra of the PBI_n aggregate in water (red) and quantasome (green); (b) pure absorptive 2D spectra of PBI_n at t_2=0.1pa and 1ps; (c)pure absorptive 2D spectra of $[PBI]_5Ru_4POM$ at t_2=0.1pa and 1ps; (d) t_2 traces obtained by exciting at 540nm (PBI_n, red square) and 560nm (quantasome, green circle) and detecting at 620nm. In both plots, the experimental data (symbols) are overlapped with the single trace best fit (continuum lines) from which the raise time is estimated: 140fs for the quantasome and 800fs for the PBI aggregate

from the spectroelectrochemistry (SEC) experiment from which it is possible to identify the spectral features associated with radical cation and anion of the system. On top of the figure 4.3a there is the SEC measurement associated with PBI^+ radical cation (blue curve) and the PBI^- radical anion (red curve) from which we can deduce that the ESA signal in the 2D maps represents the formation of the radical cation in both systems; in particular we show that the quantasome architecture facilitate the formation of the charges in a sub-200fs which is almost four times faster with respect the PBI_n aggregate. From the SEC experiment, we can observe that the peaks associate to the radical anion (PBI^-) are located at larger wavelengths with respect the spectral window covered by the 2DES experiment; specifically they are centered at 730nm, 820nm and 990nm. For this reason we extend the probe spectral region by performing a pump probe experiment by exciting both systems at 520nm and measuring the effects with an ultrabroadband probe pulse from 560nm to 1000nm. Figure 4.3a shows the SEC results combined with the transient absorption (TA) spectra of PBI_n (middle) and quantasome (bottom) systems

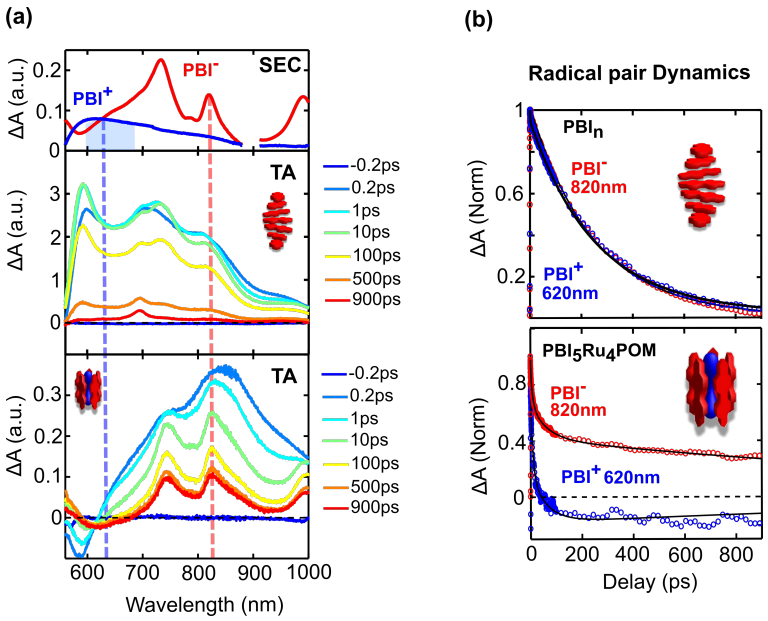

Figure 4.3: (a) on top:spectroelectrochemistry of the PBIs radical cation (blue) and anion (red), middle: transient absorption spectra at delays from -0.2ps to 900ps of the PBI_n aggregate, bottom: transient absorption spectra at delays from -0.2ps to 900ps of the $[PBI]_5Ru_4POM$; (b) dynamics of the PBI^+ (620nm ,blue) and PBI^- (820nm, red) obtained from the PBI_n (on top) and $[PBI]_5Ru_4POM$ (bottom) pump probe experiment. In both plots, the experimental data (symbols) are overlapped with the best fit (black lines) obtained with global analysis

detected at different delays between the pump and probe pulses. The data are expressed as variation of the absorption with and without the excitation of the pump pulse. This representation of the data reproduce ESA signals with positive amplitude by making the charge dynamics more readable. The TA data of the PBI_n structure show a sub-ps formation of the peaks associated with the PBI^+ and PBI^- charges that completely decay in less than 500ps. The TA data obtained from the quantasome system show an ultrafast formation of the charges that is not resolvable with this experiment (pump pulse duration 150fs). We expect this result due to the rise time found with the 2DES data (140fs) where the formation of the charges is comparable with the temporal resolution of the TA experiment. From 0.2ps to 1ps, the TA spectra of the quantasome show a sharpening of the ESA peaks which can indicate a possible localization of the charges. Another aspect that can be noticed is related to the decay of the signal detected at 610nm-700nm (PBI^+) that decays faster with respect the peaks associated with PBI^-. In order to point out these differences, figure 4.3 shows the normalized dynamics of the PBI^+ at 620nm (blue) and PBI^- at 820nm (red) for PBI_n (on top) and quantasome (bottom). In both plots we represent the experimental point (colored symbols) and the best fit (continuum black

lines) obtained with the global analysis algorithm. The radical pairs dynamics for the PBIs aggregate show the same behavior that can be modeled as a sum of two exponential decays: The first lifetime is around 800fs as it was predicted from the 2DES experiment and it corresponds to the formation and localization of the charges. The second lifetime is estimated around 250fs and it correspond to the charge recombination. It is found also a third life time larger than 1ns in which only the PBI monomer spectral signatures survive[10]. Completely different are the dynamics of the radical pairs in the quantasome structure. In particular, the radical cation shows a faster decay that is completed in less than 50ps. The radical anion shows a fast decay similar to the cation that is followed by a non-decaying signal. In the next section, we exploit global analysis algorithm in order to design a deactivation energy level scheme of the quantasome system.

4.1.2. Data analysis and predicted model

In order to temporally characterized all the steps in which the radical pairs in the quantasome structure are involved, we performed global analysis in which the best fit is obtained by using four time constant components. The result of this analysis is typically represented with the DAS as it was made for the 2DES analysis of the natural photosystems. Another representation of the global analysis results can be made via Evolution Associated Spectra (EAS). This method allows to monitor how TA spectrum evolving after each lifetime decays τ_i. Figure 4.4b shows the EAS obtained from the quantasome system where the entire dynamics is described with the following time constants: τ_1=0.8ps, τ_2=8ps, τ_3=60ps and a non-decaying component larger with respect the maximum delay adopted for the measurement (1.5ns). The time constant of 0.8ps describes the temporal evolution from the brown spectrum to the green spectrum. In this case, we can notice a sharpening of the peaks at 730nm, 820nm and 990nm that reflects a localization of the PBI^- charges. The 8ps component reproduce the effects from the green to the violet spectra, in which the broad peak corresponding to the PBI^+ completely decay. Such mechanism is connected to the presence of the polyoxometallate that, in polar aqueous environment, induces an efficient hole transfer process, generating Ru_4POM^+ radical cation [64]. The violet and black spectra show a similar shape and the two lifetimes could correspond to a bi-phasic charge recombination probably due to the varying degree of coupling within the charges. From the amplitude of the DAS, it is possible to extrapolate the percentage of the charges involved in the two recombination processes. The time constant τ_3=60ps is associated with 36% and the fourth time constant to the 64 % by making the last lifetime dominant in order to describe the charge recombination mechanism. Figure 4.4a shows a temporal comparison of the different processes that are taking place in PBI_n and quanta-

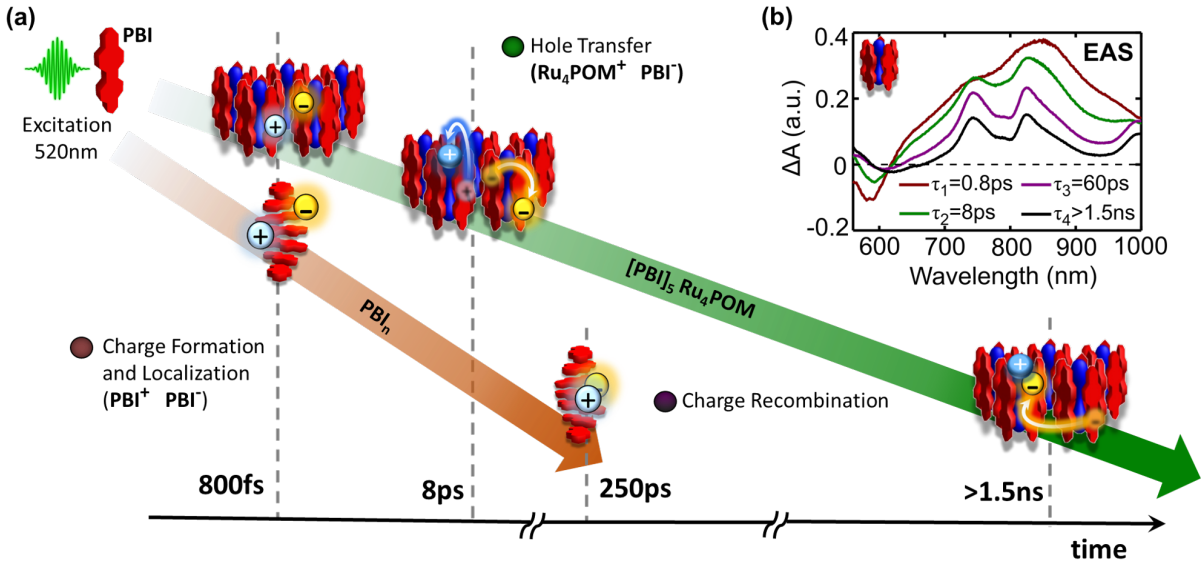

Figure 4.4: (a) predicted model for the PBI_n and quantasome systems based on the global analysis. The PBI_n aggregate is characterized by two steps: charge formation in 800fs and the charge recombination in 250ps. The results for the $[PBI]_5Ru_4POM$ are expressed in panel (b) by using evolution associated spectra; in particular, the systems evolves with four time constant: τ_1=800fs (fromation and localization of the charges), τ_2=8ps (hole transfer process), τ_3=60ps and τ_4 >1.5ns represent a bi-phasic charge recombination where the longer one dominate with respect the other

some systems. The dynamics of the PBIs units is characterized by two steps; the first one is the formation of the charges (800fs) and the second one is the charge recombination (250fs). In the quantasome system, there is an ultrafast formation and delocalization of the charges in 140fs estimated from the 2DES experiment, followed by a charge localization in 800fs. Here we have an intermediate step corresponding to the hole transfer in which the radical pair Ru_4POM^+ and PBI^- is created. Such charge separation state present a long life time which is larger than 1.5ns. In summary, by comparing the results obtained from PBI_n aggregate and artificial quantsome, we found that $[PBI]_5Ru_4POM$ facilitate the charge transfer and separation process and the charge recombination time is increasing up to ns time scale. These results confirm that the artificial quantsome structure presented in this work is a good candidate for mimic the water oxidation process in natural light harvesting.

4.2. Long-Range Energy Transfer in Organic Microcavities

The possibility to have energy transfer between a donor and an acceptor molecular system is dictated by the absorption spectra of the molecules and the distance between them. In particular, according to the Förster theory, the maximum distance that allow this mechanism is around tens nm. Such a distance is very similar to the one between chromophores in natural light harvesting systems, where the EET process is very efficient. This evidence can represent a limit for natural photosystems and in this section we show a donor/acceptor structure that allows to overcome this aspect. In this view, Georgiou and coworkers [12], observed that EET between two spatially separated molecules is possible if they are confined in a cavity that works in strong coupling regime. Such a particular coupling manifests when excitonic states of the donor and acceptor molecules are coupled with the same cavity mode by creating new hybrid states called polaritons[65]. In this particular case, Even if the distance between the molecules is larger than the typical Förster radius, it was observed that polaritons can assist donor/acceptor EET process. Unfortunately a complete spectral and temporal characterization of this process still missing. In this chapter, we exploit 2DES technique in order to investigate the EET process in a organic microcavity comprised of a donor and an acceptor molecules that are distanced by 2 μm.

4.2.1. 2DES of spatially separated molecules

Before to explore the effects of the strong coupling in an optical microcavity, we first investigate via 2DES experiment, what happen when a donor an an acceptor molecules are spatially separated outside of the cavity. We use two j-aggregate semiconductors dyes named TDBC (donor) and NK2707 (acceptor) that are separated by $2\mu m$ optically transparent polymer polystyrene (figure 4.5a). The details of the sample preparation are reported in reference[12] and the experimental parameters in appendix A. Figure 4.5b shows the steady state absorption of the system reported in panel a where it is possible to recognize two different absorption peaks at 580nm and 630nm. The first one is associated with the TDBC exciton state and the second one to the NK2707. The chemical structure of both molecules is reported in the same plot on top. In order to understand the processes in this system, we first performed 2DES experiment on the single dyes deposited on the 500μm quartz-coated glass substrate. Figure 4.5d shows the pure absorptive 2D maps of TDBC film at t_2=25fs and 100fs where it is possible to distinguish GSB signal along the diagonal line and a blue shifted ESA signal. At these two delays, we can observe

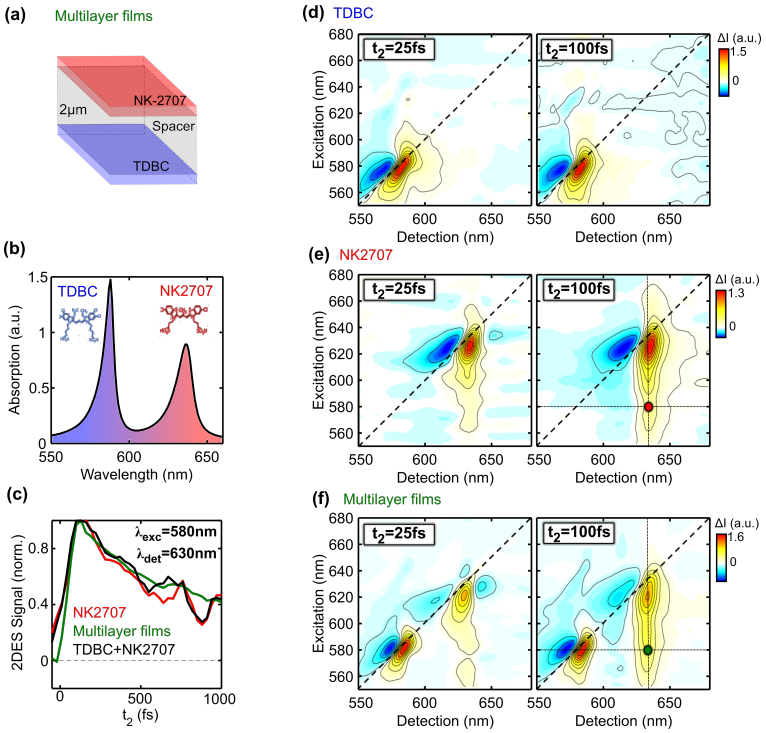

Figure 4.5: (a) scheme of the multilayer film comprised of TDBC/2μm polystyrene spacer/NK2707; (b) steady state absorption spectrum of the multilayer films reported in panel (a) with the TDBC (blue) and NK2707 (red) molecular structure; (d,e,f) pure absorptive 2D spectra at t_2=25fs and 100fs of TDBC (d), NK2707 (e) and the multilayer films (f); (c) t_2 trace of the 580nm/630nm excitation/detection point obtained from 2DES data of NK2707 (red), multilayer films (green) and the sum of the TDBC and NK2707 single dyes 2DES data

no significant variation of the signal and no cross peaks formation. Figure 4.5e shows the 2D spectra of NK2707 single dye at the same delays as for TDBC. Also in this case, we can observe the excitonic feature along the diagonal line as GSB signal and the related blue shifted ESA signal. The main difference is the presence of a cross peak at the 590nm/630nm excitation/detection wavelength that is probably due to an internal relaxation from higher to lower energy states. We now compare these results with the one obtained from the multilayer films (panel a). Figure 4.5f shows the pure absorptive 2D spectra of the multilayer films at t_2=25fs and 100fs. In the first 2D map we can clearly distinguish the excitons peaks of both dyes along the diagonal line accompanied with ESA signals. At t_2=100fs we can observe a formation of a cross peaks as it was observed for the 2D maps of the NK2707. In order to understand the origin of this cross peak, we study the dynamics of this point in all the systems. Figure 4.5c shows the dynamics at 580nm/630nm excitation/detection wavelength of the NK2707 (red), 2μm spaced films (green) and the data obtained by summing the dynamics obtained from the NK2707 and

TDBC single dye 2DES (black line). By normalizing the t_2 traces, we can observe similar trend which suggest that 2DES results obtained from the multilayer films correspond to the one obtained by the sum of the single semiconductors. This allows to affirm that no energy transfer between TDBC and NK2707 molecules is present when they are distanced by 2μm. This evidence is also confirmed by the previous photoluminescence excitation measurement performed on the same system [12]. In the next section, we will study the same structure when it is confined in a optical microcavity in order to characterize a possible EET processes between the two molecules.

4.2.2. Organic Microcavity

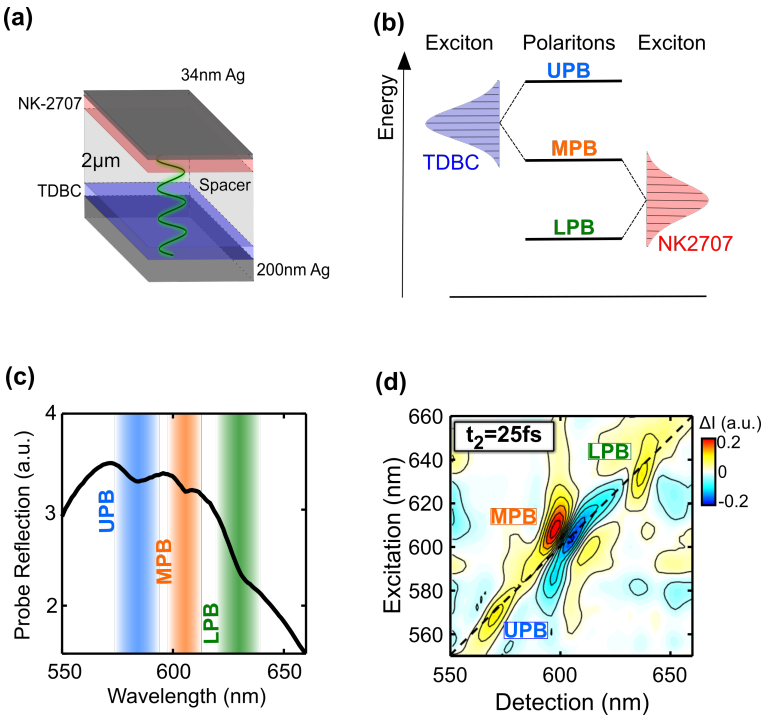

Figure 4.6: (a) scheme of the organic microcavity used in this study; (b) Energy level scheme under strong coupling regime where the coupling of the molecular excitonic states with a cavity mode, generates hybrid polaritons states called Upper Polariton Branch (UPB), Middle Polariton Branch (MPB) and Lower Polariton Branch (LPB); (c) white light reflection from the cavity where the holes identify UPB (blue), MPB (orange) and LPB (green) states; (b) 2D spectrum of the cavity at t_2=25fs where each diagonal peak is labeled with the corresponding polariton state

The scheme of the TDBC-NK2707 microcavity is shown in figure 4.6a where the spacer is the same adopted for the multilayer films and the optical confinement of the molecules is obtained by putting at the edge two Ag mirrors with 200nm and 34nm thickness.

Recent photoluminescence experiments on the same cavity, demonstrate the formation of the polaritons state and, consequently, the formation of a strong coupling between the molecules and the mode of the cavity [12]. Such a coupling promotes new hybrid-polariton states with higher and lower energies with respect the molecular excitonic states. Figure 4.6b shows an example of the energy level scheme in this regime where the coupling between both exciton states and the same cavity mode produces three polariton states named upper polariton branch (UPB) energetically higher with respect the donor exciton, lower polariton branch (LPB) energetically lower with respect the acceptor exciton and an energetic intermediate state called middle polariton branch (MPB). The formation of these new states is also confirmed experimentally by observing the with light reflection from the cavity reported in figure 4.6c or the angular dispersion reported by Georgiou and coworkers [12]. Specifically, figure 4.6c shows the spectra of the cavity reflection beam when the sample is tilted by an angle of 10^o. In the spectral range from 550nm to 660nm, the spectrum shows three holes in the probe in which the reflectivity of the cavity decreases. Such points correspond to the polariton-spectral position at 570nm (UPB), 605nm (MPB) and 640nm (LPB). We performed 2DES experiment on the organic microcavity by collecting at the detector the probe reflected beam. The details related to the experiments and the sample are reported in the appendix A. Figure 4.6d shows the pure absorptive 2D spectrum of the organic microcavity at t_2=25fs where it is possible to identify three peaks along the diagonal line that reflect the spectral position of the polariton states. We can notice that each peak has a derivative lineshape causes by the variation of the refractive index with and without the pump pulse excitation as it was observed in the recent pump probe experiments performed on different donor/acceptor microcavities [66].

4.2.3. 2DES results and analysis

In order to understand the different mechanisms collected by the 2DES experiment, we observe the dynamics of signals associated with the polaritons state when the excitons reservoirs or the UPB state are excited. Because the derivative lineshape imposes a double sign amplitude for each peak, the t_2 traces analyzed here for each diagonal and cross peaks are related only to the positive part of the spectra. We start our analysis by looking at the dynamics when the exciton reservoirs of the TDBC (peaked at 580nm) and NK2707 (peaked at 630nm) are excited. Figure 4.7a shows the 2D map at t_2=100fs where the horizontal continuum and dashed black lines identified the 580nm and 630 nm excitation wavelength and the detection axis is grid based on the spectral position of the UPB (570nm), MPB (605nm) and LPB (640nm) peaks. Figure 4.7c shows the t_2 traces of the

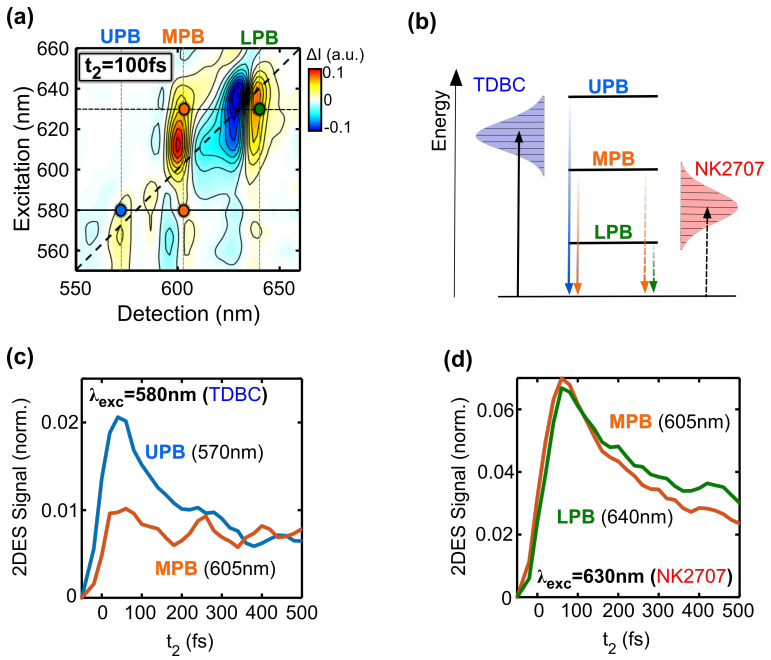

Figure 4.7: (a) 2D spectrum of the cavity at t_2=100fs where the excitation axis is grid based on the position of the TDBC (580nm) and NK2707 (630nm) exciton pekes and the detection axis is grid based on the position of the polariton states; (b) Deactivation energy level scheme where the continuum (dashed) black arrows correspond to the excitation of the TDBC (NK2707) exciton and the blue, orange and green arrows represent the emission from the UPB, MPB and LPB states; (c) t_2 traces obtained by exciting at 580nm and detecting at 570nm (blue) and 605nm (orange); (d) t_2 traces obtained by exciting at 630nm and detecting at 605nm (orange) and 640nm (green)

UPB state (blue) and the MPB state (orange) after the excitation of the TDBC exciton. Both dynamics show an instantaneous formation due to the strong coupling with the optical cavity mode, but the decay looks different. In particular, the MPB signal decays slower with respect to the UPB states. This effect could be correlated to a possible EET process from UPB to the MPB through the scattering in the exciton reservoir. Figure 4.7d shows the temporal evolution of the MPB (orange) and LPB (green) states after the excitation of the NK2707 exciton. Also in this case the signals of both polaritons rise instantaneously probably due to the strong coupling regime of the cavity. The data differ in the decay component; specifically, the MPB decays faster with respect the LPB state. All of these results are reported in the energy level scheme in figure 4.7b where the continuum lines are related to the processes obtained by exciting the TDBC exciton state and the dashed lines indicate processes after the excitation of the NK2707 exciton. The analysis proceed by evaluating the temporal evolution of the polariton states when the UPB state is excited. Figure 4.8a shows the pure absorptive 2D map at t_2=200fs where the horizon-

tal line indicates the spectrum obtained by exciting the system at 570nm (UPB) and the detection axis is grid based on the position of the polariton states. The crossing points between these lines are emphasized with colored circles which correspond to the following excitation/detection wavelength points: 570nm/570nm (UPB/UPB), 570nm/605nm (UPB/MPB) and 570nm/640nm (UPB/LPB). Figure 4.8b shows the temporal evolution

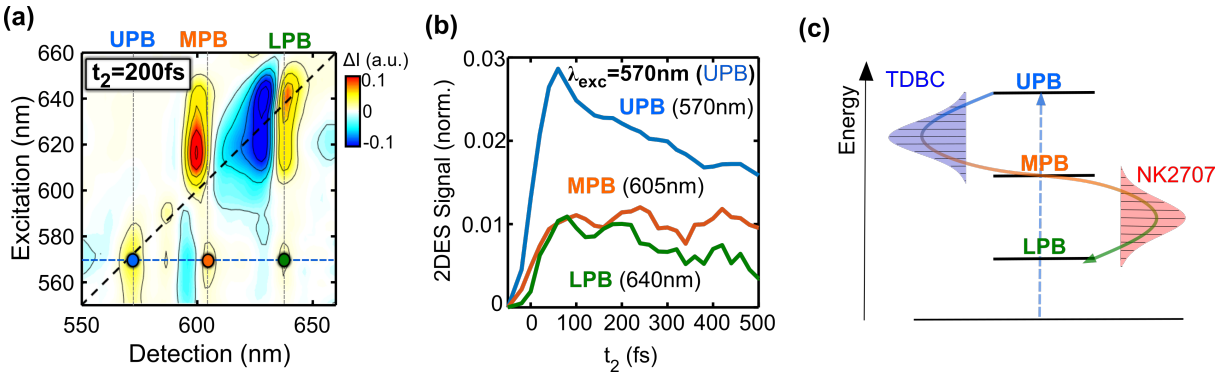

Figure 4.8: (a) 2D map at t_2=200fs where the horizontal line correspond to the excitation at 570nm and the detection axis is grid based on the position of the polaritons states; (b) t_2 traces obtained by exciting at 570nm and detecting at 570nm (blue), 605nm (orange) and 640nm (green); (c) Energy level scheme where the dashed blue arrow indicates the excitation of the UPB state and the continuum arrow represent the connection between exciton and polariton that provides an ultrafast emission from the MPB and LPB states.

of the diagonal and cross peaks marked in the panel a. The dynamic of the diagonal peak associated with the UPB state (blue) shows an instantaneous formation followed by two exponential decays; the first one is ultrafast (sub-100fs) and the second one is long-lived. The cross peaks that correspond to the emission from the MPB (orange) and LPB (green) states are composed of an ultrafast rise that is comparable with the first decay of the UPB diagonal peak and a long-lived signal that decay slower with respect the second UPB decay. The excitation at 570nm induces a population in the high energy absorption tail of the TDBC exciton reservoir. Such a population relaxes through the reservoir by populating the MPB state. This process is connected to the first decay and ultrafast rise of the UPB and MPB states dynamics respectively. Once the MPB state is populated, the strong coupling regime induces a population also in the NK2707 exciton reservoir. Such mechanism explain the rise time of the LPB state that is simultaneous with the rise of the MPB state. Figure 4.8c shows the energy level scheme in which the relaxation process discussed before is represented with an arrow that cross each polariton states passing through the exciton reservoirs of the molecules. From this result we can observe that once the UPB state is excited, the microcavity provides an almost instantaneous emission from all the other polariton states. This effect does not correspond to a classical

EET process from an higher to a lower excited state as was observed for the bulk and red forms Chls in natural light harvesting systems where the complete decay of one specie is followed by a population of the other specie. Here, the excitation of the higher energy level produces a direct emission of all the others states. This behavior suggests that the formation of the polaritons states provides a connection between the molecules via the MPB state. The entire cavity, from this point of view, behaves as a collective state where the molecules are coupled to each other. In summary, we observe a long-range energy connection between two spatially separated molecule that is assisted by the formation of hybrid polariton states.

5 | Conclusions

In this thesis we point out the power of two-dimensional electronic spectroscopy (2DES) technique to reveals different characteristics and processes of a specific sample. In the first chapter we explore the theoretical architecture to derive the 2DES response function of a generic system by giving a graphical representation with Bloch vectors and double-sided Feynman diagrams. Such methods allow to easily identify the different interaction optical pathways and the processes that are taking place in the system. The passage from the theory to the experimental apparatus is not trivial due to the several precautions regarding laser pulses duration, phase stability and mechanical delay control that must be satisfy. The 2DES setup adopted in this work used pump-probe geometry configuration where the first and the second pulses (pump) are collinear. The signal emitted from the sample is collected along the same propagation direction of the third pulse (probe). In all the experiments presented in this work, the pump and probe pulses are degenerate and they are created by a non collinear optical parametric amplifier (NOPA) with 200nm bandwidth and temporally compressed up to 15fs. The phase stability and the delay between the pump pulses is obtained by adopting the TWINS; a device based on two pairs of non liner birefringent wedges that allow a minimum temporal shift of tens attoseconds. Such apparatus, allow to directly detect the so called time-resolved pure absorptive 2D spectra as a function of excitation, detection wavelengths and pump probe delay. In order to understand the meaning of positive and negative signals and which information can be retrieved from this experiment, in the second chapter we have shown the analysis of 2D maps of three different molecules: Perylene Bisimide (PBI), free base Poprhyrin and Lumogen F-Orange (LFO).

The PBI molecule is studied by combining the 2DES experiment and the calculation results. In particular, the perfect match obtained in this case, allow to distinguish between Ground state bleaching (GSB), stimulated emission (SE) and excited state absorption (ESA) signals that are overlapped to each other in the pure absorptive maps. This molecules is particularly suited for this purpose due to the simple molecular structure and the long-lives signals associated to the energy states.

Completely different is the structure of the free base porphyrin where ultrafast processes

between different energy bands can be detected. In this case, we show how it is possible recognized excitation energy transfer (EET) mechanisms between two energy states by looking the position of the peaks in the 2D spectra. The diagonal peaks reflect the steady state absorption spectrum and the peaks out of the diagonal (cross peaks) can represent a coupling between states (instantaneous signal) or EET process (delayed signal). In this particular case, poprhyrin is characterized by an higher energy band called Q_y and a lower one called Q_x. Our 2DES results demonstrate the ultrafast EET from Q_y to Q_x band by showing a sub-100fs rise of the cross peak by exciting Q_y and detecting Q_x. The analysis can be extend by studying the frequency of the oscillatory signals emitted from the system. Such kind of analysis required the generation of the 2D oscillatory spectra obtained by Fourier transforming the 2DES signals with respect the temporal axis. The new frequency axis is called ν_2 and for a fixed value, the corresponding 2D oscillatory map will show the combination of excitation and detection wavelength from which the mode ν_2 appears. This analysis was also supported by calculation from which it is possible to predict the deactivation energy level scheme.

Another aspect that can be analyzed by exploiting 2DES technique is the estimation of the dephasing time and the spectral diffusion; specifically, such characteristics of the sample can be derived from the 2D lineshapes of the absorption peaks. In order to show this, we performed lineshape analysis on the LFO dye which structure and absorption spectrum looks similar to the PBI molecule. The depahsing time can be estimated as the inverse of the homogeneous broadening linewidth which can be extrapolated from the 2D spectra at delays close to zero. In this case, the lineshape of the GSB peak looks elliptical where the larger diameter (diagonal direction) represents the inhomogeneous broadening and the shorter diameter (cross diagonal direction)represents the homoheneous broadening. Here we propose a lineshape model function that exploit perturbation theory and Bloch equation in order to reproduce 2D lineshape as a function of the two kind of broadening. From the best fit results, we obtained the homogeneous linewidth from which we recover the estimated dephasing time. We repeat this procedure at different temperature by finding that the dephasing time linearly decreases from T_2=94fs (at 86K) to 53fs (at 295K). The spectral diffusion effect can be described by studying the temporal evolution of the lineshape. Here we adopted the central line slope method (CLS) from which it is possible to quantify the orientation of the peaks with an angular coefficient term β. Specifically, for β=1 the lineshape is elliptical and for β=0 the lineshape is circular. In last case, the diagonal and anti-diagonal linewidth are indistinguishable due to the interaction between the system and the environment by loosing the information of the initial state. The time from which β decrease from 1 to 0, characterized the spectral diffusion mechanism. Our results shows that such time is correlated to the temporal resolution of the experiment,

the dephsing time and the mode of the molecule.
Although all of these studies are applied on samples composed by single molecules, same analysis and processes can be observed in heterogeneous systems. In particular, 2DES technique is suited in order to study light harvesting system where efficient energy conversion processes take place.

5.1. Natural Light Harvesting Systems

In the third chapter we explored 2DES technique to investigate the EET processes in natural light harvesting system by focusing on the role of a group of Chlropylls (Chls) denoted red forms that absorb at lower energy with respect the primary donor of the reaction center (RC). For this reason, we first study the photosystem I Light harvesting complex I (PSI-LHCI) isolated from spinach (higher plants) that shows the highest quantum conversion efficiency (>98%) known in nature. The analysis is conducted on the sample under open and closed RCs and the temporal characterization of the EET processes is obtained by performing global analysis on the 2DES data. Our results show in both cases a sub-10ps energy equlibration between high energy Chls usually labeled as bulk and Chls RF. Such mechanisms include also an unfavorable sub-ps uphill EET from Chls RF to Chls bulk that does not affect the entire efficiency of the system. The results obtained from the open RCs system allow to unambiguously identify the energy trapping process which is almost doubled faster with respect the relaxation of Chls bulk found for the closed systems (12ps and 22ps respectively). The relaxation time of the Chls RF was estimated around 78ps from the Closed RCs system and 56 ps for the Open RCs system. This discrepancy is due to the presence of the long-lived signal associated with the primary donor of the RC that does not allow a good estimation of the relaxation time of Chls RF in the open configuration. These results can give a big contribute in order to understand the main mechanism of energy conversion in higher plants due to the presence of low-energy Chls.
In order to explore other effects imposed by this Chls, we performed the same study on the PSI-core of a cyanobacteria organism isolated from Spirulina Platensis. Such system is commonly known in literature as the organism that shows the highest concentration of Chls RF and it is usually reported in the trimeric and monomeric form. In this thesis we present the results of both forms obtained by applying the same exponential sequence model for the global analysis algorithm. The lifestimes obtained from this analysis show an ultrafast equilibration process between Chls RF and Chls bulk which is five times faster in the trimer with respect the monomer (100fs and 520fs respectively). This discrepancy suggest that the trimeric form configuration facilitate the EET processes within Chls.

This aspect is also confirmed by the estimation of the downhill EET from Chls bulk to Chls RF which is 2ps for the trimer and 5.4ps for the monomer. The relaxation times of the Chls bulk and RF are similar in both systems: sub-10ps for Chls bulk and 30-40ps for Chls RF. From the results obtained from both higher plants and cynaobacteria organisms we observe and characterized for the first time the uphill EET from Chls RF to Chls bulk which is faster in the cyanobacteria due to the larger amount of low-Chls in the photosystesm. Even if these Chls are located exclusively in the peripheral part for higher plants and in the core for cyanobacteria, the presence of the ultrafast equilibration energy mechanism of Chls RF in both organisms, demonstrate that this effect does not depend on the position of the Chls with respect the RC, but only on the their energy states. In conclusion, these results present a complete characterization of the ultrafast processes in which Chls RF are involved and represent a further steps in order to understand the balance between increasing the absorption bandwidth of the antenna with low-energy Chls and the quantum conversion efficiency.

5.2. Bio-inspired Light Harvesting Systems

The architecture of the natural photosystems open up new branches of study based on renewable energy; in particular the possibility to synthesized innovative devices inspired by the natural one. In this view, we study two different bio-inspired systems in order to optimize some aspects that are unfavorable in the natural light harvesting systems. One of these aspect is connected to the charge recombination time (typically in the order of hundreds ps) that drastically reduce the effective fuel exposed by the reaction center. In order to overcome this aspect, we study an artificial photosystem comprised of a PBIs as self-assembled antenna and a ruthenium - polyoxometalate organized as catalytic cofactor with the following stoichiometry formula $[PBI]_5Ru_4POM$. By combining 2DES and pump probe experiments we characterized the time evolution of the PBI^+ and PBI^- radical pairs. Our results point out that the presence of the POM in a polar environment facilitates the formation of the radical pairs and promotes an ultrafast hole transfer by creating Ru_4POM^+ and PBI^- charge pairs. The charge recombination time for this new radical pairs is predicted larger than 1.5ns (limited by the time window adopted for the experiments). These results represent a starting point in order to engineer artificial photosysnthesis.

The second aspect that can be optimized in the natural photosystems id related to the molecular distance in which EET process can take place. In particular, such a distance is identify by the typical Förster radius (10nm) which is comparable with spatial Chls separation. In general, this concept is valid for all the system in which there is an EET between

a donor and acceptor molecules. Recent studies propose a solution in order to increase the EET distance range by confined the donor and acceptor molecules in a microcavity that work in strong coupling regime. In this thesis we investigate such mechanisms in a microcavity composed of two j-aggregate semiconductors dyes named TDBC and NK2707 spatially separated by 2μm optically transparent polystyrene spacer. 2DES experiment point out the formation of three hybrid-polarton states generated by the strong coupling between excitonic states of the molecules with the same cavity mode. Such new states are called upper polariton branch (UPB), middle polariton branch (MPB) and lower polariton branch (LPB). By exciting the excitons reservoir of both molecules, we observe an istantaneous formation of the polarton states which remarks the coupling mechanism. By exciting the UPB, energetically higher with respect the donor exciton, we observe an ultrafast formation of the MPB (intermidiate state between the donor/acceptor excitons) and LPB (energetically lower than the acceptor exciton). These results reveal an energetic connection between the two molecules assisted by polariton states. Such connection provide an ultrafast energy migration from one molecule to the other.
In conclusion, we study two different artificial architecture that can be exploit to develop innovative devices for lighting and light-harvesting applications in which chemical reactions can be controlled through alteration of material's photophysical functionalities by strong coupling.

5.3. Future perspectives

The results obtained from are relevant in chemistry and biology: for instance, the role of low-energy Chls have key implication for the light harvesting mechanism and its biological function. In particular they increase the light harvesting capacity of the systems by increasing the absorption band and the uphill EET mechanism pointed out in this work demonstrate that they participate in the photosynthesis process. Nevertheless, some aspect related to their role in the reaction center in different organisms are still an open point.
From the chemistry point of view, these results represents a starting point in order to design bio-inspired artificial photosystems. The goal will be to develop innovative devices that allow to efficiently perform for instance oxidation and reduction of the water. In this view. the concept of a quantasome architecture represents a disruptive approach for the realization of alternatives design inspired by the functioning of the photosynthetic complex.Finally, the last result discussed on this thesis proposes strong light-matter interactions to control the energy at the nanoscale: the formation of polariton states under strong coupling regime in microcavitiieis can enable and enhance the control of EET

processes and chemical reactions.

Bibliography

[1] B.-J. Ng; L. K. Putri; X. Y. Kong; Y. W. Teh; P. Pasbakhsh; S.-P. Chai. Z-scheme photocatalytic systems for solar water splitting. *Adv. Sci.*, 7:1903171, 2020.

[2] R. Croce; H. van Amerongen. Light-harvesting in photosystem i. *Photosynth. Res.*, 116:153–166, 2013.

[3] N. Nelson; W. Junge. Structure and energy transfer in photosystems of oxygenic photosynthesis. *Annu. Rev. Biochem.*, 84:659–683, 2015.

[4] S. Caffarri; T. Tibiletti; R.C. Jennings; S. Santabarbara. A comparison between plant photosystem i and photosystem ii architecture and functioning. *Curr. Protein. Pept. Sci.*, 15:296–331, 2014.

[5] M. Russo; A. P. Casazza; G. Cerullo; S. Santabarbara; M. Maiuri. Direct evidence for excitation energy transfer limitations imposed by low-energy chlorophylls in photosystem ilight harvesting complex i of land plants. *J. Phys. Chem. B*, 125:3566–3573, 2021.

[6] P. Akhtar; C. Zhang; Z. Liu; H. S.Tan; P. H. Lambrev. Excitation transfer and trapping kinetics in plant photosystem i probed by two-dimensional electronic spectroscopy. *Photosynth. Res.*, 135:239–250, 2018.

[7] E. Wientjes; R. Croce. The light-harvesting complexes of higherplant photosystem i: Lhca1/4 and lhca2/3 form two red-emitting heterodimers. *Biochem. J.*, 433:477–486, 2011.

[8] Y. Mazor; A. Borovikova; N. Nelson. The structure of plant photosysthem i supercomplex at 2.8 å resolution. *eLife*, 4:e7433, 2015.

[9] E.-M. Aro; I.Virgin; B. Andersson. Photoinhibition of photosystem ii. inactivation, protein damage and turnover. *Biochim. Biophys. Acta*, 1143:113–134, 1993.

[10] M. Bonchio; Z. Syrgiannis; M. Burian; N. Marino; E. Pizzolato; K. Dirian; F. Rigodanza; G. A. Volpato; G. La Ganga; N. Demitri; S. Berardi; H. Amenitsch; D. M. Guldi; S. Caramori; C. A. Bignozzi; A. Sartorel; M. Prato. Hierarchical organization

of perylene bisimides and polyoxometalates for photo-assisted water oxidation. *Nat. Chem.*, 11:146–153, 2019.

[11] D. G. Lidzey; D. D. C. Bradley; A. Armitage; S. Walker; M. S. Skolnick. Photon-mediated hybridization of frenkel excitons in organic semiconductor microcavities. *Science*, 288:1620–1623, 2000.

[12] K. Georgiou; R. Jayaprakash; A. Othonos; D. G. Lidzey. Ultralong-range polariton-assisted energy transfer in organic microcavities. *Angew. Chem. Int. Ed.*, 60:2–9, 2021.

[13] A. M. Weiner. *Ultrafast Optics*. Jhon Wiley & Sons Inc Publication, 2009.

[14] M. Zavelani; G. Cerullo; S. De Silvestri; L. Gallmann; N. Matuschek; G. Steinmeyer; U. Keller; G. Angelow; V. Scheuer; T. Tschudi. Pulse compression over a 170-thz bandwidth in the visible by use of only chirped mirrors. *Optics Letters*, 26:1155–1157, 2001.

[15] Ahmed H. Zewail. Femtochemistry. *J. Phys. Chem. A*, 104:5660–5694, 2000.

[16] M. Cho; T. Brixner; I. Stiopkin; H. Vaswani; G.R. Flaming. Two-dimensional electronic spectroscopy of molecular complexes. *J. Chin. Chem. Soc.*, 53, 2006.

[17] G. S. Schlau-Cohen; T. R. Calhoun; N. S. Ginsberg; E. L. Read; M. Ballottari; R. Bassi; R. van Grondelle; G. R. Fleming. Pathways of energy ow in lhcii from two-dimensional electronic spectroscopy. *J. Phys. Chem. B*, 113:15352–15363, 2009.

[18] E. E. Ostroumov; R. M. Mulvaney; J. M. Anna; R. J. Cogdell; G. D. Scholes. Energy transfer pathways in light-harvesting complexes of purple bacteria as revealed by global kinetic analysis of two-dimensional transient spectra. *J. Phys. Chem. B*, 117:11349–62, 2013.

[19] F. V. A. Camargo; Y. Ben-Shahar; T. Nagahara; Y. E. Panfil; M. Russo; U. Banin; G. Cerullo. Visualizing ultrafast electron transfer processes in semiconductor metal hybrid nanoparticles: Toward excitonicplasmonic light harvesting. *Nano Lett.*, 21:1461–1468, 2021.

[20] V. R. Policht; M. Russo; F. Liu; C. Trovatello; M. Maiuri; Y. Bai; X. Zhu; S. Dal Conte; G. Cerullo. Dissecting interlayer hole and electron transfer in transition metal dichalcogenide heterostructures via two-dimensional electronic spectroscopy. *Nano Lett.*, 21:4738–4743, 2021.

[21] A. Nemeth; F. Milota; J. Sperling; D. Abramavicius; S. Mukamel; H. F. Kauffmann.

Tracing exciton dynamics in molecular nanotubes with 2d electronic spectroscopy. *Chemical Physics Letters*, 469:130, 2009.

[22] C. N. Borca; T. H. Zhang; X. Q. Li; S. T. Cundiff. Optical two-dimensional fourier transform spectroscopy of semiconductors. *Chemical Physics Letters*, 416:311, 2005.

[23] R. Mitric; T. Brixner C. Lambert; F. Koch; S. F. Völker; A. Schmiedel; M. Holzapfel; A. Humeniuk; M. I S Röh;. Energy transfer between squaraine polymer sections: From helix to zigzag and all the way back. *Journal of the American Chemical Society*, 137:7851–7861, 2015.

[24] T. Mančal; A. Nemeth; F. Milota; V. Lukeš; H. F. Kauffmann; J. Sperling. Vibrational wave packet induced oscillations in two-dimensional electronic spectra. *J. Chem. Phys.*, 132:184515, 2010.

[25] P. Hamm and M. Zanni. *Concepts and methods of 2D infrared spectroscopy.* Cambridge University Press, 2011.

[26] Andrei Tokmakoff. Two-dimensional line shapes derived from coherent third-order nonlinear spectroscopy. *J. Phys. Chem. A*, 104:4247–4255, 2000.

[27] Sean T. Roberts; Joseph J. Loparo and Andrei Tokmakoff. Characterization of spectral diffusion from two-dimensional line shapes. *J. Chem. Phys.*, 125(084502):1–8, 2006.

[28] Shaul Mukamel. *Principles of nonlinear optical spectroscopy.* Oxford University Press, 1995.

[29] F. D. Fuller; J. P. Ogilvie. Experimental implementations of two-dimensional fourier transform electronic spectroscopy. *Annu. Rev. Phys. Chem.*, 66:667–90, 2015.

[30] M.L. Cowan; J.P. Ogilvie; R.J.D. Miller. Two-dimensional spectroscopy using diffractive optics based phased-locked photon echoes. *Chem. Phys. Lett.*, 386:184, 2004.

[31] J. Rehault; M. Maiuri; A. Oriana; G. Cerullo. Two-dimensional electronic spectroscopy with birefringent wedges. *Rev. Sci. Instrum.*, 85(123107):1–10, 2014.

[32] Sang-Hee Shim and Martin T. Zanni. How to turn your pump–probe instrument into a multidimensional spectrometer: 2d ir and vis spectroscopies via pulse shaping. *Phys. Chem. Chem. Phys.*, 11:748–761, 2009.

[33] D.M. Jonas. Two-dimensional femtosecond spectroscopy. *Annu. Rev. Phys. Chem.*, 54:425–63, 2003.

[34] D. Brida; C. Manzoni; G. Cerullo. Phase-locked pulses for two-dimensional spectroscopy by a birefringent delay line. *Optics Letters*, 37:3027–3029, 2012.

[35] L. Lepetit; M. Joffre. Two-dimensional nonlinear optics using fourier-transform spectral interferometry. *Opt. Lett.*, 21:564–66, 1996.

[36] J. D. Hybl; A. W. Albrecht; S. M. G. Faeder; D. M. Jonas. Two-dimensional electronic spectroscopy. *Chem. Phys. Lett.*, 297:307–13, 1998.

[37] P. F. Tian; D. Keusters; Y. Suzaki; W. S.Warren. Femtosecond phase-coherent two-dimensional spectroscopy. *Science*, 300:1553–55, 2003.

[38] C. Manzoni; G. Cerullo. Design criteria for ultrafast optical parametric amplifiers. *J. Opt.*, 18:103501, 2016.

[39] J. Helbing; P. Hamm. Compact implementation of fourier transform two-dimensional ir spectroscopy without phase ambiguity. *J. Opt. Soc. Am.*, 28:171–178, 2011.

[40] L. Moretti; B. Kudisch; Y. Terazono; A. L. Moore; T. A. Moore; D. Gust; G. Cerullo; G. D. Scholes; M. Maiuri. Ultrafast dynamics of nonrigid zinc-porphyrin arrays mimicking the photosynthetic "special pair". *J. Phys. Chem. Lett.*, 11:3443–3450, 2020.

[41] F. Würthner; C. R. Saha-Möller; B. Fimmel; S. Ogi; P. Leowanawat; D. Schmidt. Perylene bisimide dye assemblies as archetype functional supramolecular materials. *Chem. Rev.*, 116:962–1052, 2015.

[42] A. Segalina; J. Cerezo; G. Prampolini; F. Santoro; M. Pastore. Accounting for vibronic features through a mixed quantum-classical scheme: Structure, dynamics, and absorption spectra of a perylene diimide dye in solution. *J. Chem. Theory Comput.*, 16:7061–7077, 2020.

[43] J. Segarra-Marti; S. Mukamel; M. Garavelli; A. Nenov; I. Rivalta. *Topics in Current Chemistry Collections*. Springer International Publishing, 2018.

[44] X. Sheng; H. Zhu; K. Yin; J. Chen; J. Wang; C. Wang; J. Shao; F. Chen. Excited-state absorption by linear response time-dependent density functional theory. *J. Phys. Chem. C*, 124:4693–4700, 2020.

[45] F. Segatta; M. Russo; D. R. Nascimento; D. Presti; F. Rigodanza; A. Nenov; A. Bonvicini; A. Arcioni; S. Mukamel; M. Maiuri; L. Muccioli; N. Govind; G. Cerullo; M. Garavelli. In silico ultrafast nonlinear spectroscopy meets experiments: The case of perylene bisimide dye. *J. Chem. Theory Comput.*, 17:7134–7145, 2021.

[46] N. De Mitri; S. Monti; G. Prampolini; V. Barone. Absorption and emission spectra of a flexible dye in solution: A computational time-dependent approach. *J. Chem. Theory Comput.*, 9:4507–4516, 2013.

[47] J. Cerezo; D. Aranda; F. J. Avilia Ferrer; G. Prampolini; F. Santoro. Adiabatic molecular dynamics generalized vertical hessian approach: A mixed quantum classical method to compute electronic spectra of flexible molecules in the condensed phase. *J. Chem. Theory Comput.*, 16:1215–1231, 2020.

[48] L. Mewes; R. A. Ingle; A. A. Haddad; M. Cherguia. Broadband visible two-dimensional spectroscopy of molecular dyes. *J. Chem. Phys.*, 155:034201, 2021.

[49] F. Milota; V. I. Prokhorenko; T. Mancal; H. von Berlepsch; O. Bixner; H. F. Kauffmann; J.Hauer. Vibronic and vibrational coherences in two-dimensional electronic spectra of supramolecular j-aggregates. *J. Phys. Chem. A*, 117:6007–6014, 2013.

[50] S. Koirala; S. Mouri; Y. Miyauchi; K. Matsuda. Homogeneous linewidth broadening and exciton dephasing mechanism in $mote_2$. *Physical Review B*, 93:075411, 2016.

[51] I. Kuznetsova; T. Meier; S. T. Cundiff; P. Thomas. Determination of homogeneous and inhomogeneous broadening in semiconductor nanostructures by two-dimensional fourier-transform optical spectroscopy. *Physical Review B*, 76:153301, 2007.

[52] Mark E. Siemens; Galan Moody; Hebin Li; Alan D. Bristow and Steven T. Cundiff. Resonance lineshapes in two-dimensional fourier transform spectroscopy. *Optics Express*, 18(17):17699–17708, 2010.

[53] L. Guo; C.-A. Chen; Z. Zhang; D. M. Monahan; Y.-H. Leed; G. R. Fleming. Lineshape characterization of excitons in monolayer wsy_2 by two-dimensional electronic spectroscop. *Nanoscale Adv.*, 2:2333, 2020.

[54] C.J. Bardeen; G. Cerullo; C.V. Shank. Temperature-dependent electronic dephasing of molecules in polymers in the range 30 to 300 k. *Chemical Physics Letters*, 280:127–133, 1997.

[55] Frantisek Sanda; Vaclav Perlík; Craig N. Lincoln and Jurgen Hauer. Center line slope analysis in two-dimensional electronic spectroscopy. *J. Phys. Chem. A*, 119:10893–10909, 2015.

[56] Christopher J. Fecko; Joseph J. Loparo; Sean T. Roberts; and A. Tokmakoff. Local hydrogen bonding dynamics and collective reorganization in water: Ultrafast infrared spectroscopy of hod/d_2o. *J. Chem. Phys.*, 122(054506):1–18, 2005.

[57] R. Croce; G. Zucchelli; F.M. Garlaschi; R. Bassi; R. C. Jennings. C. excited state equilibration in the photosystem i-light-harvesting i complex: P700 is almost isoenergetic with its antenna. *Biochemistry*, 35:8572–8579, 1996.

[58] R. C. Jennings; G. Zucchelli; R. Croce; F.M.Garlaschi. The photochemical trapping rate from red spectral states in psilhci is determined by thermal activation of energy transfer to bulk chlorophylls. *Biochim. Biophys. Acta*, 1557:91–98, 2003.

[59] B. Gobets; R. van Grondelle. Energy transfer and trapping in photosystem i. *Biochimica et Biophysica Acta*, 1507:80–99, 2001.

[60] A. Rivadossi; G. Zucchelli; F.M. Garlaschi; R.C. Jennings. The importance of ps i chlorophyll red forms in light-harvesting by leaves. *Photosynth. Res.*, 60:209–215, 1999.

[61] A. Volpato; L. Bolzanello; E. Meneghin; E. Collini. Global analysis of coherence and population dynamics in 2d electronic spectroscopy. *Opt. Express*, 24:24773–24785, 2016.

[62] E. Molotokaite; W. Remelli; A. P. Casazza; G. Zucchelli; D. Polli; G. Cerullo; S. Santabarbara. Trapping dynamics in photosystem i-light harvesting complex i of higher plants is governed by the competition between excited state diffusion from low energy states and photochemical charge separation. *J. Phys. Chem. B*, 121:9816–9830, 2017.

[63] A. Sartorel; M. Bonchio; S. Campagna; F. Scandola. Tetrametallic molecular catalysts for photochemical water oxidation. *Chem. Soc. Rev.*, 42:2262–2280, 2013.

[64] M. Stuckart; K. Y. Monakhov. Polyoxometalates as components of supramolecular assemblies. *Chem. Sci.*, 10:4364–4376, 2019.

[65] D. G. Lidzey; D. D. C. Bradley; M. S. Skolnick; T. Virgili; S. Walker; D. M. Whittaker. Strong exciton–photon coupling in an organic semiconductor microcavity. *Nature*, 395:53–55, 1998.

[66] C. A. DelPo; S.-U.-Z. Khan; K. H. Park; B. Kudisch; B. P. Rand; G. D. Scholes. Polariton decay in donoracceptor cavity systems. *J. Phys. Chem. Lett.*, 12:9774–9782, 2021.

[67] C.R. Cantor; P.R. Schimmel. *Biophysical Chemistry. Part II: Techniques for the study of biological structure and function*. Freeman, 1980.

[68] D.H. Anderson. *Compartmental modeling and tracer kinetics*. Springer, 1983.

[69] J. Eisenfeld; C.C. Ford. A systems-theory approach to the analysis of multiexponential fluorescence decay. *Biophys. J.*, 26:73–84, 1979.

[70] G.H. Golub; C.F. van Loan. *Matrix computations*. Johns Hopkins University Press, 1990.

[71] J.F. Nagle; L.A. Parodi; R.H. Lozier. Procedure for testing kinetic models of the photocycle of bacteriorhodopsin. *Biophys. J.*, 38:161–174, 1982.

[72] F.J. Knorr; J.M. Harris. Resolution of multicomponent fluorescence spectra by an emission wavelength-decay time data matrix. *Anal. Chem*, 53:272–276, 1981.

[73] I. H. M. Van Stokkum; D. S. Larsen; R. Van Grondelle. Global and target analysis of time-resolved spectra. *Biochim. Biophys. Acta Bioenerg.*, 1657:82–104, 2004.

[74] C. Ruckebusch; M. Sliwa; P. Pernot; P. A. de Juan; R. Tauler. Comprehensive data analysis of femtosecond transient absorption spectra: a review. *J. Photochem. Photobiol. C*, 13:1–27, 2012.

[75] K. M. Mullen; I. H. M. Van Stokkum. The variable projection algorithm in time-resolved spectroscopy, microscopy and mass spectrometry applications. *Numer. Algorithms*, 51:319–340, 2009.

A | Experimental details

Samples characteristics and experimental parameters adopted for the measurements

Sample	Conc.	solvent/ substrate	path length	Fluence	Pola.	page
PBI monomer (Solution)	1mM	Acetonitrile	200μm	80μJ/cm^2	$\perp$	55(2.1)
Porphyrin (Solution)	3mM	THF	200μm	44μJ/cm^2	MG	58(2.2)
LFO (solid state)	10% by mass in gelatin	polystyrene	500μm	50μJ/cm^2	$\parallel$	62(2.3)
PSI-LHCI Open (Solution)	0.75 ODcm^{-1}	water	200μm	28μJ/cm^2	$\perp$	71(3.1)
PSI-LHCI Closed (solution)	0.75 ODcm^{-1}	water	200μm	28μJ/cm^2	$\perp$	74(3.1)
PSI-Core Trimer (solution)	0.75 ODcm^{-1}	water	200μm	28μJ/cm^2	$\perp$	77(3.2)
PSI-Core Monomer (solution)	0.75 ODcm^{-1}	water	200μm	28μJ/cm^2	$\perp$	80(3.2)
PBI$_n$ aggregate (2DES)	0.4 mM	water	200μm	80μJ/cm^2	$\perp$	86(4.1)

Sample	Conc.	solvent/ substrate	path length	Fluence	Pola.	page
$[PBI]_5Ru_4POM$ (2DES)	0.25 mM	water	200μm	80μJ/cm^2	$\perp$	86(4.1)
PBI_n aggregate (TA)	0.4 mM	water	1mm	120μJ/cm^2	MG	87(4.1)
$[PBI]_5Ru_4POM$ (TA)	0.25 mM	water	1mm	120μJ/cm^2	MG	87(4.1)
TDBC film	10% by mass in gelatin	quartz coated glass	500μm	45μJ/cm^2	MG	91(4.2)
NK2707 film	5% by mass in gelatin	quartz coated glass	500μm	45μJ/cm^2	MG	91(4.2)
Multilayer films	-	spacer: polystyrene	2μm distance	45μJ/cm^2	MG	91(4.2)
Organic cavity	-	spacer: polystyrene	2μm distance	100μJ/cm^2	MG	93(4.2)

B | Global Analysis

Introduction In this appendix we give an overview behind the global and target analysis in order to dynamically characterized the processes in a generic systems under time-resolved spectroscopic experiments. The systems considered for this kind of analysis are usually deal with ensemble of different molecules. The signal measured during a spectroscopic experiment depends on the spectral properties of each member of the ensemble and the temporal evolution of their concentration [67]. In case of the pump probe experiment, we measure the transient absorption spectrum (TA) as a function of time, which analytical expression can be written as:

$$S(t,\lambda) = \sum_{n=1}^{N} c_n(t)\epsilon_n(\lambda) \tag{B.1}$$

where c_n are the concentration of the n-component as function of time and the ϵ_n is the spectral properties of the component n. In order to reproduce the data acquired from the experiment, it is important to convolve the expression B.1 with the Instrument Response Function (IRF). Such function, in a spectroscopic experiment where short laser pulses are used, assumed a Lorentzian or Gaussian linehape.

Kinetic models The dynamical properties of the systems is contain only the the term $c_n(t)$. Typically the temporal evolution of the concentration of each component is described by linear differential equations, which solution is a sum of exponential decays. Let us consider the system described by N compartments, all their concentrations can be put in a matrix written as:

$$c(t) = [c_1(t).....c_N(t)]^T \tag{B.2}$$

By defining with K the transfer matrix of he macroscopic rates from one compartment to the other, the temporal evolution of the matrix $c(t)$ can be written as [68]:

$$\frac{d}{dt}c(t) = Kc(t) + j(t) \tag{B.3}$$

where $j(t)$ is the vector that represent the input defined as: $j(t) = i(t)[1x_2.....x_n]$ where $i(t)$ is the IRF and the vector $[1x_2.....x_n]$ are extra input for each compartment. The solution of the equation B.3 are exponential function convoluted with the $j(t)$ term:

$$c(t) = e^{Kt} \times j(t) \tag{B.4}$$

At this point, we can have two cases:
(i)K is a diagonal matrix: The element of the matrix K contain contribution of the decay rate of the single compartments. In this particular case, all the member of the ensemble are independent to each other and the model is called parallel model or model I. In this case we can write the expression of the single element of the matrix c(t) in the following way:

$$[c]_{pq} = c(t_p, k_q) = e^{-k_q t_p} \times i(t) \tag{B.5}$$

where p and q are the time and compartment indexes respectively. Usually the concentration matrix obtained in this case is called C_I
(ii) Off diagonal elements of matrix K are different from zero: In this case, the mathematical expression of $c(t)$ can be obtained by making eigenvalues and eigenvectors decomposition of the matrix K:

$$K = U\Lambda U^{-1} \tag{B.6}$$

where Λ is a diagonal matrix that contain eigenvalues and the matrix U contains eigenvectors. In this case the solution can be written as:

$$c(t) = e^{Kt} \times j(t) = Ue^{\Lambda t}U^{-1} \times j(t) = A_{II}^T C_I^T \tag{B.7}$$

where $A_{II}^T = Udiag(U^{-1}[1x_2.....x_n])$. Here the solution is a linear combination of the concentration found in the model I, where the decay of each compartment is independent to each other [69]. Such result is usually refereed to model II and we can write that as $C_{II} = A_{II}^T C_I^T$.

Discretization of the function S In a real experiment, the time axis is sampled and the signal data assume a 2D matrix dimension, where each element can be written as:

$$s_{t_i,\lambda_j} = \sum_{n=1}^{N} c_{n,t_i}\epsilon_{n,\lambda_j} + \phi_{t_i,\lambda_j} \tag{B.8}$$

where the term ϕ_{t_i,λ_j} represent the noise contribution during the measurement. The matrix elements c_{n,t_i} and ϵ_{n,λ_j} are the concentration and spectral amplitude at a specific time instant and wavelength respectively associated with the same compartment. Such values are usually collected in two matrices called C and E; in this way the formula B.8 can be written as:

$$S = CE^T + \Phi \tag{B.9}$$

By considering the matrix S the one obtained from the experimental data and matrices C and E the parametrized ones, it possible to find the best fit based of the kinetic model supposed for the concentration, by finding the minimum of the residual matrix (R) calculated as[70]:

$$R = S - CE^T \tag{B.10}$$

Unidirectional model :
In this paragraph we show the result obtained by considering a cascade model where each compartment decay to another one. This model is adopted for the natural light harvesting systems and the artificial quantasome presented in this thesis. In this particular case, the final expression of the compartment concentration is [71]:

$$c_n(t) = \sum_{j=1}^{n} b_{j,n} e^{-k_j t} \times i(t) \tag{B.11}$$

The exponential amplitudes indicate with letter b assuming the following values: when $j = n$, $b_{nn} = 1$ and for $j \leq n$

$$b_{jn} = \frac{\Pi_{m=1}^{n-1} k_m}{\Pi_{i=1}^{n}(k_i - k_j)} \tag{B.12}$$

In this condition, the corresponding life times obtained by the inverse of the rate k are sequentially increased. By defining with B the matrix of the amplitudes b, we can write a relation between the temporal evolution of the concentration function (C_{II}) and the expression of C_I obtained from the parallel model:

$$C_{II} = C_I B \tag{B.13}$$

DAS and EAS spectra Decay Associated Spectra (DAS) and Evolution Associated Spectra (EAS) are two different representations of the global analysis results by giving a direct interpretation of the various mechanisms (with a specific lifetime) that are taking place in the system [72]. The DAS contains the amplitude of the exponential decays where the decay and the rise of the signals are reveal from the amplitude sign. Specifically, the

positive amplitudes indicate the decay of Ground State Bleaching (GSB) and Stimulated Emission (SE) signals or a formation of Excited State Absorption (ESA). On the other hand, negative amplitudes represent a formation of GSB and SE or a decay of ESA. In this case, the expression of the entire signal S becomes

$$S = C_I DAS \tag{B.14}$$

Same interpretation, but different method are the EAS. Such spectra represent how the spectra the absorption changes after each time constants retrieved from the analysis. This aspect make the first EAS similar to the experimental spectrum at time zero and the last one will be proportional to the last DAS. These two different spectra are related with the matrix B with the following expression [73]:

$$DAS = EASB^T \rightarrow EAS = DASB^{-T} \tag{B.15}$$

Global analysis for 2DES dataset In case of 2DES experiment, the data set that we want to analysis has three dimensions: excitation wavelength, detection wavelength and waiting time. For the following calculation, we indicate the experimental data as a 3D matrix $S_{i,j,k}$ where i, j are the indexes of the two wavelength axis and the letter k represent the index for the time axis. In order to take into account both oscillatory and non oscillatory signal in t_2, the exponential functions adopted to fit the data are complex and each will have the following expression:

$$C_{n,k} = a_n e^{b_n t_k} \rightarrow C_{n,k} = |a_n| e^{i\phi_n} e^{-t_k/\tau_n} e^{i\omega_n t_k} \tag{B.16}$$

where the a_n contain information about modulus and phase of the signal and the term b_n contains information regarding the decay ($\tau_n = -1/Re[b_n]$) and the frequency ($\omega_n = Im[b_n]$) of the signal. Once the number n of the exponential component is chosen, every dynamics of each 2D spectrum point will be fit with the same series of exponential decays that shares the terms b_n (the decays are fixed for every point) and varying the amplitude terms. Such constrain reduce a lot the number of iteration that must be done in order to find the best fit. The algorithm can be simplified more by reducing the dimension of the data set from 3D to 2D. In particular, from a 3D dataset $S_{i,j,k}$ to 2D data set $Y_{k,h}$, where h is the index of excitation/detection frequency points in the 2D map [74]. We can now collect all the decay/frequency b terms and the amplitudes terms a of each point in the 2DES data in the matrices E and A with dimensions $(n \times k)$ and $(n \times h)$ respectively.

The final expression of the matrix model is:

$$M_{k,h} = \sum_{n=1}^{N} e^{t_k b_n} A_{n,k} \rightarrow M = EA \tag{B.17}$$

The total number of the parameters adopted in this case will be: $P = N + N * H$, where H is the number of all the frequency coordinate in the 2D map and N is the number of exponential functions. The calculation can facilitate by introducing another array z with length P that contains all the elements. The best fit is obtained via minimization of the least squares of the residuals:

$$min||Y - M(z)||^2 \tag{B.18}$$

The structure of the $M(z)$ allows to simplify the problem by separating the contribution of the A and E matrices and found the best solution only by focusing on the elements b_n [75]. In this way the number of iterations performed by the global analysis algorithm will be drastically reduced. The problem can be more simplified by introducing a sub-sampling in the frequency axis and set constrain for the values of the matrix B elements. Specifically we can divide the b values up in two groups. The first one is related to the non oscillatory component (only τ_n) where no constrains to the values are applied. The second one contains both decay and oscillatory component (τ_n and ω_n) that must be obey to the following points: (i) the decay that correspond to the oscillation dumping must be positive; (ii) the use of complex exponential implies that for each ω_n there is also their opposite $-\omega_n$ that decay with the same time. This allows to simplify the calculation by considering just one of them. (iii) The frequencies must be smaller than the Nyquist frequency associated with the time sampling [61].
If the amplitudes of the exponential decays can be graphically represented with the DAS, the same thing can be done for the amplitude associated with the complex exponential where the oscillatory terms appear. Such maps are called Coherence Associated Spectra (CAS) or oscillatory 2D map as it is reported for the free base porphyrin in chapter 2. This method is particularly useful in order to disentangle the information form the sample and from the solvent in which it is dissolved.

Acknowledgements

"An arrow can only be fired by first pulling it back. When life drags you back with difficulties, it means that it will throw you into something big. Concentrate and take aim"

Dalai Lama

This thesis is the result of three years of work where difficulties and satisfactions are mixed together. Of course, this result was not possible without the help of other people that support me in all of my career. First and foremost I thank Giulio Cerullo and Margherita Maiuri. They helped me in every projects and they teach me the basics of the non linear spectroscopy. I thank Franco V. de A. Camargo, Luca Moretti, Tersilla Virgili and Lucia Ganzer for training me in the laboratory activities as 2DES and pump probe experiments and giving me some advice for the different projects. I must thank all the external collaborators involved in the different projects starting from Stefano Santabarbara and Anna Paola Casazza for synthesizing the natural light harvesting systems samples and for helping in the analysis and data interpretation. I thank Kyriacos Georgiou, David Lidzey and Kirsty McGhee for developing organic microcavities and and thin film of semiconductor organic dyes in order to study the dephasing time. I thank The group of Marco Garavelli in Bologna and in particular Francesco Segatta for performing simulations of the 2DES data of PBI. I thank the group of Marcella Bonchio allow us to study their innovative artificial photosystem based on the Quantasome concept.
I think that a good research is also coming from a stimulated enviorment where colleagues (that are now friends) with different background gave me suggestion, advice and support. I must thank all of them: Piotr Kabacinski, Michele Guizzardi, Vasilis Petropoulos, Charles Sayers, Andrea Villa, Oleg Dogadov, Armando Genco, Chiara Trovatello, Mert Akturk, Veronica Policht and Aaron Ross. Nothing will be happened without the support of my family and my friends that always sustains me with all my decisions.

List of Publications

- M. Russo, A.P. Casazza, G. Cerullo, S. Santabarbara, M. Maiuri, Ultrafast excited state dynamics in the monomeric and trimeric Photosystem I core complex of Spirulina platensis probed by two-dimensional electronic spectroscopy, *J. Chem. Phys.*, Submitted
- M. Russo, K.E. McGhee, G. Cerullo, D. G. Lidzey, M. Maiuri, T. Virgili, Revealing Dephasing Time of a molecular dye for organic polaritonics by Two-Dimensional Electronic Spectroscopy, in preparation
- T. Nagahara, F. V. A. Camargo, L. Ganzer, M. Russo, F. Xu, P. Zhang, A. Perri, G. de la Cruz Valbuena, I. A. Heisler, C. D'Andrea, D. Polli, K. Müllen, X. Feng, Y. Mai, G. Cerullo, Electronic Structure of Single Graphene Nanoribbons dispersed in Liquid Phase Revealed by Two-Dimensional Electronic Spectroscopy, in preparation
- M. Maiuri, M. Russo, L. Moretti, V. Petropoulos, F. Rigodanza, A. Sartorel, M. Prato, G. Cerullo, M. Bonchio, Tracking Ultrafast Charge Separation in a PBI-based Biomimetic Complex for Oxygen Evolution, in preparation
- M. Russo, K. Georgiou, A. Genco, S. De Liberato, G. Cerullo, D. G. Lidzey, A. Othonos, M. Maiuri, T. Virgili, Direct Evidence of Ultrafast Energy Delocalization in a Strongly Coupled Organic Microcavity probed by TwoDimensional Electronic Spectrosc, in preparation
- F. Segatta, M. Russo, D. R. Nascimento, D. Presti, F. Rigodanza, A. Nenov, A. Bonvicini, A. Arcioni, S. Mukamel, M. Maiuri, L. Muccioli, N. Govind, G. Cerullo, M. Garavelli, In Silico Ultrafast Nonlinear Spectroscopy Meets Experiments: The Case of Perylene Bisimide Dye, *J. Chem. Theory Comput*, **17**, 7134-7145 (2021)
- V. R. Policht, M. Russo, F. Liu, C. Trovatello, M. Maiuri, Y. Bai, X. Zhu, S. Dal Conte, G. Cerullo, Dissecting Interlayer Hole and Electron Transfer in Transition Metal Dichalcogenide Heterostructures via Two-Dimensional Electronic Spectroscopy *Nano Lett.*, **21**, 4738-4743 (2021)
- M. Russo, A. P. Casazza, G. Cerullo, S. Santabarbara, M. Maiuri, Direct Evidence

for Excitation Energy Transfer Limitations Imposed by Low-Energy Chlorophylls in Photosystem ILight Harvesting Complex I of Land Plants, *J. Phys. Chem. B*, **125**, 3566-3573 (2021)

- F. V. A. Camargo, Y. Ben-Shahar, T. Nagahara, Y. E. Panfil, M. Russo, U. Banin, G. Cerullo, Visualizing Ultrafast Electron Transfer Processes in SemiconductorMetal Hybrid Nanoparticles: Toward ExcitonicPlasmonic Light Harvesting, *Nano Lett.*, **21**, 1461-1468 (2021)
- M. Russo, V. Petropoulos, E. Molotokaite, A. P. Casazza, G. Cerullo, M. Maiuri, S. Santabarbara, Ultrafast excited state dynamics in land plants Photosystem I core and whole super-complex under oxidised electron donor conditions, *Photosynth. Res.*, **144**, 221-233 (2020)
- L. Ganzer, S. Zappia, M. Russo, A. M. Ferretti, V. Vohra, M. Diterlizzi, M. R. Antognazza, S. Destri, T. Virgili,Ultrafast spectroscopy on water-processable PCBM: rod–coil block copolymer nanoparticles, *Phys.Chem.Chem.Phys.*, **22**, 2683 (2020)